

S-Duct Inlet Design for a Highly Maneuverable Unmanned Aircraft

Thesis

Presented in Partial Fulfillment of the Requirements for the Degree Master of Science in
the Graduate School of The Ohio State University

By

Jacob Brandon

Graduate Program in Aeronautical and Astronautical Engineering

The Ohio State University

2020

Thesis Committee

Dr. Clifford Whitfield, Advisor

Dr. Richard Freuler

Dr. Matthew McCrink

Dr. Jacob Allenstein

Copyrighted by

Jacob Brandon

2020

ABSTRACT

A design approach and performance analysis of a custom s-duct inlet is presented for a subsonic delta-wing unmanned aerial vehicle. The aircraft was designed, built at scale, and tested in a subsonic wind tunnel to obtain lift and drag characteristics. Lift and drag characteristics along with aircraft design requirements were used to determine an appropriate embedded jet engine for the scaled model. Important geometric parameters of the s-duct inlet consisted of a length-to-engine diameter ratio of 5.0, an offset-to-length ratio of 0.30, and an area ratio of 1.40. A review of fundamental concepts and the design process is presented to provide a foundation for future design iterations. Computational fluid dynamics software was used to analyze the inlet design performance in comparison to the well-documented RAE-M2129 inlet. Pressure recovery and circumferential/radial total pressure distortion were used to analyze inlet performance at zero incidence angle. Performance was also evaluated at an incidence angle of 21° to simulate a maximum rate of climb condition. Results for the inlet at zero incidence angle demonstrated a 1.12% decrease in pressure recovery compared to the RAE-M2129 inlet. Circumferential distortion intensity results were comparable between the two inlet geometries. The design inlet results showed larger distortion extent elements mainly due to flow separation from the second turn. Future experimental and computational work is proposed to further improve the inlet design.

DEDICATION

Dedicated to Mom and Dad.

ACKNOWLEDGEMENTS

I am beyond grateful for the opportunity to have worked on this project under the guidance of Dr. Whitfield. His unwavering support in the alignment of my research interests with the goals of this project undoubtedly fueled the outcome of this work and my inspiration for future research pursuits.

I also wish to thank Dr. McCrink for sharing his expertise in model fabrication and flight-testing methods. His willingness to share space, equipment, and materials at the ARC was crucial to the successful completion of wind tunnel tests.

I would also like to thank Dr. Freuler for his willingness to serve on my committee and for passing along critical information related to inlet pressure distortion.

Dr. Allenstein was instrumental to the completion of this thesis. I can't thank him enough for his support in terms of computational resources and advice on computational best-practices. The results shown in this thesis would not have been possible without him.

Colin Trussa deserves a special thank you for all the times he stopped his work or answered the phone in the middle of the night to help me work through something. I am lucky to have such a great friend.

Finally, thank you to my family and friends.

VITA

June 1, 2013 Medina High School, Medina, OH, USA

May 6, 2018 B.S. Aeronautical and Astronautical Engineering,
The Ohio State University, Columbus, OH, USA

August 21, 2018 – Present Graduate Research/Teaching Associate,
Aeronautical and Astronautical Engineering,
The Ohio State University, Columbus, OH, USA

FIELDS OF STUDY

Major Field: Aeronautical and Astronautical Engineering

TABLE OF CONTENTS

ABSTRACT	ii
DEDICATION	iii
ACKNOWLEDGEMENTS	iv
VITA	v
LIST OF TABLES	viii
LIST OF FIGURES	ix
CHAPTER 1. MOTIVATION FOR A NEW UAV PLATFORM	1
1.1 XQ-1A Design	2
1.2 XQ-1B Design	6
CHAPTER 2. PLATFORM FOR TESTING UAV MODEL	7
2.1 Wind Tunnel Facility	7
2.2 Wind Tunnel Corrections	8
2.2.1 Tunnel Blockage	8
2.2.2 Downwash	9
2.3 Experimental Equipment	10
2.3.1 Force Balance	11
2.3.2 Angle of Attack System	14
2.3.3 Data Acquisition	16
2.4 XQ-1A Wind Tunnel Results	17
2.4.1 Power Required	21
CHAPTER 3. INLET DESIGN	30
3.1 Brief Historical Background on Inlet Design	30
3.1.1 Types of Inlets	31
3.1.2 Design Consideration of External Boundary Layers	34
3.1.3 XQ-1A Inlet Choice and Inspiration from F-16 Fighting Falcon	37
3.2 Fundamental Concepts	41
3.2.1 Flow in Straight Pipes	43
3.2.2 Flow in Curved Pipes	48

3.3 Inlet Performance Parameters	53
3.4 XQ-1A-1 Inlet Design.....	63
CHAPTER 4. COMPUTATIONAL FLUID DYNAMICS	68
4.1 Previous CFD Work on S-duct Inlets	68
4.2 Governing Equations and Turbulence Modeling.....	72
4.3 RAE-M2129 Geometry.....	78
4.4 RAE-M2129 Mesh Validation Results	87
4.4 XQ-1A-2 Inlet Design.....	96
4.4.1 Geometry Scaling.....	100
4.4.2 CFD Results and Discussion.....	104
CHAPTER 5. CONCLUSIONS AND FUTURE WORK.....	117
5.1 Conclusions.....	117
5.2 Future Work	119
BIBLIOGRAPHY	122
APPENDIX.....	126

LIST OF TABLES

Table 1 UAV design requirements	2
Table 2 Equations used by force balance to convert from body axis to stability axis frame of reference [7].....	12
Table 3 H-388 force balance calibration information [10]	13
Table 4 JetCat P20-SX Specifications	25
Table 5 Radial positions of total pressure probe locations in QinetiQ experimental data	80
Table 6 RAE-M2129 geometric parameters	81
Table 7 Summary of RAE-M2129 mesh validation results.....	89
Table 8 Inlet geometry comparison	101
Table 9 CFD results for XQ-1A inlet design compared against RAE-M2129 mesh validation case.....	105
Table 10 Summary of AIP circumferential and radial total pressure distortion	113

LIST OF FIGURES

Figure 1 XQ-1A – 1/3 rd -scale delta-wing aircraft model used for flight tests. Total span, 36”, total length 48”.....	3
Figure 2 XQ-1A – 1/5 th -scale model used for wind tunnel testing (image is taken upside down in the wind tunnel)	4
Figure 3 Initial sizing estimations.....	5
Figure 4 OSU ARC 3'x5' wind tunnel	8
Figure 5 Body axis frame of reference [8].....	11
Figure 6 Relationship between body axis and stability axis frame of reference [8].....	12
Figure 7 H-388 six-component force balance.....	14
Figure 8 External view of angle of attack system with the XQ-1A installed (model is installed upside down)	15
Figure 9 XQ-1A pitched at high angle of attack (model is installed upside down).....	16
Figure 10 LabView wind tunnel data acquisition interface	17
Figure 11 XQ-1A lift curve for various elevon deflection angles	18
Figure 12 XQ-1A drag polar for various elevon deflection angles	19
Figure 13 XQ-1A lift-to-drag ratio for various elevon deflection angles	20
Figure 14 Induced drag factor for unswept linearly tapered wings [11].....	23
Figure 15 Thrust required at sea level.....	24
Figure 16 JetCat P-20SX engine [12]	25
Figure 17 Estimated power requirement of XQ-1A compared against power available using JetCat P-20SX engine.....	26
Figure 18 Excess power throughout range of attainable flight speeds	27
Figure 19 Climb angle associated with maximum rate of climb	28
Figure 20 Types of inlets for embedded engine applications [4].....	31
Figure 21 F-16 landing gear placed within chin inlet cowl [14].....	33
Figure 22 Typical boundary layer removal methods [4]	35
Figure 23 Typical layout of a channel boundary layer diverter for a chin mounted inlet	36
Figure 24 Lockheed Martin F-35 DSI [17].....	37
Figure 25 Front view of General Dynamics F-16V Fighting Falcon [19]	39
Figure 26 F-16 inlet length and offset dimensions [20].....	40
Figure 27 F-16 inlet variants - NSI (top) and MCID (bottom) [21]	41
Figure 28 Representative variation in mass flow ratio based on flight condition [13]....	42
Figure 29 Important results of Poiseuille experiments. (a) Change in local lateral pressure with distance from pipe entrance, (b) Linear change in pressure gradient with volumetric	

flow rate in fully developed region, (c) Linear change in volumetric flow rate with pipe diameter. Figure obtained from [22].....	44
Figure 30 Evolution of the velocity profile in the entrance region of a pipe due to near-wall viscous effects	46
Figure 31 Poiseuille velocity profile entering a pipe bend with a constant radius of curvature, R . A fluid element traveling through the bend at a velocity, u , experiences a radial acceleration proportional to $\rho u^2/r$. The centripetal acceleration and velocity profile induces secondary flow. Figure obtained from [22].	49
Figure 32 Flat velocity profile entering a curved pipe. Highest velocity occurs near the inside wall of the bend. Figure obtained from [22]	50
Figure 33 Stability margin definition [27]	56
Figure 34 Typical probe/rake array [27]	57
Figure 35 Example of ring circumferential intensity and extent distortion elements for a one-per-revolution pattern [27]	59
Figure 36 Example of ring circumferential distortion for a multiple-per-revolution pattern [27].....	60
Figure 37 General configuration of s-duct inlet fit to JetCat P-20SX engine.....	63
Figure 38 XQ-1A-1 design choice of engine position and relative inlet/nozzle lengths. (JetCat P-20SX engine highlighted in purple)	64
Figure 39 Dimensions relevant to the XQ-1A-1 inlet offset.....	66
Figure 40 XQ-1A-1 inlet lofting planes and s-duct centerline	67
Figure 41 Four coherent turbulent modes found in [36] using DDES and SPIV	72
Figure 42 Continua physics models	73
Figure 43 Summary of all- $y+$ wall treatment [37]	78
Figure 44 Main sections of RAE-M2129 geometry [38, with additional annotations]	82
Figure 45 RAE-M2129 lip geometry approximation.....	83
Figure 46 Side view of RAE-M2129 lofting planes	84
Figure 47 RAE-M2129 simulation domain	85
Figure 48 RAE-M2129 unstructured mesh.....	86
Figure 49 RAE-M2129 wall $y +$	87
Figure 50 RANS mesh validation solution obtained through outlet pressure adjustments	88
Figure 51 Mach contour comparison between Onera RANS results (top) and mesh validation RANS results (bottom)	91
Figure 52 Static pressure along duct walls - starboard and port	93
Figure 53 AIP pressure recovery	94
Figure 54 Pressure recovery through downstream half of RAE-M2129 s-duct	95
Figure 55 Updated design iteration defined by the intersection of two circular arcs	97
Figure 56 Definition of s-duct centerline curvature.....	98
Figure 57 Side view of discretized centerline with constant radius of curvature (highlighted in yellow).....	99
Figure 58 XQ-1A inlet design.....	100
Figure 59 Comparison of absolute and normalized centerline profiles of XQ-1A inlet and RAE-M2129	102

Figure 60 Comparison of normalized area distribution between XQ-1A inlet and RAE-M2129	103
Figure 61 Cross-sectional ellipse dimensions of XQ-1A inlet	104
Figure 62 XQ-1A Mach number contour with streamlines for $0^\circ AOA$ (top) and $21^\circ AOA$ (bottom).....	106
Figure 63 AIP pressure recovery comparison between RAE-M2129 (left) and XQ-1A inlet at $AOA = 0^\circ$ (middle) and XQ-1A inlet at $AOA = 21^\circ$ (right).	107
Figure 64 Rear-visualization of dean vortices located near the outside corner of the second turn, left to right: RAE-M2129, XQ-1A ($0^\circ AOA$), XQ-1A ($21^\circ AOA$).....	108
Figure 65 Pressure recovery through downstream half of XQ-1A inlet ($0^\circ AOA$).....	109
Figure 66 Plane progression of pressure recovery within XQ-1A inlet ($21^\circ AOA$).....	110
Figure 67 AIP circumferential total pressure distortion	116
Figure 68 RAE-M2129 mesh validation residuals.....	126
Figure 69 XQ-1A $0^\circ AOA$ residuals.....	126
Figure 70 XQ-1A $21^\circ AOA$ residuals.....	127
Figure 71 XQ-1A $0^\circ AOA$ mass flow solution monitor	127
Figure 72 XQ-1A $21^\circ AOA$ mass flow solution monitor	128
Figure 73 Inlet lip flow separation observed for XQ-1A at $21^\circ AOA$	128

CHAPTER 1. MOTIVATION FOR A NEW UAV PLATFORM

The motivation for this project stemmed from the desire to build on the developmental work of unmanned air vehicles (UAVs), performed at The Ohio State University's Aerospace Research Center (ARC). In August 2017, an Ohio State team of researchers set multiple absolute speed and distance world records in the Class U category of UAVs [1]. The Avanti N619RA sustained average speeds of 147 miles per hour over an out-and-back course approximately 28 miles long. The vehicle utilized a custom-built flight controller, control via satellite communications, redundant radio control links, and collision detection technology to safely complete the record-setting flight. The overall goal of this project was to design, build, and test an aerodynamically interesting aircraft that would push the limits of in-house flight-testing techniques and procedures [2, 3].

Design requirements and definitions outlined in Table 1 served as the foundation for the UAV design.

Table 1 UAV design requirements

Design Requirement	Definition
(1) High speed	Aerodynamically efficient in terms of airframe and engine growth
(2) Highly maneuverable	Inherently capable of low-speed, high g-load maneuvers
(3) Aerodynamically interesting	Nonlinear aerodynamic characteristics due to complex flows
(4) Multi-configurable	Easily adaptable for multiple wing configurations

It was determined at an early stage in the design process that the scope of initial work should focus on the development of a subsonic platform, therefore the focus of the work was on implementation of design requirements (2)-(4). However, important early design decisions were made in consideration of scalability to higher flight speeds. These early design decisions involved the use of an area-ruled fuselage to mitigate the problems associated high-speed compressible wave-drag. In addition to the consideration of drag rise at high speeds, it was decided that an embedded engine would serve as an appropriate method of engine-airframe integration. The design decision of an embedded engine motivated the need for the work presented in this thesis – the design and analysis of a UAV inlet to deliver clean air flow to the engine.

1.1 XQ-1A Design

In accordance with design requirements, The Flight Vehicle Design and Testing (FVDT) Group at the ARC created the XQ-1A as a preliminary 1/3rd-scale flight-test

demonstrator layout. The model was also built at 1/5th-scale to serve as an important platform to perform wind tunnel tests to verify initial performance and stability estimates. Both scaled versions of the XQ-1A model were also fit with elevon control surfaces at the trailing edge of the delta wing, however only the 1/3rd-scale model was outfitted with functional elevons for flight-testing. Due to flight-test capability, the inlet design discussed throughout this thesis was designed to fit the 1/3rd-scale XQ-1A geometry. The aerodynamic characteristics obtained from the wind tunnel tests of the 1/5th-scale XQ-1A are used in this thesis to determine the appropriate engine for the 1/3rd-scale layout. The 1/3rd- scale demonstrator model and the 1/5th-scale wind tunnel model are shown below in Fig. 1 and Fig. 2, respectively.

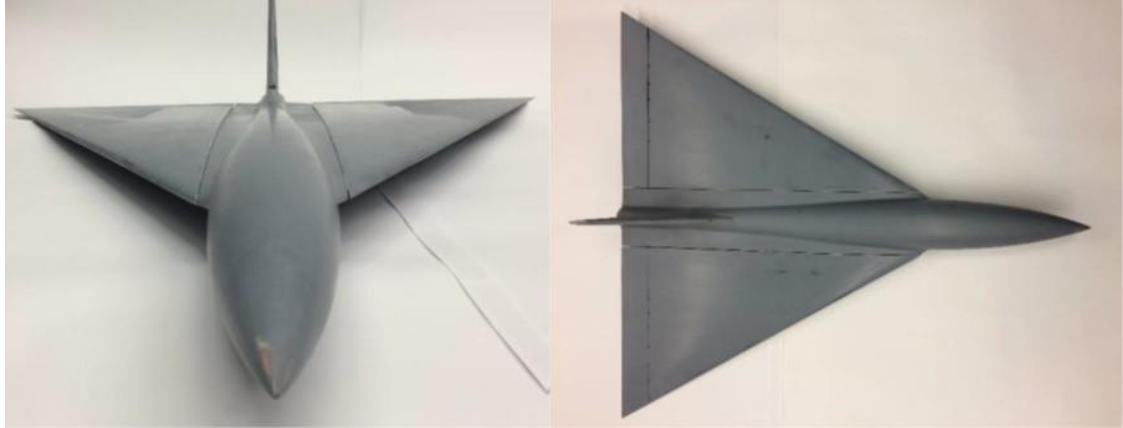


Figure 1 XQ-1A – 1/3rd-scale delta-wing aircraft model used for flight tests. Total span, 36", total length 48".



Figure 2 XQ-1A – 1/5th-scale model used for wind tunnel testing (image is taken upside down in the wind tunnel)

The XQ-1A utilized an axisymmetric area-ruled fuselage sized to house necessary internal components, a delta wing with a sweep of 60° and a capable high-speed wing of symmetric cross-sectional shape. The vehicle was sized for a full-scale cruise speed of

300 kts and maneuvers up to 7 g's at 150 kts, with the intent to scale down the vehicle geometry for initial testing. Figure 3 below is the sizing plot that was used to identify initial values for wing-loading and minimum thrust-loading that met the design constraint of a 300 kts cruise speed (g_1), high-maneuverability constraint, defined by maintaining positive energy under load (g_2), and a low-speed flight capability constraint, defined by stall-speed or maximum lift (g_3). The baseline values selected for wing-loading and minimum thrust-loading are shown as a black dot in Fig. 3.

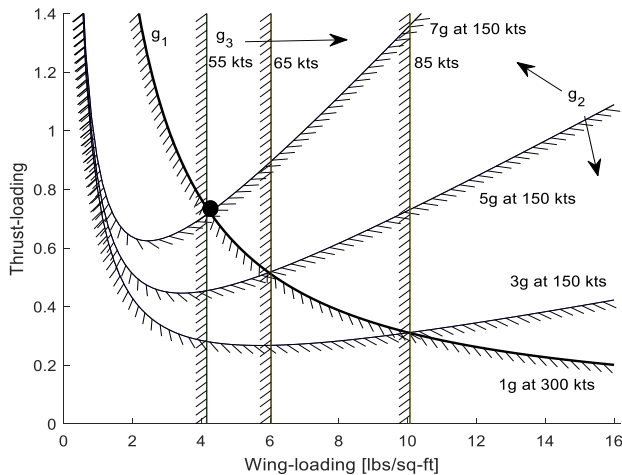


Figure 3 Initial sizing estimations

The first-cut weight and wing area estimates were based on an installed JetCat P-400 Pro series jet engine with a rough estimate of 80% installed thrust efficiency. The aircraft outlined above represents a large scale (group III-IV) Unmanned Aircraft System

(UAS). The 1/3rd-scale demonstrator was powered by an electric pusher-propeller configuration for flight-test purposes.

1.2 XQ-1B Design

The XQ-1B represented an additional design iteration of the UAV that implemented deflectable wing tips to better satisfy design requirements (1), (3), and (4). The XQ-1B layout was built at 1/5th-scale to provide a platform suitable for wind tunnel testing at the ARC. Deflectable wing tips have been used on delta wing aircraft such as the North American XB-70 Valkyrie because they increase lift due to shock capture and improve stability at supersonic speeds. At supersonic speeds, the vertical tail loses effectiveness and the aerodynamic center of the aircraft shifts downstream, which causes corresponding changes of directional and longitudinal stability, respectively [4]. A downward deflection of the wing tips helps to mitigate both issues of directional and longitudinal stability because it acts as a larger effective tail and prevents the shift of the aerodynamic center. An additional outcome of The FVDT Group due to the implementation of wing tips is discussed by Trussa [5], which assesses the low-speed aerodynamic characteristics of the XQ-1B layout at various angles of attack and wing tip deflection configurations. While future design iterations of the 1/3rd-scale UAV model will likely include deflectable wing tips, it is important to note that the following discussion of wind tunnel results is based only on XQ-1A data.

CHAPTER 2. PLATFORM FOR TESTING UAV MODEL

2.1 Wind Tunnel Facility

Wind tunnel experiments were conducted in an open-return suction-type subsonic wind tunnel located at the ARC (schematic shown below in Fig. 4) to obtain aerodynamic characteristics of the 1/5th-scale XQ-1A model. Both the inlet and exit of the tunnel were exposed to outdoor environmental conditions. Flow at a Reynolds number of approximately 5×10^5 was driven by a 7.8 ft, 6-bladed, fan located at the exit of tunnel. The fan was belt-driven by a 125 hp three-phase AC motor. The exact test section dimensions in terms of height, width, and length were 39"x59"x96", respectively, with an upstream area contraction ratio of 6.7 [6]. Air speed was calculated using transducer measurements of the differential pressure between the settling chamber and just upstream of the test section. Multiple screens and a honeycomb are used upstream in the tunnel to condition the flow prior to the test section. LabView was used to monitor airspeed in real time.

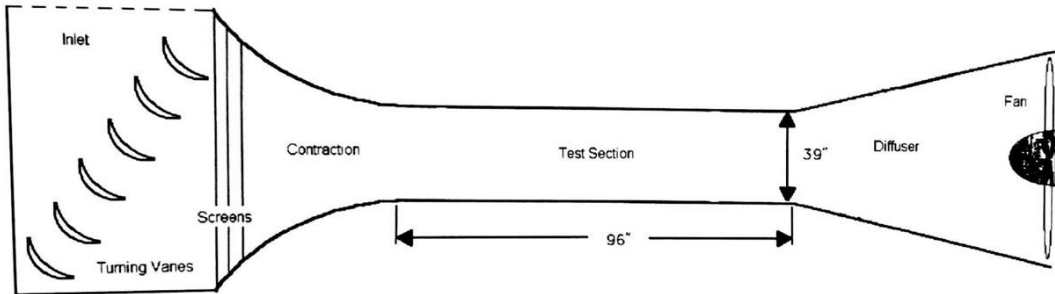


Figure 4 OSU ARC 3'x5' wind tunnel

2.2 Wind Tunnel Corrections

Wind tunnel corrections were applied automatically within the data acquisition system to account for the effects of wind tunnel blockage, downwash, model base drag, and weight tare of the 1/5th-scale model.

2.2.1 Tunnel Blockage

The UAV model inherently causes a blockage in the wind tunnel that reduces the flow cross-sectional area in the test section. The effect of blockage is that the area reduction slightly increases the flow velocity around the model in comparison to the flow velocity that would occur in unconstrained freestream atmospheric conditions. The wind tunnel data corrects for tunnel blockage through Eqn. 1 from [7], which uses the ratio of the volume of the model to the height and width of the test section to calculate the average change in velocity around the model.

$$u_1 = V * \left(\frac{Vol}{h^2 b} \right) \quad (1)$$

In Eqn. 1, u_1 represents the average change in velocity around the model, which is assumed as constant throughout the test section. Also, V is the uncorrected tunnel speed as measured by the pressure transducers, h represents the test section height, b is the test section width, and Vol represents the volume of the model. The volume of the model was estimated by using 70% of the multiplication of the 1/5th-scale model thickness, the wing span, and the root chord. Based on this correction procedure, the estimated artificial increase in velocity due to tunnel blockage was approximately 1% of the uncorrected tunnel velocity.

2.2.2 Downwash

The interaction between the tunnel boundaries and the model can have a significant effect on lift and drag measurements due to changes in downwash. The main net effects of changes in downwash are an increase in measured drag and angle of attack relative to free-air conditions. The changes in downwash are caused by the interaction between wing tip vortices and the tunnel walls, which has an increasing effect as the distance between the wing tips and the nearby tunnel walls decreases. It is recommended

by [7] to ensure that the wing span is less than 80% of the tunnel width to reduce downwash effects. The 1/5th-scale model used in testing had a wingspan of 2 ft which equates to approximately 40% of the wind tunnel width. Equations 2 and 3 describe the downwash corrections applied to the wind tunnel results, provided by [7] for a wing in a closed octagonal jet. In the equations, δ represents the boundary correction factor (a value of 0.125 was used as recommended by [7]), S is the wing area, and C is the cross-sectional area of the tunnel. Using these equations, the drag coefficient increase was calculated as 0.0065, and the local angle of attack increase was 0.37°.

$$\Delta C_D = \delta \frac{S}{C} C_L^2 \quad (2)$$

$$\Delta \alpha = \delta \frac{S}{C} C_L \quad (3)$$

2.3 Experimental Equipment

Essential experimental equipment used in the wind tunnel testing of the XQ-1A included a six-component force balance, a system to vary angle of attack, and the data acquisition system. A brief description of the experimental equipment is discussed in this section.

2.3.1 Force Balance

An HH-388 six-component internal strain gauge force balance (shown in Fig. 7) was used to measure aerodynamic loads on the 1/5th-scale UAV model. Forces were measured by the balance in the body axis frame of reference (*B*) and then converted to the stability axis frame of reference (*SA*) based on angle of attack. The stability axis resolves lift and drag components that are perpendicular and parallel to the flow direction, respectively. Sideslip angle (β) was not considered in this study. Figure 5 below illustrates the body axis frame of reference. Table 2 and Fig. 6 demonstrate the conversion of forces from the body axis frame to the stability axis frame.

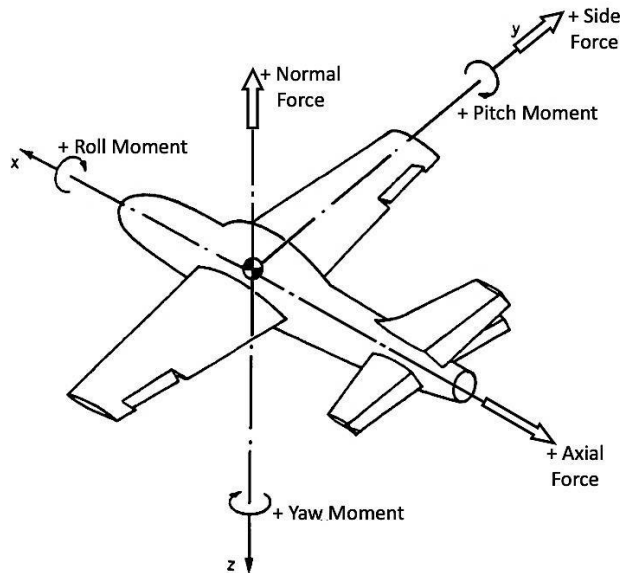


Figure 5 Body axis frame of reference [8]

Table 2 Equations used by force balance to convert from body axis to stability axis frame of reference [7]

$LF_{SA} = NF_B \cos\alpha - AF_B \sin\alpha$	$RM_{SA} = RM_B \cos\alpha + YM_B \sin\alpha$
$DF_{SA} = AF_B \cos\alpha + NF_B \sin\alpha$	$YM_{SA} = YM_B \cos\alpha - RM_B \sin\alpha$
$SF_{SA} = SF_B$	$PM_{SA} = PM_B$

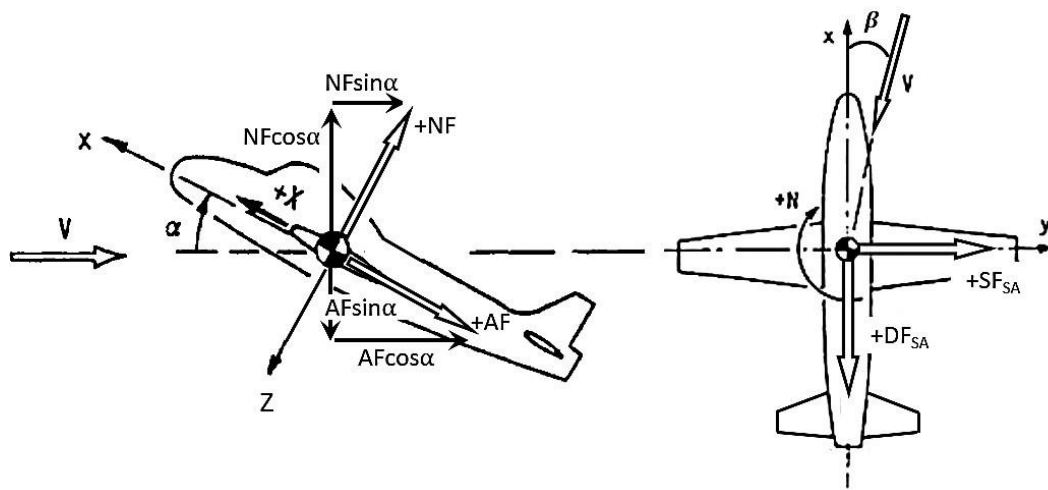


Figure 6 Relationship between body axis and stability axis frame of reference [8]

Calibration information for the H-388 force balance is provided below in Table 3.

The forces measured in the experiments were within the lower range of the force balance calibration curve. A high level of measurement accuracy is maintained at low loads due to the design of the balance and the high gain, low noise signal conditioning and acquisition system [9].

Table 3 H-388 force balance calibration information [10]

Component	Max Design Load	Max Calibration Loads		Instrument Accuracy (%) Load)
		Positive	Negative	
Normal Force 1	600 lbs	22.5 lbs	-22.5 lbs	-0.020
Normal Force 2	600 lbs	22.5 lbs	-22.5 lbs	-0.020
Side Force 1	600 lbs	22.5 lbs	-22.5 lbs	-0.020
Side Force 2	600 lbs	22.5 lbs	-22.5 lbs	-0.021
Rolling Moment	400 in-lbs	116.2 in-lbs	-116.2 in-lbs	-0.021
Axial Force	150 lbs	10.25 lbs	-16.9 lbs	-0.020

The force balance was attached through the back of the model, which resulted in an open-air cavity between the force balance and the fuselage. Increased pressure within the open-air cavity caused an additional pressure drag force that needed to be estimated and subtracted from the wind tunnel measurements. The additional drag force was estimated and removed from measurements in the axial force direction using Eqn. 4. Changes in the lift component due to pressure drag were also accounted for as a function of angle of attack. In Eqn. 4, $D_{fuselage}$ and D_{sting} represent the diameter at the aft-most position of the fuselage and the diameter of the sting, respectively. The wing area is represented by S , and q_∞ is the freestream dynamic pressure.

$$C_{D_{Base}} = \frac{q_\infty}{S} \pi \left(\frac{D_{fuselage} - D_{sting}}{2} \right)^2 \quad (4)$$



Figure 7 H-388 six-component force balance

The weight of the model was removed from the signal output of the force balance through each angle of attack position. It was necessary to perform the weight tare procedure at each angle of attack position because of the changing direction of the body force frame of reference through which the model weight force was measured. Subtraction of the signal output due to the weight of the model allowed an isolation of the signal output change due to aerodynamic loads at each angle of attack.

2.3.2 Angle of Attack System

A parallelogram linkage system was built to vary the angle of attack of the model. The system passed vertically through the wind tunnel test section, positioned downstream of the model to reduce flow interference. The linkage was designed such that the center of the model corresponded to a fixed point of rotation through the range of angle attack to maintain the position of the model within the length of the test section. Steel bars were used in the linkage system to provide structural integrity and avoid vibrations due to

unsteady aerodynamic loading. A translational jackscrew powered by an electric motor was used to adjust angle of attack. A system of counterweights was required to reduce the load on the jackscrew and electric motor. Figures 8 and 9 below illustrate the external and internal view, respectively, of the angle of attack system installed within the wind tunnel.

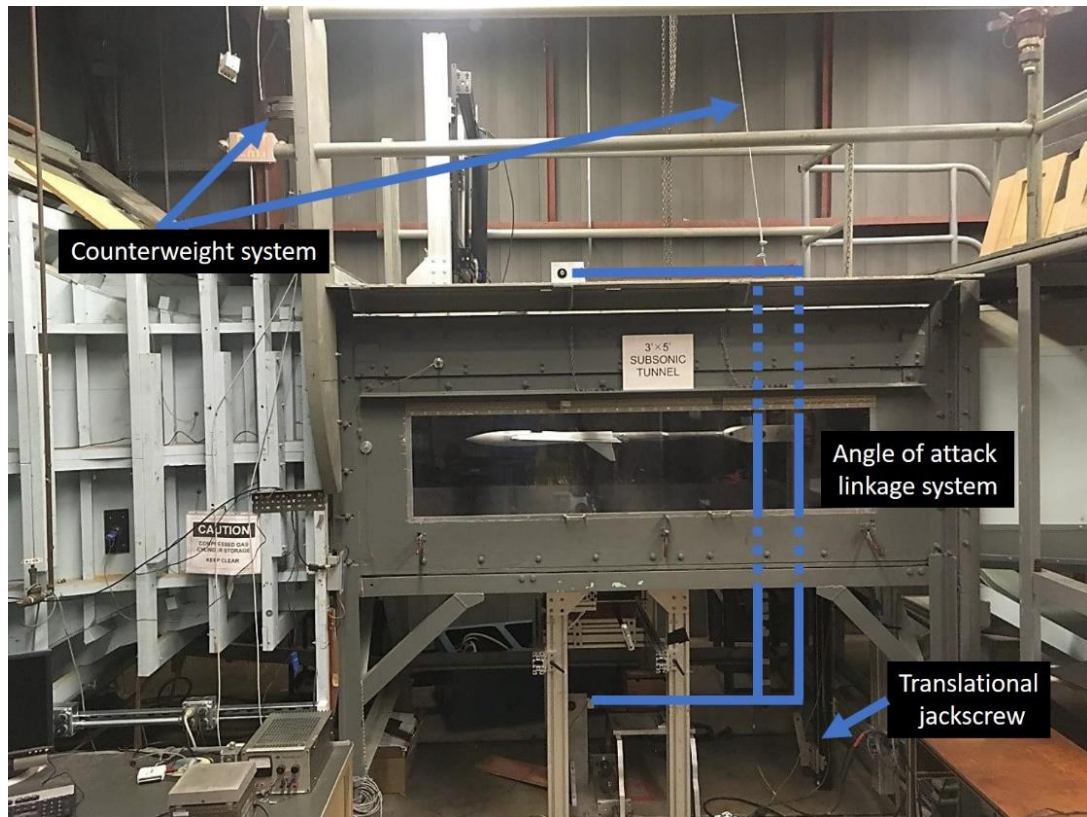


Figure 8 External view of angle of attack system with the XQ-1A installed (model is installed upside down)

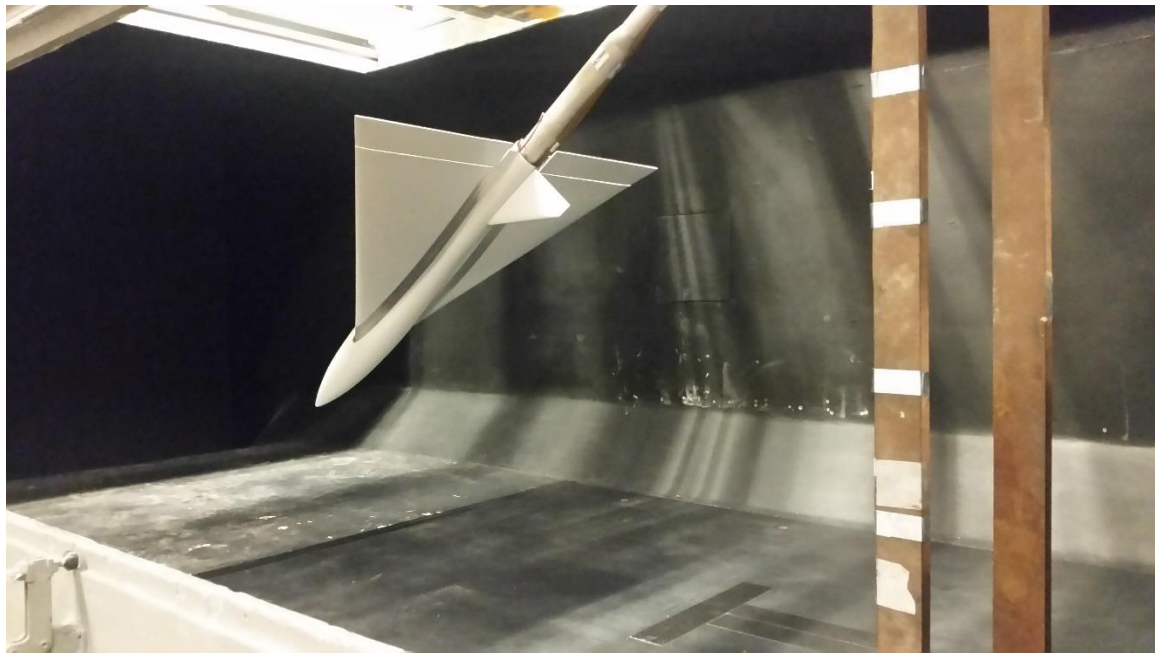


Figure 9 XQ-1A pitched at high angle of attack (model is installed upside down)

2.3.3 Data Acquisition

Force balance data was obtained using a National Instruments Compact DAQ 9174 (NI-9174). The NI-9174 sampled data at 200 Hz and provided time-averaged results over a period of 5 seconds. The LabView interface is shown below in Fig. 10, which was monitored in real-time during testing. Prior to data acquisition, the user was responsible for inputs of angle of attack and the test section air velocity.

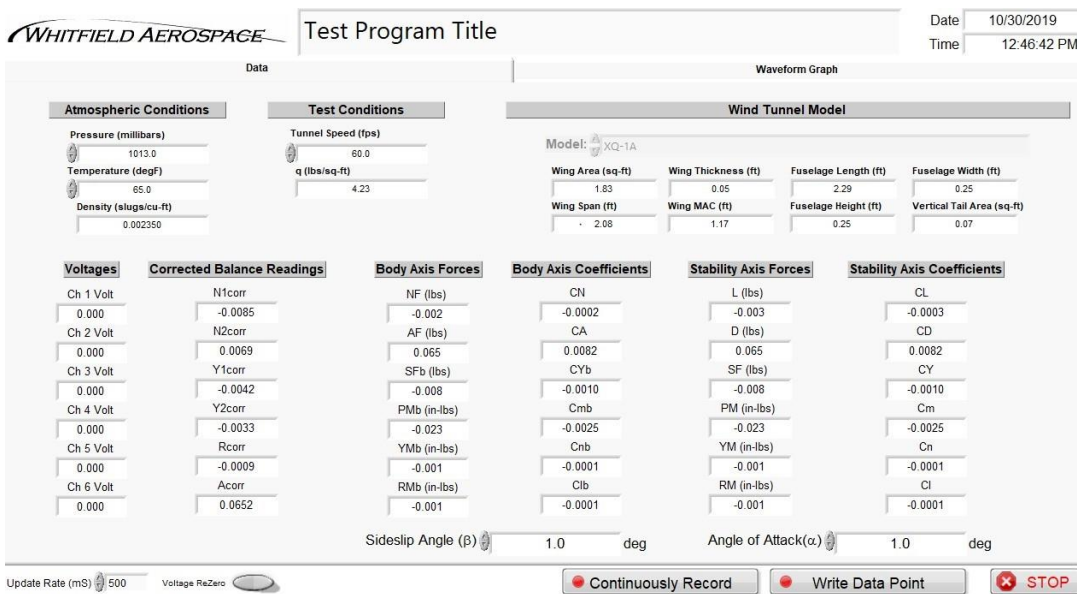


Figure 10 LabView wind tunnel data acquisition interface

2.4 XQ-1A Wind Tunnel Results

Wind tunnel test results provided valuable information regarding the lift and drag characteristics of the 1/3rd-scale XQ-1A model under various static angle of attack conditions. The results were used to guide general design decisions for the inlet system, as well as determine the necessary propulsion to appropriately meet the design requirements.

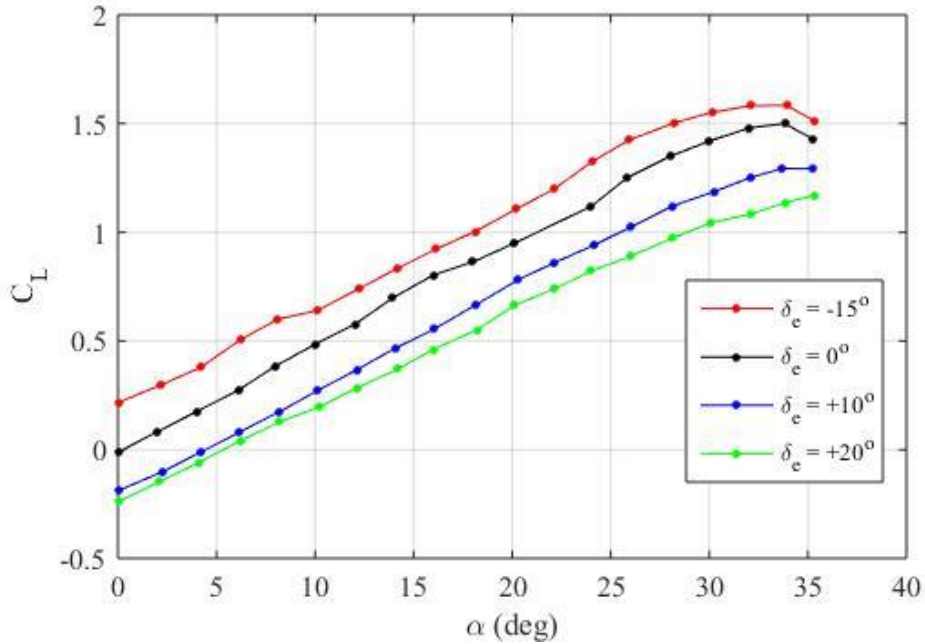


Figure 11 XQ-1A lift curve for various elevon deflection angles

Figure 11 confirms the expected lift curve slope for the delta wing UAV of approximately 0.05/degree, as well as a large stall angle of attack of 34°. Figure 11 also highlights the change in lift characteristics of the XQ-1A as elevon deflection angle (δ_e) varies between -15° to +20° . As expected, a negative elevon deflection angle increases the effective camber of the airfoil sections within the wing and causes an increase in lift coefficient. The relatively low lift curve slope of the delta wing narrowed the potential design options for the position of the UAV's inlet. The low lift curve slope requires the UAV to operate at high angles of attack to maintain lift, particularly at low-speed conditions. The need to deliver clean airflow to the engine at extreme flight conditions determined the choice of inlet location on the UAV. Extreme flight conditions were

interpreted for the inlet design as those involving high entry flow incidence angles, which occur during low-speed or highly maneuverable flight conditions. High entry flow incidence angles cause flow separation near the lip of the inlet, which propagates downstream to arrive at the engine face as highly distorted flow. High levels of distortion can lead to compressor stall and loss of thrust during flight.

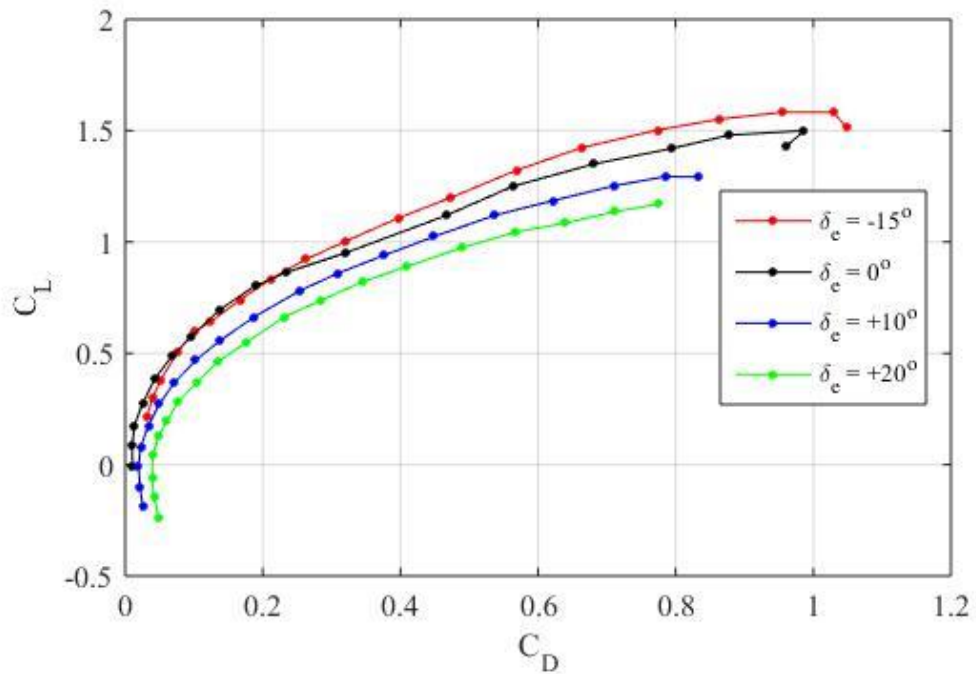


Figure 12 XQ-1A drag polar for various elevon deflection angles

The drag polar in Fig. 12 was used to determine the zero-lift parasitic drag coefficient of the UAV and to better understand the induced and parasitic drag penalty

that occurs due to lift. The experimental zero-lift parasitic drag coefficient of 0.0109 was used from Fig. 12 for required thrust calculations that helped determine the appropriate engine for the 1/3rd-scale UAV model.

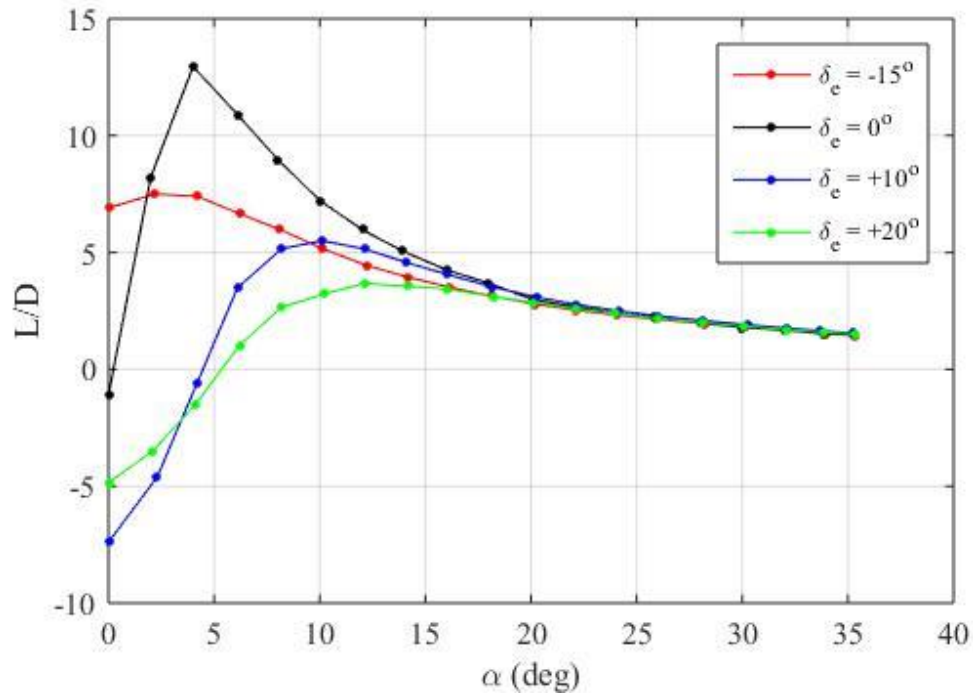


Figure 13 XQ-1A lift-to-drag ratio for various elevon deflection angles

Figure 13 confirms that XQ-1A operates at a maximum aerodynamic efficiency at an angle of attack of 4° with zero elevon deflection. Elevon deflection angle is shown to have a significant effect on lift-to-drag ratio at low angles of attack. Fig. 13 also demonstrates the gradual decrease in lift-to-drag ratio at increasing angle of attack. High

lift-to-drag ratio is especially important for the UAV inlet design in terms of the angle of attack that corresponds to an efficient sustained cruise flight condition. Ideally, the inlet should efficiently capture this entry flow incidence angle during cruise without sacrificing performance at extreme angles of attack.

2.4.1 Power Required

Power requirements of the 1/3rd-scale UAV were considered under steady, level, unaccelerated flight conditions at sea level. Under these assumptions, the thrust required was calculated using Eqn. 5.

$$T_R = \frac{W}{C_L/C_D} = \frac{W}{L/D} \quad (5)$$

An estimated weight of approximately 10 lb was used for the 1/3rd-scale model, based on the estimated wing loading in Fig. 3 multiplied by the wing area. The variation of lift-to-drag ratio with flight speed was determined using the following equations.

$$C_L = \frac{W}{\frac{1}{2}\rho_\infty V_\infty^2 S} \quad (6)$$

$$C_D = C_{D,0} + \frac{c_L^2}{\pi e AR} \quad (7)$$

A lift coefficient was calculated using Eqn. 6 for each flight speed assuming constant weight, which was used to calculate the corresponding drag coefficient in Eqn. 7. An Oswald efficiency factor of 0.87, and a zero-lift parasitic drag coefficient of 0.0109 obtained from wind tunnel data, were used to estimate the total drag coefficient. The Oswald efficiency factor was calculated from Eqn. 8 below, along with estimations for the lift-induced form drag factor, K'' , and the induced drag factor, δ .

$$e = \frac{1}{K'' \pi AR + 1 + \delta} \quad (8)$$

$$\text{where } K'' = \frac{dC_{D_f}}{dC_L^2} \cong 0.011, \quad \delta \cong 0.06$$

The conservative estimate of K'' (typical range between 0.009-0.012 [11]) was based on the inherently large surface area of the delta wing. The induced drag factor of 0.06 was approximated from an extrapolation of Fig. 14 below, using an aspect ratio (labeled A in Fig. 14) of 2.4 and a taper ratio near 0.

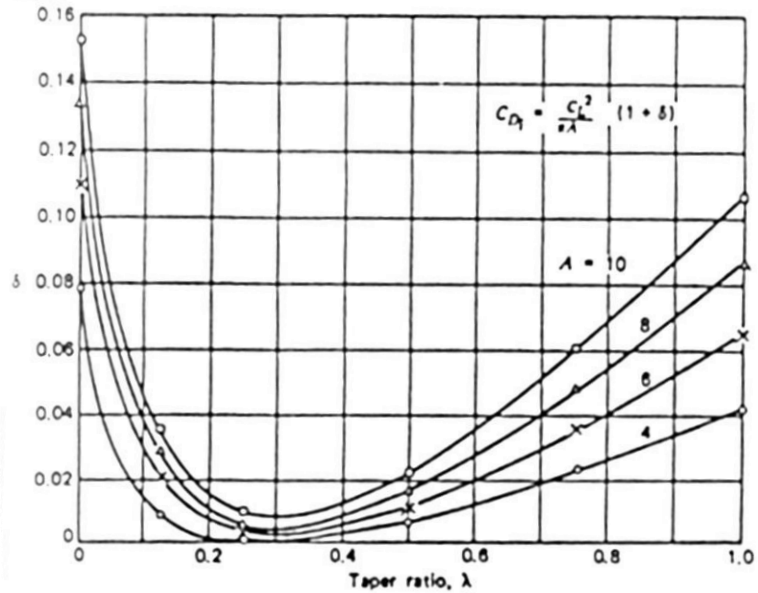


Figure 14 Induced drag factor for unswept linearly tapered wings [11]

The ratio of Eqn. 6 and 7 over various flight speeds was used in Eqn. 5 to determine the thrust required, as shown below in Fig. 15.

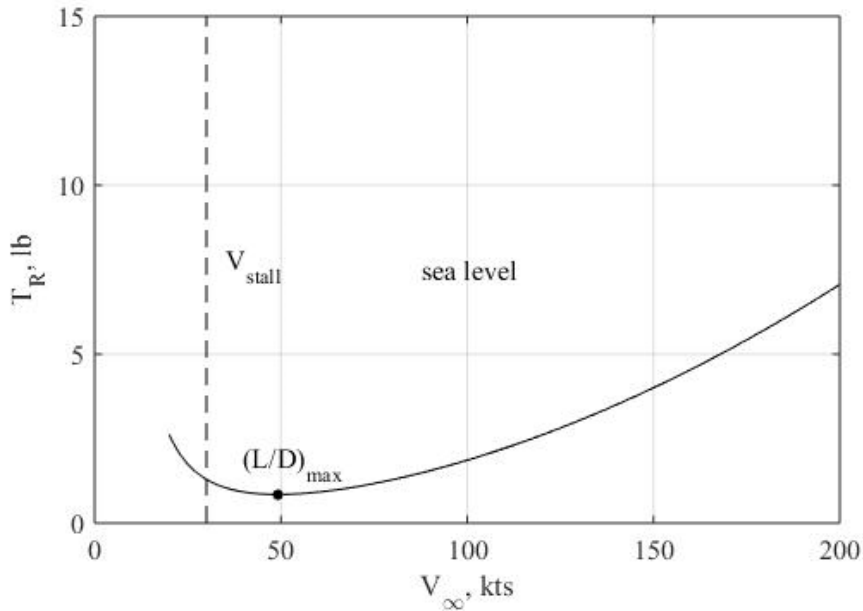


Figure 15 Thrust required at sea level

Figure 15 provides insight into the increase in required thrust as flight speed is increased. At flight speeds to the left of the minimum of the thrust required curve, induced drag dominates as the UAV must increase angle of attack to maintain lift, which demands a slightly larger thrust relative to the minimum. An updated calculated stall speed of approximately 30 kts is shown based on an updated estimation of the scaled model weight and maximum lift coefficient from wind tunnel data. A minimum thrust required of 0.6 lb corresponds to the estimated maximum lift-to-drag ratio.

Figure 15 was used along with sizing and cost considerations to determine an appropriate engine. Figure 15 shows the JetCat P-20SX engine that was chosen for the 1/3rd-scale model. The engine specifications are described below in Table 4.

Table 4 JetCat P20-SX Specifications

Engine Metric	Rated Specification
Idle [1/min]	85000
Max rpm [1/min]	245000
Idle thrust [lb]	0.07
Max thrust [lb]	5.4
Exit gas temperature [$^{\circ}$ F]	1274
Pressure ratio	1.5
Mass flow [lb/s]	0.11
Exhaust gas velocity [kts]	1450
Fuel consumption at idle rpm [floz/min]	0.41
Fuel consumption at max rpm [floz/min]	3.04
Weight [lb]	0.77
Engine Diameter [in] (\varnothing_{engine})	2.36
Length (including starter motor) [in]	7.09



Figure 16 JetCat P-20SX engine [12]

The final decision for the engine choice was determined through consideration of cost, engine size relative to the model, and available thrust. It was determined that it was desirable to require minimum modifications to the existing fuselage to internally mount

the engine. The JetCat P-20SX dimensions of length and diameter closely matched the existing fuselage dimensions, which was assumed to support increased ease of installation.

The desired cruise speed of the full-scale UAV is 300 kts, therefore a rough approximation of the desired speed capability of the 1/3rd scale model is 100 kts. Figure 17 demonstrates that the P-20SX engine provides the scale model with adequate thrust to maintain steady, level flight up to 175 kts. The power curves in Fig. 17 further illustrate the estimated power provided by the P-20SX engine compared with the XQ-1A's power requirements over a range flight speeds.

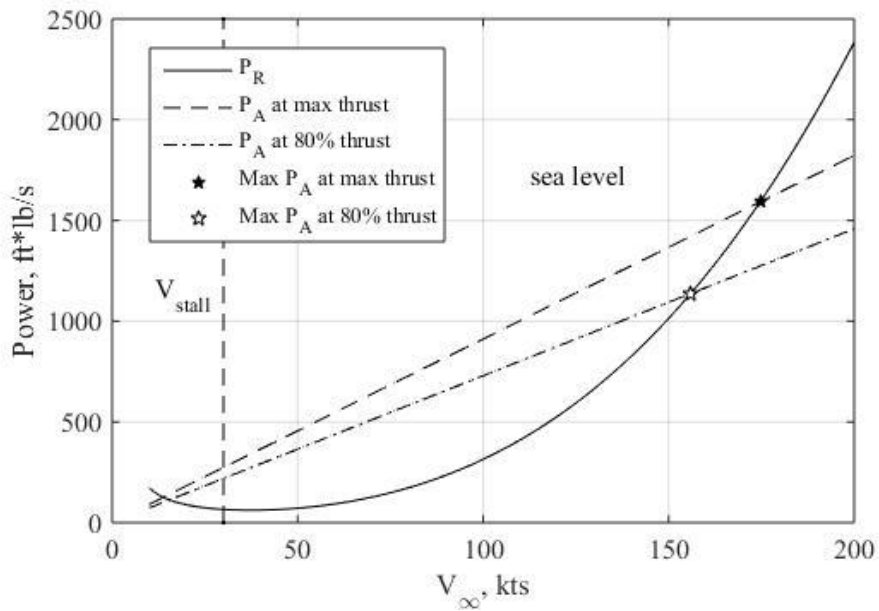


Figure 17 Estimated power requirement of XQ-1A compared against power available using JetCat P-20SX engine

Figure 17 shows that the engine can power the XQ-1A to a maximum flight speed of approximately 175 kts. This condition corresponds to the engine's maximum thrust condition, which would likely only be run for a short amount of time to preserve the life of the engine. The subsonic XQ-1A scale model does not have a strict need for long-range cruise at high subsonic speeds. An additional line is plotted in Fig. 17 to represent the available power if the JetCat engine is run at 80% thrust. The intersection of this curve with the power required curve shows an achievable flight speed of 155 kts, which represents a more sustainable throttle condition for the engine.

The UAV's design requirement of maneuverability necessitates excess power from the engine. Figure 18 below further demonstrates the expectation of excess power through the range of attainable flight speeds at maximum thrust.

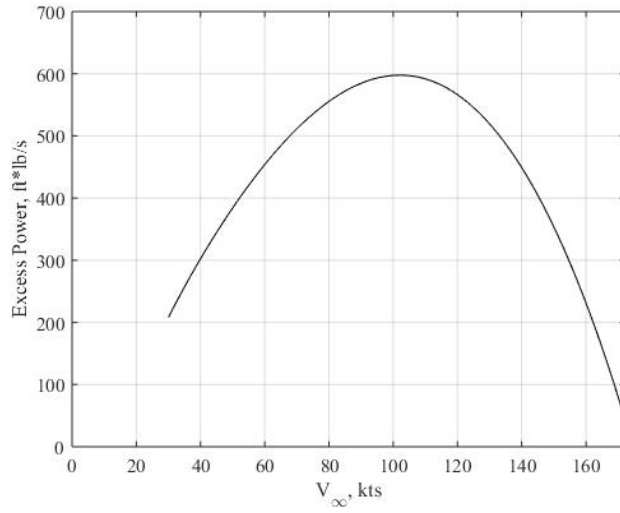


Figure 18 Excess power throughout range of attainable flight speeds

The maximum excess power occurs at a flight speed of approximately 100 kts, corresponding to a maximum rate of climb of 57 ft/s. Excess power is related to rate of climb through Eqn. 9 below.

$$R/C = \frac{\text{excess power}}{W} \quad (9)$$

Equation 9 leads to important information in terms of inlet design because it can be used to develop Fig. 19, which estimates the climb angle necessary to achieve specific rates of climb over varying forward flight speeds.

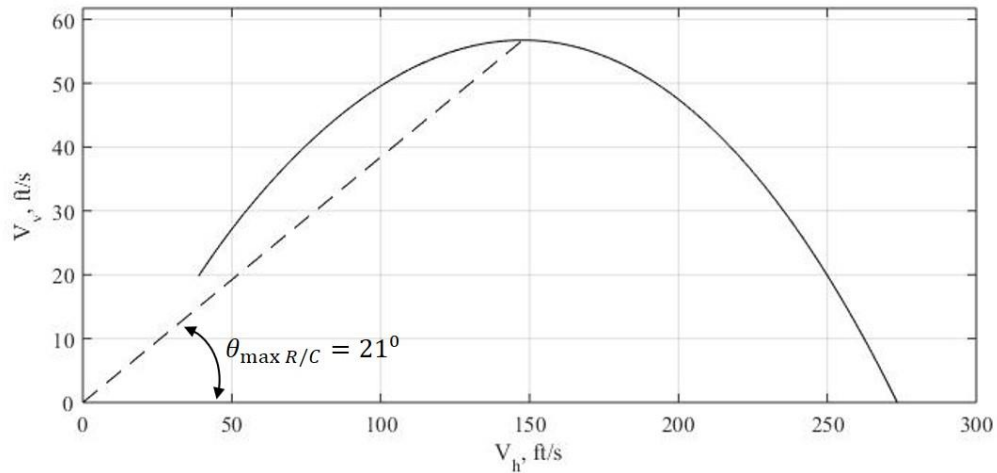


Figure 19 Climb angle associated with maximum rate of climb

The climb angle of 21° , along with vertical and horizontal velocities of 57 ft/s and 147 ft/s, respectively, are used in this thesis to evaluate the performance of the proposed XQ-1A inlet. In the subsequent analyses, the climb angle is assumed as equivalent to angle of attack to simulate conditions that immediately follow initiation of a pitch-up maneuver. This was determined as a reasonable assumption due to the expected fast rate at which these maneuvers will be performed.

CHAPTER 3. INLET DESIGN

3.1 Brief Historical Background on Inlet Design

Prior to the development of the jet engine in the 1940s, background knowledge on inlet aerodynamics stemmed from research on cooling systems for piston-engine aircraft [13]. The Second World War accelerated interest in jet engines for aircraft propulsion, particularly due to the desire to achieve supersonic flight capability. Achievement of supersonic flight required the need of an engine embedded in the fuselage to mitigate sharp increases in drag in the transonic flight regime. Due to the desire for supersonic flight, research in the 1940s focused predominantly on efficient handling of shock waves in an inlet system to deliver clean subsonic flow to the engine. Through this research of inlets in supersonic freestream speeds, the concept of spillage drag was an important discovery that proved to be vital to subsonic inlets. The '60s unveiled the significance of dynamic distortion in terms of its effect on compressor performance. The late '70s uncovered the problem of swirling flow on compressor surge. In general, effective inlet design focuses on compromises between external and internal flow field requirements.

Inlet aerodynamic design diverges from external aerodynamic design in the fundamental sense that inlets must operate continuously in separated flow regimes, while external aerodynamic design often uses flow separation as a limit of operation [13]. Proper handling of separated flow in an inlet design requires an understanding of the behavior of the turbulent boundary layer which, until recent developments in computational fluid dynamics (CFD), has been understood only through experimentation.

An efficient inlet design effectively balances the deliverance of clean air flow to the engine with the consequence of external drag on the aircraft in consideration of the full mission profile.

3.1.1 Types of Inlets

Inlet location can have a large impact on the quality of air flow that enters the inlet and on engine performance. Choice of inlet location can depend on a wide variety of design variables including weight and sizing restrictions, aircraft mission profile, landing gear location, wing type, fuselage geometry, among many others. Figure 20 and the general discussion below from Raymer [4] outlines typical inlet types for embedded engine applications.

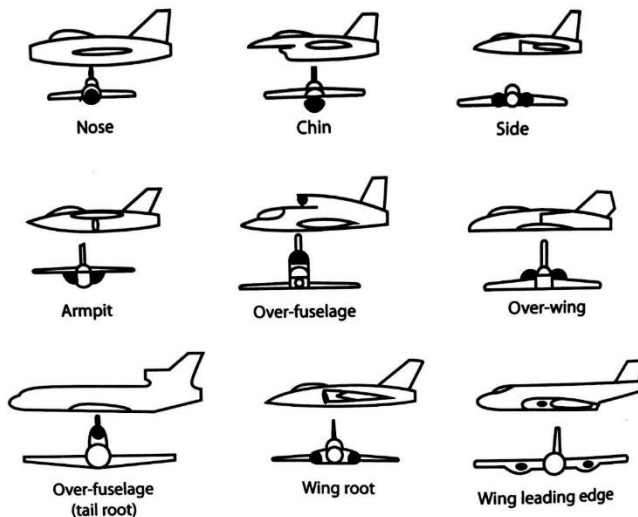


Figure 20 Types of inlets for embedded engine applications [4]

The nose inlet location offers the most uniform air flow delivery to the engine because it provides a straight-line connection between the freestream air and the engine. Internal flow separation is a non-issue beyond what may occur near the inlet lip at high incidence angles or at ground-running conditions. The problem with a nose inlet stems from the need for a very long duct, which adds a significant amount of weight and has high frictional losses within the internal boundary layer. The nose inlet also causes problems with sizing other components of the aircraft such as landing gear, due to the large volume that the inlet inherently occupies.

The chin inlet allows for a shorter duct length and has many of the same benefits associated with the nose inlet, however it does require internal bends that can cause losses due to flow separation. It is especially suited for high angle of attack flight conditions because of its position below the fuselage, and because the fuselage forebody helps turn the flow in the direction of the inlet. Nose wheel landing gear position is also important with a chin inlet because it likely should be placed aft of the inlet entrance face to avoid inlet distortion and foreign-object ingestion. Landing gear for a chin inlet is typically within the inlet cowl as shown in Fig. 21 below, which shows extended landing gear for the F-16. The cross-sectional area of the cowl must increase in this configuration to safely house retracted landing gear, which causes an increase in cowl drag. Aircraft with twin engines and a dual chin inlet layout can potentially avoid these issues through placement of the nose wheel landing gear between the chin inlets.



Figure 21 F-16 landing gear placed within chin inlet cowl [14]

Side mounted inlets are often used in twin engine aircraft to provide short duct lengths and relatively clean air flow. Side inlets can have distortion issues at high angles of attack due to vortex ingestion from the fuselage forebody. Blockage can become an issue for a side mounted inlet during a maneuver with a high degree of yaw. A single engine aircraft can also use side mounted inlets that converge toward the engine face, however the flow paths should remain separate from each other through the entire system to avoid compressor stall due to pressure instabilities that can occur from flow mixing.

An “armpit” inlet is located between the fuselage and the wing junction for a high-mounted wing. It is a risky design choice because of the possibility of combined boundary layer ingestion from both the fuselage and the wing. Careful consideration of boundary layer diversion must be integrated into the design of an armpit inlet to achieve the full benefit of its short duct length. An over-wing inlet suffers many of the same issues as an armpit inlet, and it is especially problematic at high angles of attack.

The main benefit of an over-fuselage inlet is that it eliminates the nose wheel landing gear complexities involved with a chin inlet. The over-fuselage inlet is often not suitable for high angles of attack because the fuselage forebody can potentially completely block air flow to the engine. Careful design of the fuselage can mitigate this problem through the generation of vortices that induce flow in the direction of the inlet. An over-fuselage inlet can also be placed near the tail of the aircraft, which is beneficial because it locates the engine exhaust near the rear of the fuselage to reduce flow separation and drag. The cost of this configuration is often an s-duct with large offset and large flow turning angles that can lead to low pressure recovery and high distortion from internal separation.

Wing root and wing leading edge inlet eliminate the need for an inlet cowl and thus reduce drag, however both configurations can significantly decrease wing performance due to flow disturbances over the wing. The wing root inlet can also potentially ingest the fuselage boundary layer.

3.1.2 Design Consideration of External Boundary Layers

In nearly all inlet types described above, aside from nose and outboard wing leading edge inlets, careful design consideration must be taken to avoid boundary layer ingestion from external surfaces upstream of the inlet. A common approach is to employ a form of a boundary layer removal near the inlet entrance. Four main types of boundary layer removal techniques are shown below in Fig. 22, as outlined in Raymer [4].

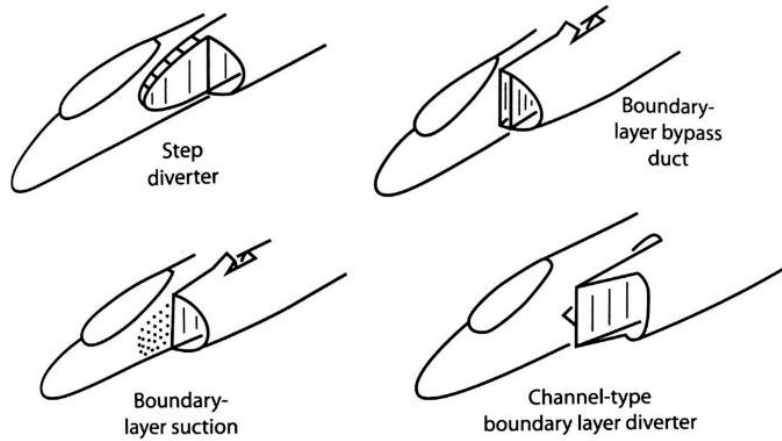


Figure 22 Typical boundary layer removal methods [4]

The step diverter is simply an upstream surface extrusion that is designed to push low-energy boundary layer air away from the inlet and draw in high-energy air. The step diverter length is typically one inlet diameter upstream of the inlet and has a thickness equivalent to approximately 2-4% of the fuselage length ahead of the inlet [4].

The boundary layer bypass duct is a separate inlet duct designed to separate the boundary layer from the high-energy air, then eject it downstream. The boundary layer suction removal method is similar to that of the bypass duct, only it uses holes or a series of slots upstream of the inlet instead of a duct. Reduced drag is a benefit of the boundary layer suction method because it reduces the frontal area and wetted area of the inlet system, however it does not function as well as a bypass duct.

The most common form of boundary layer removal is the channel diverter (also shown on the F-16 in Fig. 21 above). The inlet is located at a distance away from the fuselage that is determined based on an estimation of the boundary layer thickness. A

splitter plate is often used to redirect the boundary layer air in a manner that minimizes drag. The additional drag associated with the channel diverter can be large and is dependent on the frontal area of the channel, therefore the frontal area of the channel should be minimized as much as possible. A typical boundary layer diverter for a chin inlet configuration is shown below in Fig. 23.

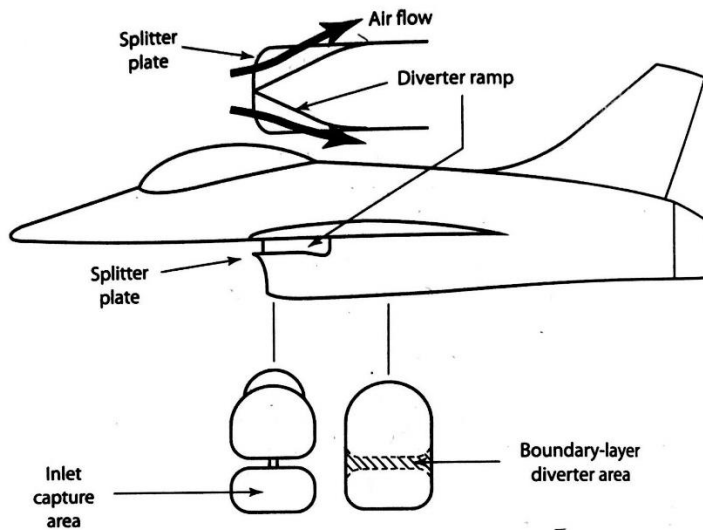


Figure 23 Typical layout of a channel boundary layer diverter for a chin mounted inlet

Divertorless supersonic inlets (DSI) represent a novel modern approach to boundary layer diversion near the inlet entrance. A DSI inlet utilizes a contoured bump surface upstream of the flush inlet to serve as a precompression surface and boundary layer removal device that can significantly increase the engine's available power. The

theoretical application was first developed by Dr. Antonio Ferri in the early 1950s [15], and first implementation of the concept was seen on the F11F-1F. Modern CFD capabilities have allowed for further refinement of these contoured bump surfaces, as shown below in Fig. 24 by Lockheed Martin's F-35 patented DSİ design [16].



Figure 24 Lockheed Martin F-35 DSİ [17]

3.1.3 XQ-1A Inlet Choice and Inspiration from F-16 Fighting Falcon

In the early stages of the XQ-1A inlet design, it was important to apply the general principles of the previous discussion to choose an inlet type that supported achievement of the design requirements.

Wind tunnel data for the XQ-1A confirmed the expectation that the delta wing configuration was capable of high angle of attack operations, which eliminated the possibility of any over-fuselage inlet types to avoid air flow blockage and the complexities of additional fuselage design modifications. High angle of attack capability of the XQ-1A is largely due to the additional vortex lift generated by the leading-edge vortex system inherent to a delta wing configuration [18], therefore a leading-edge inlet system was deemed as incompatible with the XQ-1A. Side mounted inlets were mainly eliminated as a design choice due to the long duct length that would be required to place the inlet upstream of the leading-edge wing root. Also, it was determined that the XQ-1A would be powered by a single engine, which reduced the benefits of a dual inlet system. A nose mounted inlet was not desirable because of the need to house avionics in the fuselage.

It was decided that a chin mounted inlet would deliver the highest quality air flow to the engine in accordance with the XQ-1A design requirements. The chin mounted inlet provides the ability to use a relatively short duct length and is highly functional at high angles of attack, which is especially applicable to the XQ-1A during takeoff, landing, and pitch-up maneuvers. The aft location of the inlet also limits any interference with the wing, preserving the interesting aerodynamic phenomenon of the delta wing.

The choice of a chin mounted inlet motivated design inspiration from the General Dynamics F-16 Fighting Falcon, shown below in Fig. 25.



Figure 25 Front view of General Dynamics F-16V Fighting Falcon [19]

The use of the F-16 as inspiration was justified by its proven performance record (1979 – present) as a light-weight multi-purpose 4th generation fighter, along with its high-speed and maneuverability design requirements that are closely aligned with the goals of the XQ-1A design. The F-16 has a maximum short-endurance speed of approximately Mach 2.0 and a highly maneuverable 9 g design load factor. At the time of writing this thesis, there are approximately 3,000 operational F-16s in service for 25 countries worldwide, with new production aircraft having an expected service life to 2060 and beyond [19]. Externally, the XQ-1A inlet design discussed in later sections follows the F-16 inlet system design in the allowance of space for a channel-type boundary layer diverter. The detailed design of the channel diverter is not considered in the scope of this work. Internally, the main sources of inspiration taken from the F-16 were the general cross-sectional shape and the relative inlet length, as shown below in Fig. 26. For reference, the F-16 inlet length and offset dimensions relative to the engine diameter were estimated as approximately $L/\phi_{engine} \approx 4.2$ and $H/\phi_{engine} \approx 0.28$.

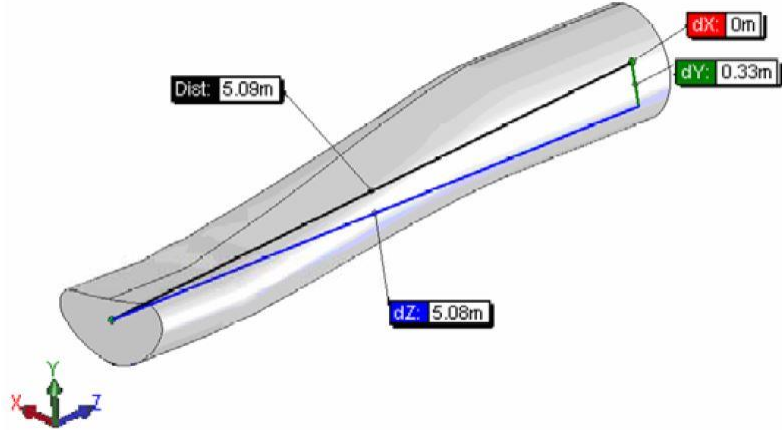


Figure 26 F-16 inlet length and offset dimensions [20]

The F-16 inlet uses semi-elliptical cross-sections at the entrance of the inlet that closely fit the curvature of the fuselage. The downstream cross-sections gradually transition to a circular shape near the engine face. Similarly, the XQ-1A inlet design utilizes elliptical-to-circular cross-sections. The current F-16V (“Viper” variant) is categorized into two “Blocks” that mainly denote the difference in engine configuration. The Block 70 configuration uses an F110-GE-129 engine to power the aircraft, while the F-16V Block 72 configuration uses an F100-PW-229 engine. Both engines produce a thrust of approximately 29,000 lb and have a similar maximum diameter ($\sim 1.2 \text{ m}$), however the Pratt & Whitney engine variant uses the smaller Normal Shock Inlet (NSI), and the General Electric engine uses the larger Modular Common Inlet Duct (MCID or “Bigmouth” inlet) [20]. The larger MCID is designed to supply additional mass flow to the engine. The slight differences in geometry can be seen below in Fig. 27.

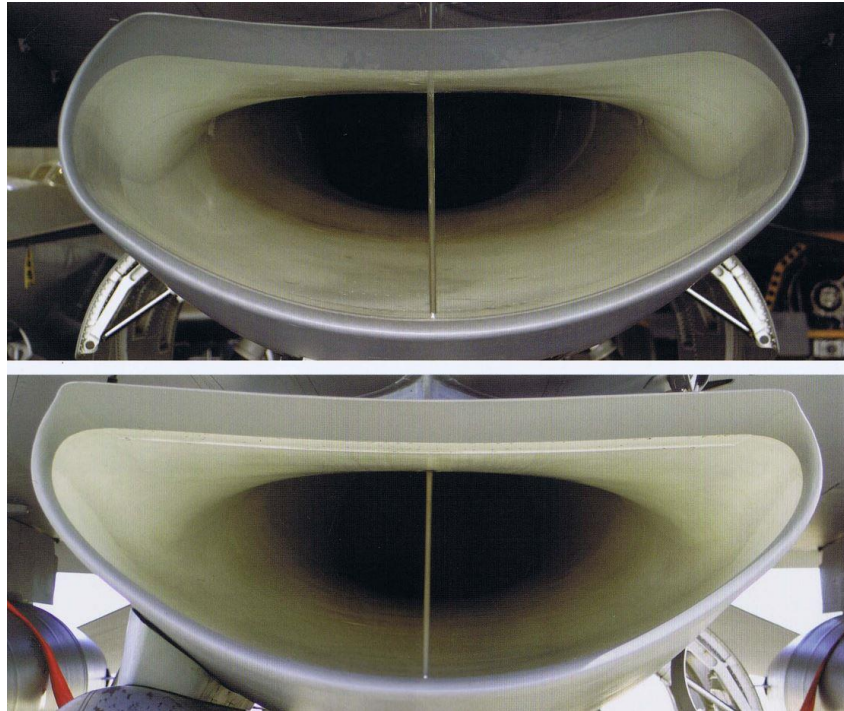


Figure 27 F-16 inlet variants - NSI (top) and MCID (bottom) [21]

3.2 Fundamental Concepts

An efficient inlet design must consider both the internal and external flow field over a range of flight conditions. The external flow field represents the input flow conditions to the inlet, which can have a significant impact on performance due to downstream propagation of non-uniform flow. Sharp streamline curvature near the lip of an inlet can lead to flow separation. The behavior of the fuselage boundary layer also changes based on flight speed and varying incidence angles. For subsonic conditions, the external flow field at zero incidence angle can be conceptualized in terms of the change in mass flow ratio, defined as the ratio of the captured freestream streamtube area to the

inlet entrance face area. The typical main flight conditions that cause variation of the flow ratio are (a) high-speed cruise, (b) climb, (c) ground running, and (d) top speed, as shown below in Fig. 28.

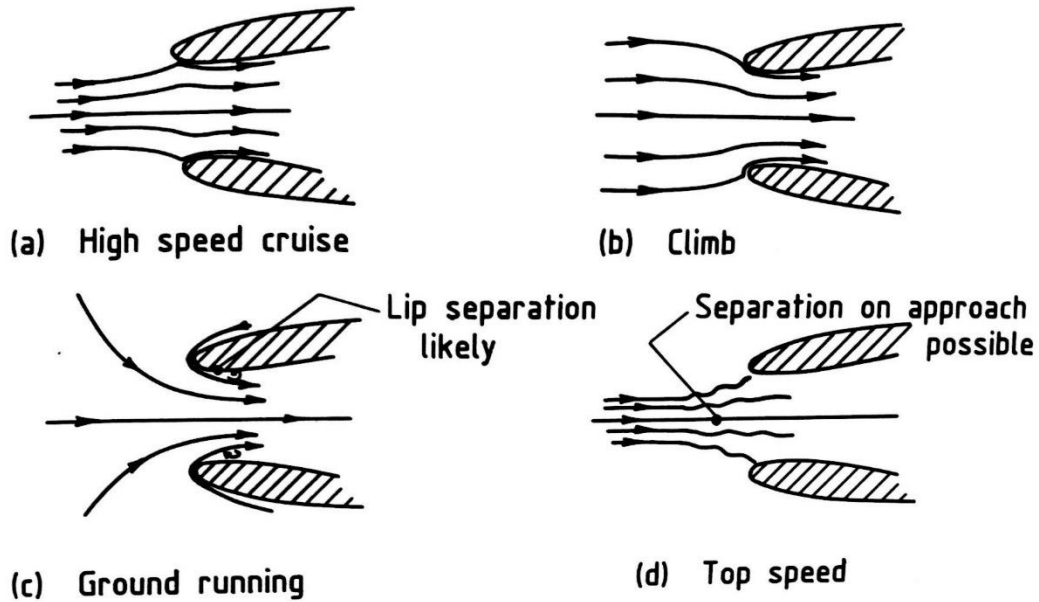


Figure 28 Representative variation in mass flow ratio based on flight condition [13]

In the high-speed cruise condition, the mass flow ratio is usually in the range of 0.5 to 0.8 [13], and the inlet operates at peak performance. Efficient pre-entry retardation of the flow velocity takes place as the freestream streamtube area increases prior to the inlet. Inlet lip design is typically built around the high-speed cruise condition to eliminate flow separation. The mass flow ratio increases to values greater than 1.0 during a typical

climb condition. The inlet lip and throat design should also allow for this condition to be accepted with minimal losses due to flow separation. Ground running corresponds to an extreme static or low speed condition that can lead to flow separation near the inlet lip due to the sharp turning angle of the freestream streamlines. A slotted inlet lip may be used to improve flow quality at these low speed conditions [13]. At the top speed condition, the captured freestream streamtube area decreases below the value of the high-speed condition, which leads to a further adverse pressure gradient in the pre-entry region. In the presence of an external boundary layer, this may cause severe regions of separated flow that can potentially cause engine surge. Boundary layer bleeds are often used to mitigate losses associated with the top speed flight condition.

In summary, the external flow field provides the input conditions to the inlet system. It is important to consider the behavior of external boundary layers and freestream streamlines in terms of the position of the inlet entrance face on the aircraft, as well the inlet lip design, over a wide range of flight conditions.

3.2.1 Flow in Straight Pipes

Once the flow enters the inlet, the presence of the surrounding surfaces causes a change in the flow behavior. The behavior of flow in a straight pipe is fundamental to the understanding of more complex flow behavior in a curved pipe. It is also particularly important to understand in the case where a constant-area extension is placed upstream and/or downstream of an s-duct inlet. In 1840, Poiseuille published experimental work that studied the relationship between volumetric flow rate through straight tubes of

varying diameter and driving pressure [22]. He also considered temperature effects. Results showed that the flow within the pipe became “fully developed” after a certain downstream distance from the pipe entrance, meaning that specific flow relationships become linear, as outlined in Fig. 29.

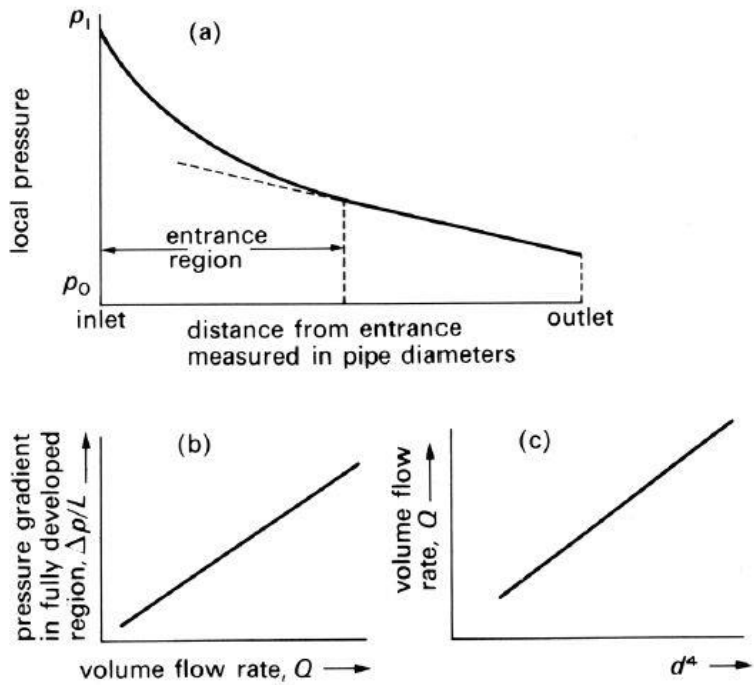


Figure 29 Important results of Poiseuille experiments. (a) Change in local lateral pressure with distance from pipe entrance, (b) Linear change in pressure gradient with volumetric flow rate in fully developed region, (c) Linear change in volumetric flow rate with pipe diameter. Figure obtained from [22]

The result of these experiments was Poiseuille law, which qualitatively states that within the fully developed region of a long horizontal pipe of constant circular diameter,

the viscous force operating at the tube wall on a steady-state Newtonian fluid is equivalent to the favorable pressure gradient force that drives the flow through the pipe. His experimental results along with subsequent derivations from fundamental equations of fluid mechanics led to the following relationship between pressure, viscosity, volumetric flow rate, and the dimensions of the straight pipe.

$$\Delta p = -128 \frac{\mu L Q}{\pi d^4} \quad (10)$$

$$Q = \frac{K P d^4}{L} \quad (11)$$

An important result of these equations is the dominant effect of the pipe diameter on the required pressure difference to drive the flow through the pipe in the fully developed region. If the pipe diameter decreases, the driving pressure must increase by a power of four to maintain the same volume flow rate. In terms of an s-duct inlet design, these relationships likely do not strictly apply because the required pipe length to observe fully developed flow can be upwards of $100d$ [22], however the progression of the velocity profile through the pipe will increasingly resemble the theoretical parabolic velocity distribution of fully developed flow defined below by Eqn. 12.

$$u = 2\bar{U} \left(1 - \frac{r^2}{a^2}\right) \quad (12)$$

The more likely scenario in terms of an s-duct inlet design is that the flow is not fully developed in the entrance region. This is important because it helps to understand the general shape of the velocity profile that enters the s-duct. Assuming the freestream velocity profile is uniform, the velocity profile in the entrance region of a pipe gradually adjusts to the presence of viscous effects imposed by the near wall. Near-wall viscous effects in the entrance region cause two main effects: (1) a retardation of the flow velocity near the wall coupled with (2) a convective acceleration of the flow near the pipe centerline to maintain a constant flow rate. The evolution of a typical velocity profile in the entrance region of a pipe is illustrated below in Fig. 30.

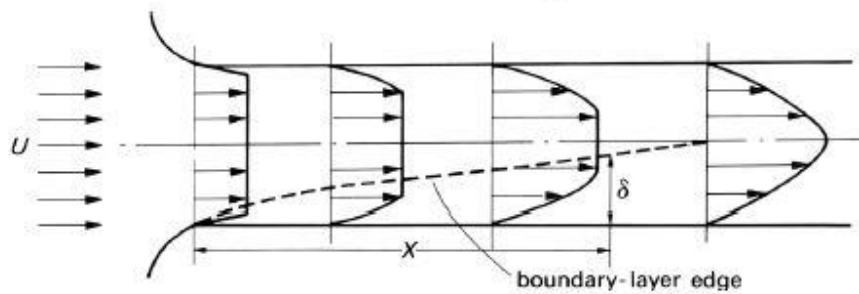


Figure 30 Evolution of the velocity profile in the entrance region of a pipe due to near-wall viscous effects

Figure 30 also highlights the importance of the growth of the boundary layer in terms of the velocity profile in the entrance region of a pipe, which depends on the Reynolds number of the flow. A laminar flow will require a longer pipe length than a turbulent flow to become fully developed. Nearly all s-duct inlets for aircraft applications operate in the turbulent flow regime. The Reynolds number (Re) is often used to differentiate between laminar and turbulent flow regimes. In a physical sense, the Reynolds number represents the ratio of the inertial properties of the fluid to the viscous properties of the fluid. For a pipe of arbitrary cross-sectional shape, the Reynolds number is defined below by Eqn. 13. In Eqn. 13, ρ is the fluid density, U is the mean flow velocity, μ is the dynamic viscosity of the fluid, A is the cross-sectional area of the inlet, and P represents the perimeter of the inlet.

$$Re = \frac{\rho U D_{eq}}{\mu}, \quad \text{where } D_{eq} = \frac{4A}{P} \quad (13)$$

In a circular pipe, the hydraulic diameter (D_{eq}) reduces to the pipe diameter. The flow is considered laminar for $Re < 2300$, transitional for $2300 < Re < 2500$, and turbulent for $Re > 2500$ [22]. It is important to note that the time-average velocity profile of turbulent pipe flow resembles a much blunter profile in the interior of the pipe than in laminar flow. The velocity gradient at the wall is much greater as a result.

An approximation of the entrance length for a turbulent flow is provided by [22] in Eqn. 14 below. In Eqn. 14, X represents a downstream distance from the entrance and d corresponds to the pipe diameter.

$$\frac{X}{d} = 0.693Re^{1/4} \quad (14)$$

The entrance length estimation can provide insight into the shape of the velocity profile that enters an s-duct inlet. It is important to emphasize that a uniform freestream flow is also assumed in the previous description of pipe flow. In an inlet design, additional freestream effects must be considered such as the mass flow ratio and inlet lip shape, which will alter the properties of the entrance flow.

3.2.2 Flow in Curved Pipes

It is important to understand the general flow effects of pipe curvature because it is fundamental to the secondary flow behavior that is common in an s-duct inlet. Flow in a curved pipe introduces the additional effect of centripetal acceleration on the fluid that is supplied by a transverse pressure gradient. The pressure gradient is relatively uniform over the cross-section [22], and it provides a centripetal acceleration ($\sim \frac{\rho u^2}{r}$) that acts perpendicular to the flow direction towards the inside of the pipe bend.

Centripetal acceleration combined with the velocity profile at the entrance of the pipe bend causes secondary flow behavior that acts within the cross-sectional plane of the pipe, as seen below in Fig. 31. Faster flow near the centerline of the pipe reacts more slowly to the centripetal acceleration due to its higher inertia, which causes a distortion of the Poiseuille velocity profile that shifts the faster moving flow toward the outside of the bend. The flow at the centerline is replaced by slower moving fluid from the inside of the bend. In theory, the flow forms two symmetric counter-rotating recirculation regions in the transverse plane of the flow. These secondary motions appear downstream of the bend as twin counter-rotating vortices that vary in strength depending on the pipe geometry and flow conditions.

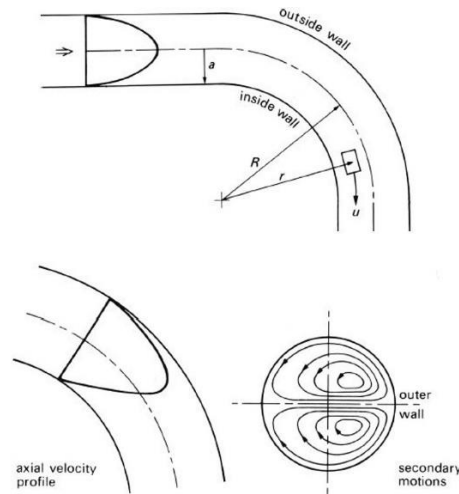


Figure 31 Poiseuille velocity profile entering a pipe bend with a constant radius of curvature, R . A fluid element traveling through the bend at a velocity, u , experiences a radial acceleration proportional to $\rho u^2/r$. The centripetal acceleration and velocity profile induces secondary flow. Figure obtained from [22].

The previous explanation suggests that the greatest velocity occurs at the outside of the bend due to the distortion of the Poiseuille velocity profile, however this is not observed in experiments in which the velocity profile at the entrance of the bend is flat (shown below in Fig. 32). Experiments show that the velocity of the fluid near the inside wall is greater than that near the outside wall [22].

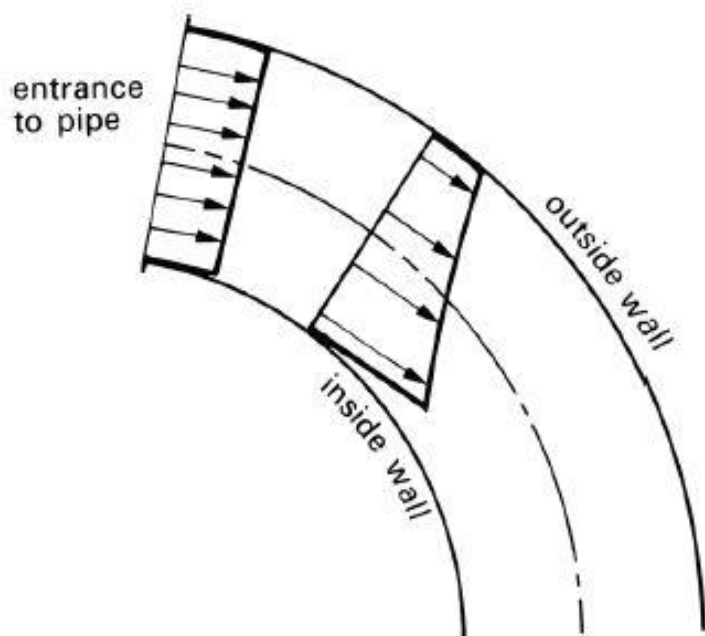


Figure 32 Flat velocity profile entering a curved pipe. Highest velocity occurs near the inside wall of the bend. Figure obtained from [22]

This velocity profile along the bend is explained by Bernoulli's theorem (assuming gravity forces are negligible), which relates pressure and velocity along a streamline for a steady, incompressible, and inviscid flow.

$$p_1 + \frac{1}{2}\rho u_1^2 = p_2 + \frac{1}{2}\rho u_2^2 = \text{constant} \quad (15)$$

Equation 15 is applicable in understanding the increased flow velocity observed near the inside wall of the pipe bend because the pressure is greater near the outside wall than near the inside wall. As shown in Fig. 32, pressure and velocity are uniform at the entrance to the pipe, therefore the velocity must increase along a streamline near the inside wall. It is important to note that Bernoulli's equation can only be reasonably applied along a streamline that is outside of the boundary layer, where it is assumed that viscous shear effects are minimal in the interior flow of the pipe.

A mathematical solution was proposed by Dean [23] in 1928 that confirmed the transverse streamline behavior of the secondary flow in a curved pipe. The results were obtained from the steady motion of laminar, incompressible fluid through a pipe of circular cross-section coiled in a circle of small curvature. Strict application of the analytical equations is limited due to a list of necessary approximations that enable a simplification of the Navier-Stokes equations, however the results provided important mathematical insight into the cross-sectional streamline behavior inherent to the

secondary flow structure that forms in an s-bend geometry. An important conclusion from the analytical research was that flow rate decreased with increased pipe curvature. The decrease in flow rate due to curvature was determined to depend on a single variable now known as the Dean number, which is often described by Eqn. 16 below,

$$K = Re \sqrt{\frac{D}{2R_c}} \quad (16)$$

where D is the pipe diameter and R_c is the pipe radius of curvature. The Reynolds number is typically calculated based on the mean axial velocity at the entrance of the bend. The general importance of the Dean number is to predict the formation and strength of secondary flow structures in a curved pipe. Eqn. 16 highlights the importance of pipe curvature ($D/2R_c$). The flow becomes turbulent at large Dean numbers and causes asymmetric, oscillatory behavior of the Dean vortices [24].

Ligrani [25] studied the flow in a curved channel with mild curvature for a range of Dean numbers from 35 to 430. The results showed that at low Dean numbers (<40-60) the flow was fully laminar. Small secondary flow structures began to form for Dean numbers between 40-75. Secondary instabilities in the vortex pairs were seen for Dean numbers between 75 and 200, where the vortex pair demonstrated undulations, twisting, splitting, and merging.

Berger et al. [26] provided a comprehensive analysis of flow in curved pipes over a wide range of conditions. Both steady and unsteady flows were considered in infinitely coiled pipes as well as finite bends. Thermal effects, multiphase flow, non-Newtonian fluids, and flexible wall effects were also analyzed. The main emphasis was on the understanding of secondary flow within pipes with circular cross-sections due to the transverse pressure gradient.

3.3 Inlet Performance Parameters

Steady-state pressure recovery and total pressure distortion are chosen as the primary inlet performance evaluators in this thesis. Both performance parameters are evaluated at the Aerodynamic Interface Plane (AIP), defined as a circular or annular section of an inlet duct that is located as close as practically possible to the engine-face plane [27]. The comparisons to literature in Chapter 4 of this thesis utilize the definition of pressure recovery in Eqn. 17 as the ratio between the area-weighted average total pressure at the AIP to the freestream total pressure.

$$\eta_{02} = \frac{P_{T,AIP}}{P_{T,\infty}} \quad (17)$$

The physical importance of pressure recovery for subsonic inlets is that it provides a quantitative measurement of the total losses in the inlet due to friction on the inlet walls and any external surface area wetted by the flow that enters the inlet. Pressure recovery also accounts for turbulent mixing associated with flow separation or near-separation [13].

Seddon and Goldsmith [13] provide a rough approximation that relates the total pressure loss in an inlet system (ΔP_T) to the loss of engine thrust, given by Eqn. 18.

$$\frac{\Delta X}{x} = 0.35 K M_\infty \frac{\Delta P_T}{q_\infty} \quad (18)$$

In Eqn. 18, the change in engine thrust is denoted as ΔX , and K is an empirical factor dependent on the engine but is generally close to a value of 1.5. The approximation is adequate for $0.5 < M_\infty < 1$.

Total pressure distortion at the AIP can be quantified in terms of circumferential and radial elements. It is widely considered as an important parameter to consider in the determination of inlet/engine compatibility. Inlet/engine compatibility is often determined by the total pressure distortion effect on compressor stability margin for a turbine engine. The following equations and explanations of recommended practices were obtained by Revision B of SAE Aerospace ARP1420 [27]. These recommended

practices served as an important tool to evaluate the performance of the proposed XQ-1A inlet design.

The level of assessment necessary to fully evaluate inlet/engine compatibility is beyond the scope of this thesis, however it is useful to generally understand the relationship between AIP total pressure distortion level descriptors and engine performance.

The stability margin (SM) of the engine is an engine performance parameter that is considered important for inlet/engine compatibility assessments. It is defined in Eqn. 19 as the pressure ratio range (at a constant corrected airflow) through which a compressor may be operated. An example of a compressor performance map in Fig. 33 illustrates a representative reduction in stability margin due to increased flow distortion.

$$SM = \left(\frac{PR_1 - PR_0}{PR_0} \right) * 100 \quad (19)$$

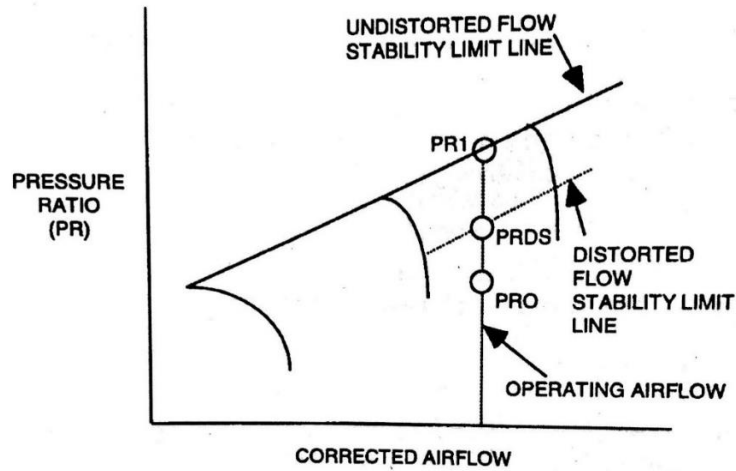


Figure 33 Stability margin definition [27]

The stability margin is limited by the operating pressure ratio (PRO) and the compressor stability limit line ($PR1$). The compressor stability limit line represents the upper operational limit set to avoid the occurrence of aerodynamic instability or aeromechanical failure. The overall negative effect of pressure distortion at the AIP is a reduction of the compressor stability limit line that results in a lower stability margin.

In a proper assessment of engine stability, the change in stability margin must be accounted for over the entire corrected-airflow operating range under conditions that lower the compressor stability limit line and raise the operating point. The following additional performance parameters must also be considered: “time-variant inlet distortion, in-phase pressure oscillations, component interactions, deterioration, component variation due to manufacturing tolerance, control tolerances, variable-geometry position, power-level transients, operating-point shift with distortion, Reynolds number effect,

compressor bleed, and horsepower extraction” [27]. Due to common experimental and computational limitations, much of the analyses of these inherently complicated effects rely heavily on the use of steady-state (time-averaged) performance descriptors.

Pressure distortion at the AIP is measured experimentally through a total pressure rake array, as shown below by Fig. 34. A typical array contains eight rakes spaced equally by 45° with five probes at each rake. The probes are typically separated radially such that they are located at the centroids of equal areas. An array in this typical geometry forms five rings of pressure measurements that can be used to linearly interpolate the circumferential and radial pressure distortion at the AIP.

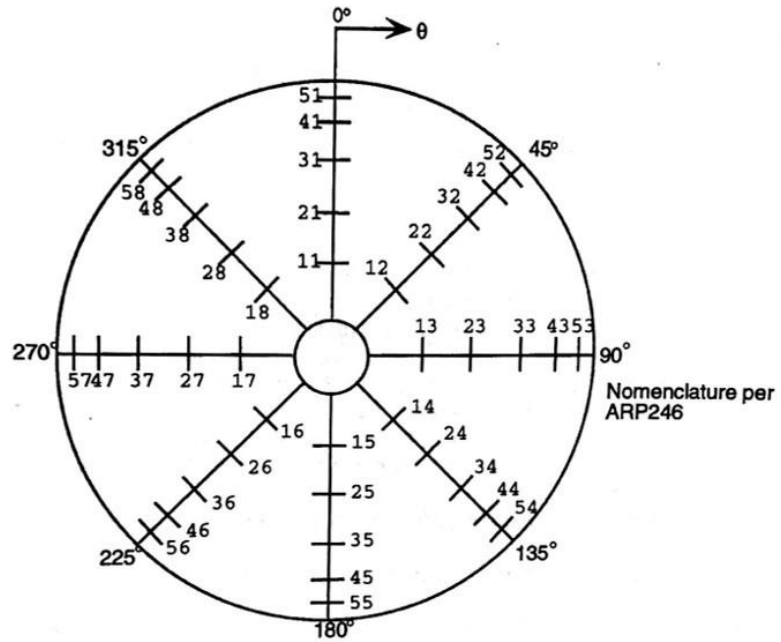


Figure 34 Typical probe/rake array [27]

Circumferential pressure distortion is described at each ring of the rake array in terms of intensity, extent, and multiple-per-revolution elements. The intensity element represents the magnitude of the pressure distortion. The extent element represents the circumferential angular size of the low-pressure region. The multiple-per-revolution element represents the number of low-pressure regions within a single ring, relative to the average total pressure of the corresponding ring. For example, a “one-per-rev” pattern represents the occurrence of a single low-pressure region along the circumference of a pressure measurement ring.

The full definition of pressure distortion extent and intensity are defined below by Eqn. 20 and Eqn. 21, respectively, following the nomenclature used in [27].

$$\text{Extent: } \theta_i^- = \theta_{2i} - \theta_{1i} \quad (20)$$

$$\text{Intensity: } \left(\frac{\Delta PC}{P} \right)_i = \left(\frac{PAV - PAVLOW}{PAV} \right)_i \quad (21)$$

$$PAV_i \equiv \text{Ring Average Pressure} = \frac{1}{360} \int_0^{360} P(\theta)_i d\theta$$

$P(\theta)_i$ is a function resulting from a linear fit between data points

$$PAVLOW_i \equiv \text{Average Low Pressure} = \frac{1}{\theta_i^-} \int_{\theta_{1i}}^{\theta_{2i}} P(\theta)_i d\theta$$

The circumferential total pressure distribution can be plotted, as shown by example in Fig. 35 below, for a given measurement ring to visualize the intensity and extent of a one-per-rev pattern.

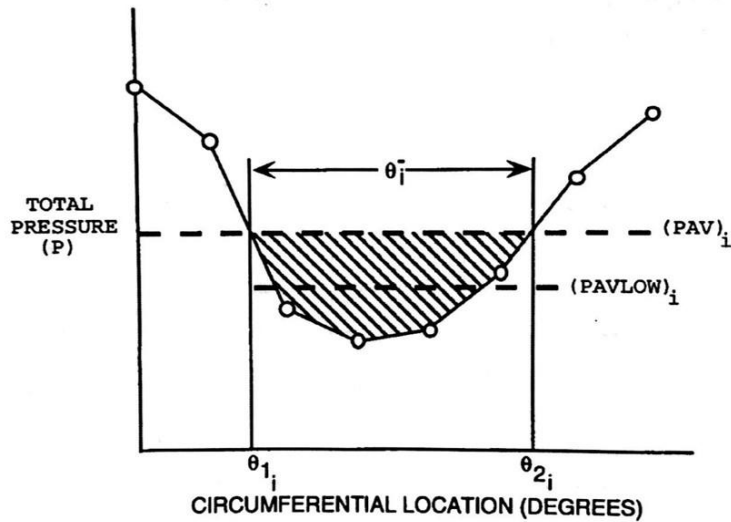


Figure 35 Example of ring circumferential intensity and extent distortion elements for a one-per-revolution pattern [27]

Multiple-per-rev patterns occur when two low-pressure regions are separated by two high-pressure regions within the circumference of a single measurement ring, as shown below in Fig. 36. Special treatment is applied to this case to determine the level of variation within the circumferential distortion based on a high-pressure extent threshold value (θ_{min}^+). A comparison between the extent of the surrounding high-pressure regions and the high-pressure extent threshold value determine the appropriate modifications to

the interpretation of the ring's intensity, extent, and equivalent multiple-per-revolution elements.

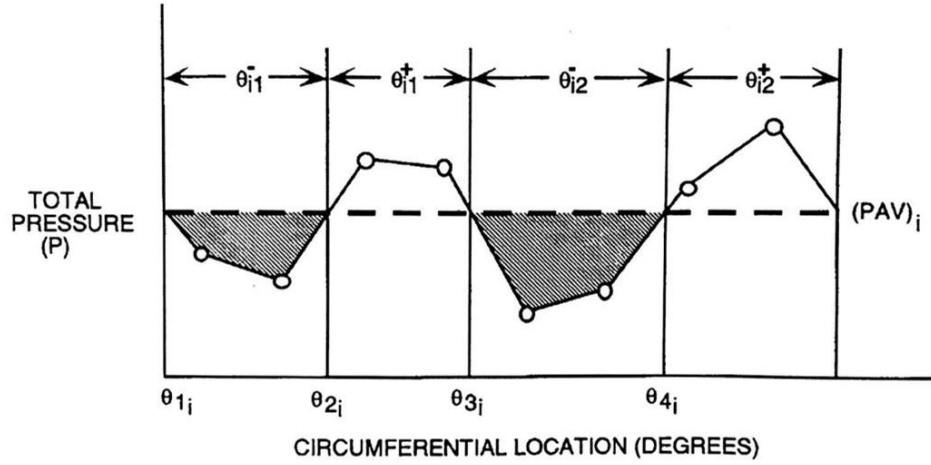


Figure 36 Example of ring circumferential distortion for a multiple-per-revolution pattern [27]

A high-pressure extent threshold value of 25° is used for MPR distortion element calculations in this thesis, per suggestion by [27].

A low-pressure region with a surrounding high-pressure region extent (θ_{ik}^+) less than or equal to θ_{min}^+ is considered as an equivalent one-per-revolution low-pressure region, and receives the following treatment of extent and intensity below.

$$\text{Extent: } \theta_i^- = \sum_{k=1}^Q \theta_{ik}^- \quad (22)$$

$$Intensity: \quad \left(\frac{\Delta PC}{P} \right)_i = \frac{\sum_{k=1}^Q \left[\left(\frac{\Delta PC}{P} \right)_{ik} \theta_{ik}^- \right]}{\sum_{k=1}^Q \theta_{ik}^-} \quad (23)$$

A low-pressure region with a surrounding high-pressure region extent (θ_{ik}^+) greater than θ_{min}^+ is considered as a multiple-per-revolution element with a value greater than unity. Intensity, $\left(\frac{\Delta PC}{P} \right)_i$, is the $\left(\frac{\Delta PC}{P} \right)_{ik}$ that corresponds to the maximum value of $\left[\left(\frac{\Delta PC}{P} \right)_{ik} \theta_{ik}^- \right]$. Likewise, circumferential distortion extent, θ_i^- , is the θ_{ik}^- corresponding to the maximum value of $\left[\left(\frac{\Delta PC}{P} \right)_{ik} \theta_{ik}^- \right]$. The multiple-per-revolution element is a measure of equivalent low-pressure regions observed within the ring, calculated as the ratio of the total integrated area beneath PAV_i to the largest single area beneath PAV_i .

$$Multiple - per - rev: \quad MPR_i = \frac{\sum_{k=1}^Q \left[\left(\frac{\Delta PC}{P} \right)_{ik} \theta_{ik}^- \right]}{\left[\left(\frac{\Delta PC}{P} \right)_{ik} \theta_{ik}^- \right]_{max}} \quad (24)$$

Radial distortion intensity is defined below as the difference between the face-average total pressure and the ring-average total pressure.

$$\text{Radial Intensity: } \left(\frac{\Delta PR}{P} \right)_i = \frac{PFAV - PAV_i}{PFAV} \quad (25)$$

$$PFAV \equiv \text{Area weighted face average pressure} = \frac{1}{N} \sum_{i=1}^N PAV_i$$

$$N \equiv \text{total number of rings in rake}$$

In practice, both circumferential and radial distortion elements can be summed, as shown in Eqn. 26, to obtain an empirical relationship for the loss of compressor stability pressure ratio as a percent of the undistorted stability pressure ratio:

$$\Delta PRS = \sum_{i=1}^N \left[KC_i * \left(\frac{\Delta PC}{P} \right)_i + KR_i * \left(\frac{\Delta PR}{P} \right)_i + C_i \right] * 100 \quad (26)$$

The constants KC_i , KR_i , and C_i are empirically determined from test data involving the inlet/engine system. They serve to calibrate the distortion patterns to within $\pm 2\%$ of the stability pressure ratio. Finally, Eqn. 27 can be used to determine the loss of compressor stability margin (ΔSM).

$$\Delta SM = \left(\frac{PR1}{PR0} \right) * \Delta PRS \quad (27)$$

3.4 XQ-1A-1 Inlet Design

The following discussion of the “XQ-1A-1” inlet describes the preliminary inlet design approach, which was designed to fit the existing 1/3rd-scale XQ-1A fuselage geometry and the diameter of the JetCat-P20SX engine.

Figure 37 below demonstrates the general aspects of the inlet design. An important feature of the design is the “Downstream Parallel Extension” section, which is simply a constant area duct used to provide clearance for the JetCat P-20SX electric starter motor. The elliptical-to-circular s-duct section was defined using a sequence of five internal lofting planes.

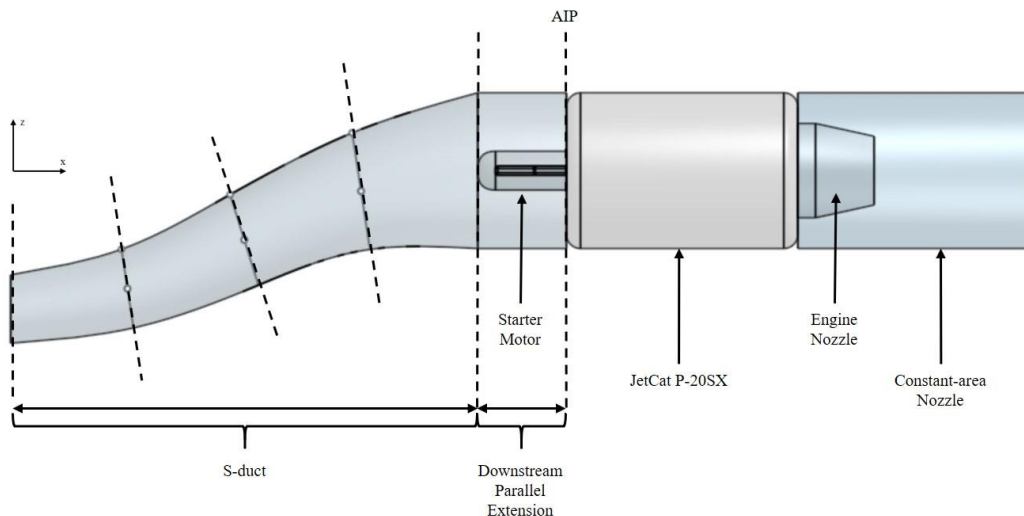


Figure 37 General configuration of s-duct inlet fit to JetCat P-20SX engine

It was desirable to limit the overall length (L) and offset (H) of the s-duct as much as possible in the preliminary design to limit losses due to internal friction and flow separation. An inlet length equivalent to five times the engine diameter ($L = 5\phi_{engine}$) was chosen as an appropriate length of the s-duct based on the estimated relative dimensions of the F-16 inlet ($L \approx 4.2\phi_{engine}$).

Choice of engine position was an important design parameter because it allowed for simultaneous achievement of the desired inlet length and a reasonable inlet entrance face position. The location of the engine was chosen as three engine diameters upstream of the rear end of the fuselage, which effectively positioned the entrance face of the s-duct at approximately $x/L_{fuselage} = 0.44$, with x measured from the front of the fuselage. Figure 38 below shows the XQ-1A-1 inlet length dimension relative to the lower half of the fuselage.

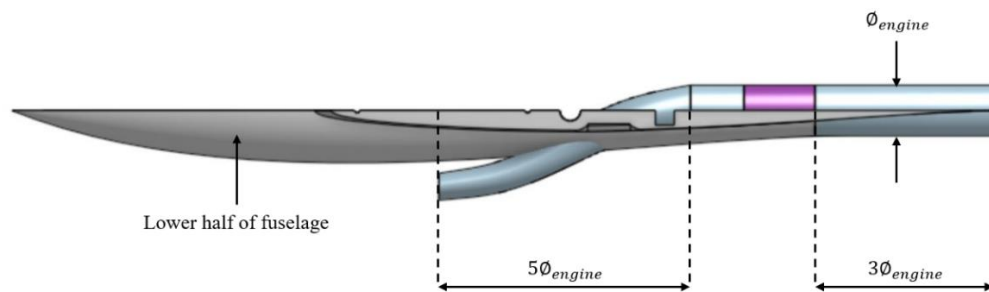


Figure 38 XQ-1A-1 design choice of engine position and relative inlet/nozzle lengths.
(JetCat P-20SX engine highlighted in purple)

S-duct offset was important in terms of a balance between consideration of internal flow separation and fuselage boundary layer ingestion. Large s-duct offset results in less ingestion of the fuselage boundary layer because it locates the inlet entrance face away from the fuselage, however large offset also results in large regions of separated internal flow due to increased flow turning angles and increased drag. Boundary layer ingestion and internal flow separation also depends on flight conditions. The perfect design tradeoff for all flight conditions is likely not possible given the wide range of flight conditions expected for a typical XQ-1A mission profile.

A 0.5-inch boundary layer diverter height was chosen as reasonable for the XQ-1A inlet, which effectively established an inlet offset of $H = 1.514\phi_{engine}$. For comparison, Raymer [4] provides an estimation of appropriate boundary layer diverter height as approximately 1-3% of the fuselage length in front of the inlet, which results in a range of diverter heights of 0.2-0.6 inches when applied to the XQ-1A geometry. It was also found that the chosen boundary layer diverter height of 0.5 inches is roughly eight times larger than a flat plate approximation of the fuselage turbulent boundary layer displacement thickness [28], calculated as 0.0685 inches using Eqn. 28 below. In Eqn. 28, δ^* represents boundary layer displacement thickness, x represents the flat plate length at the location of interest. The flat plate length corresponds to an approximation of the fuselage length between the front of the fuselage and the inlet entrance face. The calculation of displacement thickness assumes a near-stall flight speed of 30 kts at sea level conditions and uses a flat plate length of 20.03 inches.

$$\delta^* \cong \frac{0.048x}{(Re_x)^{1/5}} = 0.0685'' \quad (28)$$

Other important parameters that determined the inlet offset included the fuselage diameter at the location of the inlet entrance face and the semi-minor axis length of the elliptical cross-section at the inlet entrance face. Figure 39 below shows the relevant dimensions that determined the inlet offset of $H = 1.514\phi_{engine}$.

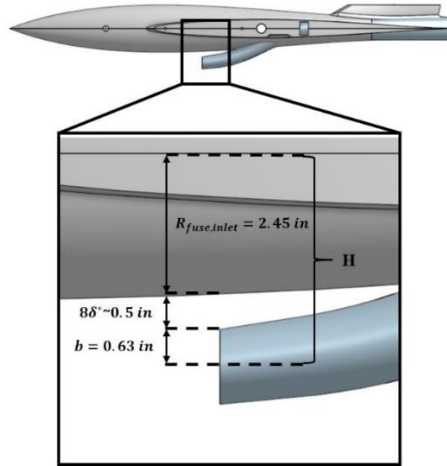


Figure 39 Dimensions relevant to the XQ-1A-1 inlet offset

The XQ-1A-1 inlet used six lofting planes to define the full geometry, as shown below in Fig. 40. The centerline curvature was defined in reference to a straight line

connected between the geometric centers of the inlet entrance face and the entrance face of the downstream parallel extension. Internal lofting planes were equally spaced. Planes located at $x/L = 0.20, 0.60$ were vertically offset from the straight reference line to define the geometric centers of the corresponding cross-sectional areas. The centerline was then defined using a spline that connected the geometric center of each lofting plane.

It was eventually decided that this parameterization of the geometry, particularly in terms of the centerline curvature, was not suitable for future design trade studies. It was also difficult to achieve a smooth surface transition near the interface between the s-duct and the downstream parallel extension. Due to these reasons, the performance of the XQ-1A-1 inlet was not analyzed in detail. However, important dimensions of length ($L = 5\phi_{engine}$) and offset ($H = 1.514\phi_{engine}$) relative to the engine diameter were established and maintained in the XQ-1A-2 inlet design.

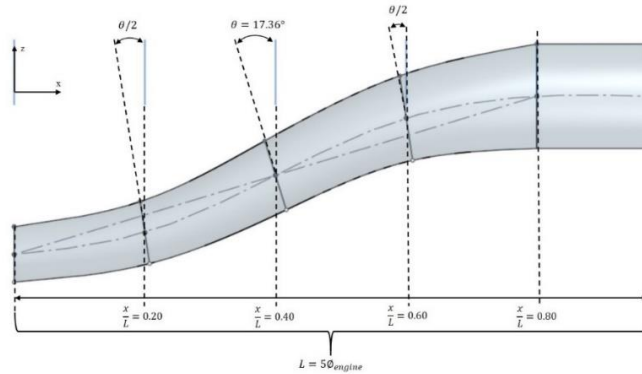


Figure 40 XQ-1A-1 inlet lofting planes and s-duct centerline

CHAPTER 4. COMPUTATIONAL FLUID DYNAMICS

4.1 Previous CFD Work on S-duct Inlets

S-duct inlets have been analyzed previously in detail using CFD. Relevant studies include, but are not limited to, the effects of centerline curvature, length, offset, flow turning angle, cross-sectional shape, incidence angle, and boundary layer ingestion on pressure recovery and flow distortion at the AIP. Higher-order computational models have also been used to predict time-variant flow behavior in diffusing s-duct inlets.

Towne and Schum [29] used a parabolic three-dimensional Navier-Stokes CFD code to assess the effects of centerline curvature and transitioning cross-sections in complex inlet designs. Results showed that distortion at the AIP was driven mainly by centerline offset and the thickness of the boundary layer at the diffuser entrance. The transition of diffuser cross-sections was determined to have a secondary effect on the overall pressure loss in the inlet.

Papadopoulos et al. [30] used RANS equations and a shear stress transport two-equation turbulence model to evaluate an s-duct inlet designed for a UAV application. The inlet utilized a loft between a rectangular cross-section with rounded corners to a circular cross-section at the AIP, which were designed using Gerlach area shaping. Gerlach area shaping focuses on a variation of cross-sections to increase the outer wall velocity and decrease the inner wall velocity at the first turn to effectively decrease the transverse pressure gradient and formation of secondary flow. The custom s-duct was designed for a freestream Mach number of 0.85 at an altitude of 6,000 m, and an engine

mass flow rate of 1.38 kg/s. The inlet used an offset equivalent to two times the engine face diameter, an area ratio of 1.782, and varied the inlet length-to-engine face diameter ratio from approximately 0.8 to 1.7. The near-double increase in inlet length resulted in an approximate 1.5% decrease in pressure recovery due to frictional losses, however added benefit was observed in terms of flow distortion at the AIP.

Gopaliya et al. [31] presented the effects of inlet offset on the performance of an s-duct diffuser with a 90°/90° turn. The inlet cross-sectional geometry lofted between a rectangular inlet to a semicircular outlet. Results showed that increased inlet offset resulted in reduced pressure recovery and increased flow non-uniformity at the exit.

Gupta et al. [32] used CFD to investigate the change in performance of s-shaped rectangular diffusers due to flow turning angles of 15°/15°, 22.5°/22.5°, 45°/45°, and 90°/90° and various aspect ratios. It was observed that flow uniformity decreased, and cross flow velocities increased as turning angle increased.

Lee and Cho [33] employed three-dimensional RANS equations and a k- ω -based shear stress transport model to test the effect of varying cross-sectional shape of the RAE-M2129 inlet geometry. A total of 21 test cases were performed that varied the aspect ratio such that cross-sections with upper-half semicircular and lower-half semicircular shapes were analyzed. Performance metrics were pressure recovery and distortion. A flight Mach number of 0.21 at zero angle of attack was used in the study, with a large mass flow ratio of 23.245. Results showed that the upper-half semicircular shapes delivered the best performance, while the circular case exhibited the worst.

Menzies [34] performed RANS simulations using various turbulence models to test the performance of the RAE-M2129 inlet at a variety of angles of pitch and yaw. Positive angles of yaw showed a reduction of inlet distortion and an increase of pressure recovery due to the lowered effect of offset. Negative angles of yaw accentuated the effect of offset and caused lower inlet performance. Computational work related to engine surge was also performed to assess the performance of the RAE-M2129 inlet, however no experimental data was available for validation.

Berrier and Allan [35] used experimental and computational methods to evaluate the performance of four flush-mounted s-duct inlet geometries over a range of Mach numbers and with large amounts of boundary layer ingestion. Tests were conducted at Mach numbers from 0.25 to 0.83. Steady-state RANS equations were solved to represent the computational model, and $k-\omega$ Shear Stress Transport (SST) was used to model turbulence. Results showed that pressure recovery generally decreased and distortion increased with increasing Mach number, except at low Mach numbers in the range of 0.25-0.4, where it was observed that pressure recovery increased. Computational predictions showed more pessimistic results for pressure recovery compared with the experimental results.

Gil-Prieto et al. [36] compared Delayed Detached-Eddy Simulation (DDES) with high-resolution, synchronous stereoscopic particle image velocimetry (SPIV) measurements to characterize dynamic flow distortion at the AIP of a circular cross-sectional s-shaped inlet. Proper Orthogonal Decomposition (POD) was used to identify the most energetic coherent turbulent structures that occur in a typical s-duct flow field.

Four distinct modal distributions were identified in both the DDES modeling and SPIV measurements, labeled as follows: first switching mode, second switching mode, first vertical mode, and second vertical mode. The switching modes, outlined in Fig. 41, are characterized by an alternately dominant streamwise vortex, shed downstream of the separation region. The dominant streamwise vortex propagates to the lower section of the AIP and a second opposite-rotating vortex forms above, which eventually dominates the original structure and forms the “swirl-switching” mechanism. In general, the switching modes cause a circumferential change in the primary region of pressure loss at the AIP. The first and second vertical modes are related to the vertical change in the primary region of pressure loss due to vortex shedding from the unsteadiness of the shear layer along the s-duct centerline. The freestream Mach number was 0.27. The s-duct had a centerline offset of $H/L = 0.5$, an area ratio of $D_{exit}/D_{inlet} = 1.52$, and length $L/D_{inlet} = 4.95$.

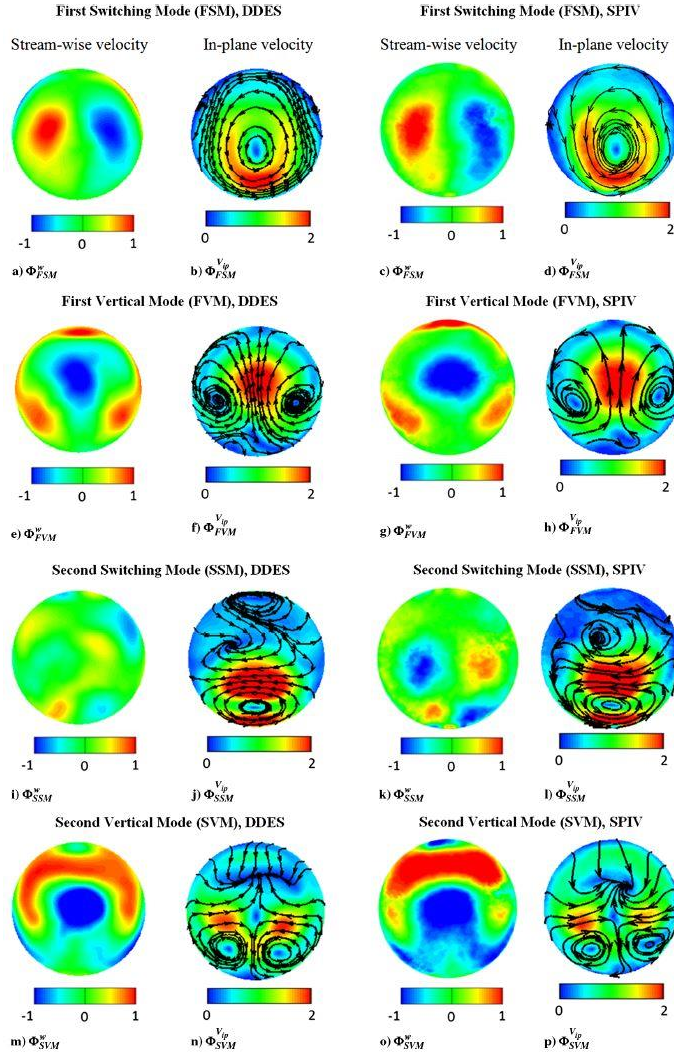


Figure 41 Four coherent turbulent modes found in [36] using DDES and SPIV

4.2 Governing Equations and Turbulence Modeling

The following section provides a brief outline of the governing equations for the CFD analyses discussed within this thesis. The outline is guided by the relevant physics models described below in Fig. 42, and Simcenter's STAR-CCM+ Theory guide [37].



Figure 42 Continua physics models

In general, fluid flow simulations attempt to model the macroscopic behavior of the flow as a continuum within a discretized computational domain. In this thesis, an Eulerian approach was used to model the fluid flow through the definition of a fluid domain containing the inlet. The domain was divided into a finite number of small control volumes that represent the volume mesh. Discrete versions of the integral form of the conservation equations were solved at each control volume to simulate the flow field properties over the full computational domain. It was determined that steady-state Reynolds-Averaged Navier-Stokes (RANS) equations would serve as an appropriate approximation to the full Navier-Stokes (N-S) equations, given that close agreement

between experimental and previous CFD data has been shown in literature, specifically in terms of inlet pressure recovery [38].

The numerical solution of the RANS equations resolves the transport of the mean flow quantities as a turbulence approximation to the direct numerical simulation of the full N-S equations. Lack of fidelity in terms of instantaneous turbulent properties of the flow is balanced by significant savings in terms of computational resource requirements. The RANS equations are obtained through a substitution of the instantaneous solution variables (\emptyset), decomposed into the addition of their corresponding mean ($\bar{\emptyset}$) and fluctuation components (\emptyset'). The instantaneous solution variables of interest in this thesis include velocity and pressure. The enabled Segregated Fluid Isothermal model in STAR-CCM+ treats temperature as a constant of 300 K throughout the computational domain. This approximation was made due to the low-speed nature of the flow in order to reduce the use of unnecessary computational resources.

The RANS equations (in absence of body forces) are outlined as follows:

$$\text{Mean Mass Transport: } \frac{\partial \rho}{\partial t} + \nabla \cdot [\rho(\bar{\mathbf{v}} - \mathbf{v}_g)] = 0 \quad (29)$$

where ρ is the fluid density, $\bar{\mathbf{v}}$ is the continuum velocity. The \mathbf{v}_g variable is a reference frame velocity relative to the laboratory frame, which is zero for all simulations in this thesis.

$$\text{Mean Momentum Transport: } \frac{\partial}{\partial t}(\rho \bar{\mathbf{v}}) + \nabla \cdot [\rho \bar{\mathbf{v}}(\bar{\mathbf{v}} - \mathbf{v}_g)] = -\nabla \cdot \bar{p}\mathbf{I} + \nabla \cdot (\mathbf{T} + \mathbf{T}_{\text{RANS}}) \quad (30)$$

In Eqn. 30, \bar{p} is the mean pressure, \mathbf{I} is the normal stress tensor, and \mathbf{T} is the viscous stress tensor. The Reynolds stress tensor, \mathbf{T}_{RANS} , is an important addition to the original NS equations. As defined below, it is related to the mean of the fluctuation components of velocity.

$$\mathbf{T}_{\text{RANS}} = -\rho \begin{bmatrix} \overline{u'u'} & \overline{u'v'} & \overline{u'w'} \\ \overline{u'v'} & \overline{v'v'} & \overline{v'w'} \\ \overline{u'w'} & \overline{v'w'} & \overline{w'w'} \end{bmatrix} \approx 2\mu_t \mathbf{S} - \frac{2}{3}(\mu_t \nabla \cdot \bar{\mathbf{v}})\mathbf{I} \quad (31)$$

The right side of Eqn. 31 is known as the Boussinesq approximation, where \mathbf{S} is the mean strain rate tensor, and μ_t is the turbulent eddy viscosity that allows for the Reynolds stress tensor to be modeled as a function of mean flow quantities. The simulations in this thesis use the Shear-Stress-Transport (SST) K-Omega (Menter) eddy viscosity model to provide closure to the system of governing equations.

Fundamentally, the SST K-Omega models solves transport equations to determine the turbulent eddy viscosity. The transport equations are solved for the turbulent kinetic energy (k) and the specific dissipation rate (ω). The specific dissipation rate is defined as the dissipation rate (ε) per unit turbulent kinetic energy.

Reported advantages of the K-Omega model over similar eddy viscosity models (K-Epsilon, for example), include improved simulation of boundary layers under adverse pressure gradients. This was an important factor in the determination of an appropriate turbulence model for the following simulations, as an adverse pressure gradient inherently exists throughout the diffusing inlet. The Standard K-Omega models have noted sensitivity to inlet boundary conditions for internal flows, therefore the simulations in this thesis utilize the SST K-Omega (Menter) model. The modified model attempts to mitigate the issue of boundary condition sensitivity by adding a non-conservative cross-diffusion term to the transport equations, which effectively blends a K-Epsilon model in the far-field with a K-Omega model near the wall. The diffusion term is effective because the K-Epsilon model is insensitive to the values of the specific dissipation rate in the freestream.

The wall treatment is an important factor in the solution outcome because it determines the resolution of the boundary layer that forms along the inlet wall surfaces. The goal of the wall treatment is to apply empirical-based approaches to each of the three distinct boundary layer regions: the viscous sublayer, the log-law layer, and the buffer layer. The viscous sublayer comprises of the near-laminar fluid close to the wall and is dominated by viscous effects. The log-law layer exists in the outer region of the boundary layer and is affected equally by viscosity and turbulence. The buffer layer is a transitional region between the viscous sublayer and the log-law layer. The wall y^+ parameter, defined by Eqn. 32 below, is an important non-dimensional quantity that is used to evaluate the mesh quality near the wall.

$$y^+ = \frac{yu^*}{\nu} \quad (32)$$

In Eqn. 32, y represents the normal distance from the wall to the corresponding wall-cell centroid, u^* is a reference velocity, and ν is the kinematic viscosity. The wall treatment options provided by STAR-CCM+ include low- y^+ , high- y^+ , and all- y^+ . Figure 43 below highlights the differences in near-wall mesh refinement requirements for each wall treatment. The low- y^+ wall treatment requires the finest cell resolution near the wall because of its ability to solve the full transport equations to the near-wall cell without any additional modeling approximations. The high- y^+ treatment allows for the near-wall cell center to have a y^+ value greater than 30, as it does not resolve the viscous sublayer via the transport equations. Instead, the high- y^+ wall treatment uses wall functions and turbulent boundary layer theory to estimate the boundary layer. The hybrid all- y^+ wall treatment uses the local position of the near-wall centroid relative to the boundary layer to determine the local wall treatment. The high- y^+ approach is used in regions where the near-wall centroid is outside of the buffer layer. The low- y^+ approach is used in regions where the near-wall centroid is inside the viscous sublayer, and a blending function is used for near-wall centroids within the buffer region.

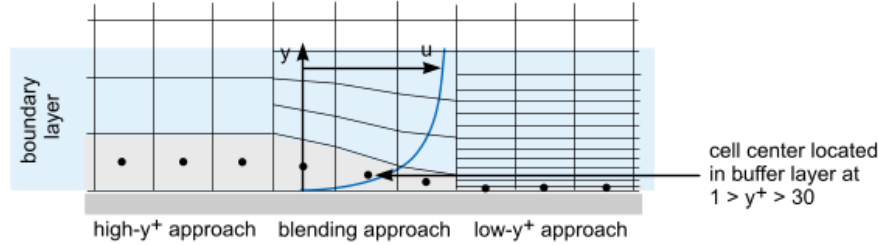


Figure 43 Summary of all- y^+ wall treatment [37]

The all- y^+ wall treatment is used in the following simulations to both limit computational resource requirements and reasonably resolve the boundary layer. For reasonable results using blending approach in the all- y^+ wall treatment, it is recommended practice to at least maintain wall y^+ values between 1 and 30.

4.3 RAE-M2129 Geometry

The Aerodynamics Action Group (AD/AG-43) for Aeronautical Research and Technology in Europe (GARTEUR) performed CFD studies to compare against experimental data provided by QinetiQ for the Royal Aircraft Establishment (RAE) M2129 S-diffuser [38]. RANS, unsteady RANS (URANS), and Detached Eddy Simulation (DES) simulations were used to better understand the flow physics and compare against experimental data. Large-scale time-dependent flow features and time-variant total pressure distortion at the AIP were most accurately predicted by DES simulations, however the results required significant computational resources. RANS and URANS simulations were not able to accurately resolve time-variant flow distortion at

the AIP, but other flow performance parameters such as pressure recovery were accurately represented. URANS results required additional computational resources and demonstrated minimal benefit in terms of time-averaged performance parameters. Given these results and computational resource limitations, RANS equations were chosen as an appropriate flow model for initial design iterations of the XQ-1A inlet.

The goal of the following analysis was to demonstrate a valid mesh and physics model that could be applied to a similar inlet geometry designed for the XQ-1A. The success of the mesh and physics model validation was evaluated in terms of the CFD results and their agreement with those given by experimental Data Point 69 (DP69) and the previous CFD work of GARTEUR AD/AG-43. Pressure recovery at the AIP was considered as the inlet performance parameter of greatest concern in terms of mesh validation given the expected limitations of RANS equations. The dynamic engine face rake used contained 8 equally spaced arms with 5 Pitot pressure probes on each arm to obtain experimental data at the AIP of the RAE-M2129. The arms were separated by 45° intervals. These experimental probe locations are used later in the CFD analyses in this thesis to evaluate total pressure distortion at the AIP. The radial positions of each probe ring are provided in Table 5.

Table 5 Radial positions of total pressure probe locations in QinetiQ experimental data

Ring	Radius [m]
1	0.02409
2	0.04173
3	0.05388
4	0.06375
5	0.07229

The experimental data referenced in this section was performed by the RAE in a closed-circuit, atmospheric, low-speed, 13-by-9 ft wind tunnel in 1990. Incidence and side-slip angles were not considered in the study. An ejector unit at the end of the inlet provided the pressure difference to drive the flow.

The geometry of the RAE-M2129 is defined by the following centerline equation (located at $y = 0$), cross-sectional diameter equation, and Table 6 below:

$$z = -0.15 \left[1 - \cos \left(\frac{\pi x}{L} \right) \right] \quad (33)$$

$$D = D_{throat} + (D_{AIP} - D_{throat}) \left[3 \left(1 - \frac{x}{L} \right)^4 - 4 \left(1 - \frac{x}{L} \right)^3 + 1 \right] \quad (34)$$

Table 6 RAE-M2129 geometric parameters

Quantity	Value	Description
D_{throat}	0.1288 m	Throat diameter
D_c	0.1440 m	Highlight (entry) diameter, capture area
D_{AIP}	0.1524 m	Diameter at AIP
x_{AIP}	0.4839 m	AIP position
L	0.4572 m	Duct length

The inlet contains circular cross-sections throughout. It was necessary to approximate certain aspects of the RAE-M2129 inlet to reproduce the geometry shown in Fig. 44. The geometry used in the following mesh validation study contains four key sections – inlet lip, upstream parallel extension, s-duct, and downstream parallel extension.

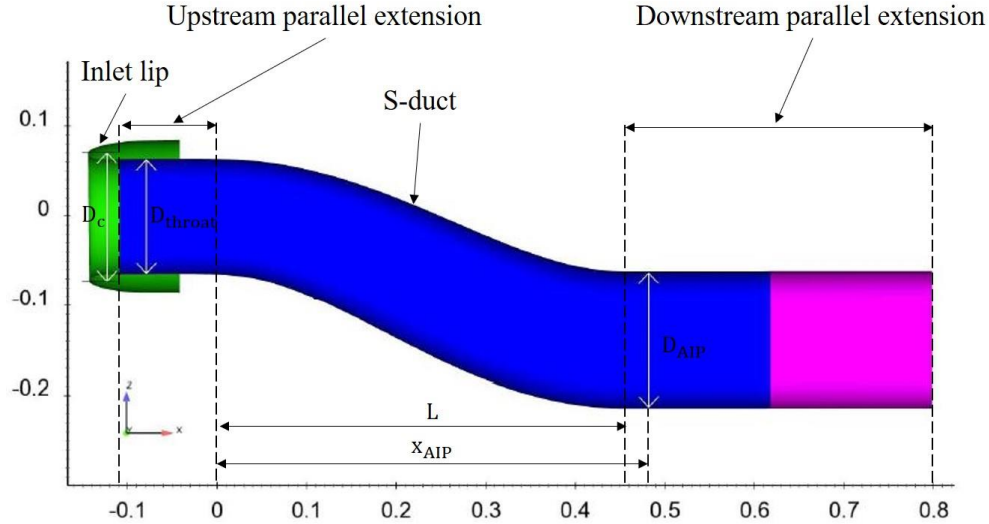


Figure 44 Main sections of RAE-M2129 geometry [38, with additional annotations]

The inlet lip geometry was not provided and was therefore approximated using points on a cropped image of Fig. 44. New axes and axes tick values were placed on the cropped image along with approximated coordinates of the lip leading edge point and the point of intersection between the lip and the upstream parallel extension. A finer axis resolution was interpolated and extrapolated to locate all points within the image. Points were placed manually on the screenshot to trace the curvature of the lip, then used as inputs within the SOLIDWORKS spline tool. Pixilation in the screenshot is a limiting factor and likely source of error in this approximation. The values of the spline are tabulated below in Fig. 45.

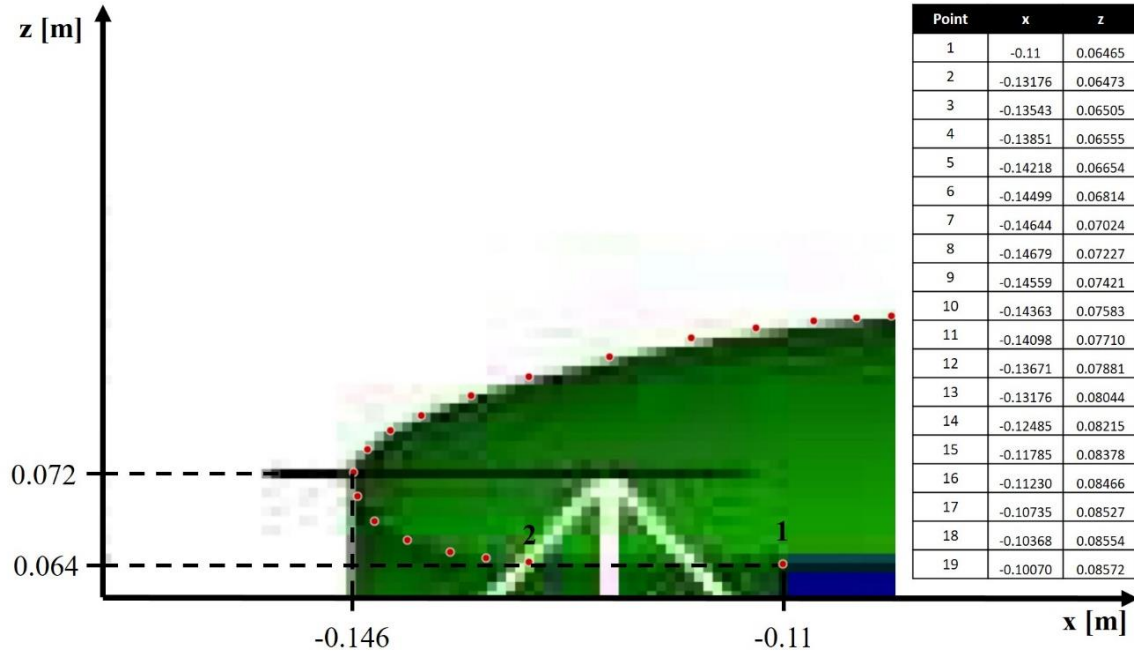


Figure 45 RAE-M2129 lip geometry approximation

The upstream parallel extension is a constant-area section that matches the entrance area of the s-duct ($x = 0$). The length of the upstream parallel extension was approximated as 0.11 m.

Equations 33 and 34 were discretized along 17 equally spaced lofting planes to reproduce the s-duct geometry in terms of the duct curvature and cross-sectional diameter. The discretized set of centerline points were connected using SOLIDWORKS B-spline tool. Error between the spline and Eqn. 33 was not evaluated. The cross-sectional diameter was defined at each lofting plane. All internal cross-sectional shapes were defined by the SOLIDWORKS Boss/Base Loft tool. Error between the internal cross-sectional shapes and Eqn. 34 was not evaluated. Figure 46 below illustrates the

positions of the lofting planes along the discretized centerline. The maximum Mach number location is emphasized for later reference in the discussion of the mesh validation results. The relative magnitude of the s-duct centerline curvature demonstrates the symmetry between the upstream and downstream halves of the s-duct, as well as the smooth transition of the spline between lofting planes.

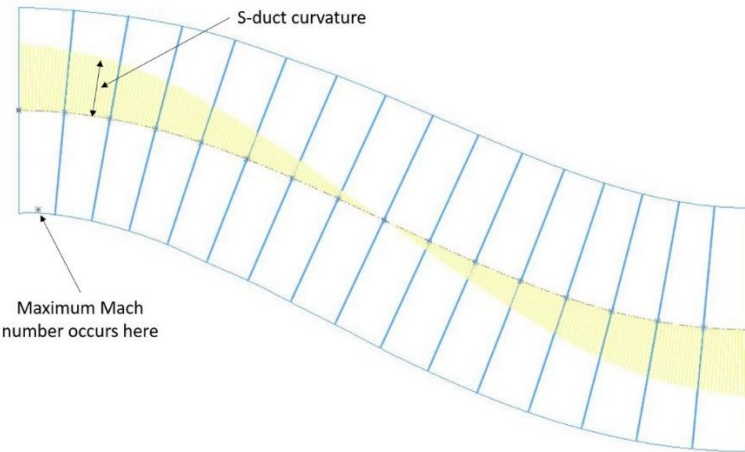


Figure 46 Side view of RAE-M2129 lofting planes

The downstream parallel extension is a constant-area section, approximately 0.3428 m in length, that matches the exit area of the s-duct ($x = 0.4572$). The AIP is located slightly downstream of the exit of the s-duct within the downstream parallel extension. The downstream parallel extension's main function is to assist with numerical

convergence in the CFD simulations. A coarse mesh is applied in this region to dissipate flow structures between the AIP and the exit of the downstream parallel extension.

The solution domain included a half-spherical region to represent the freestream conditions. A diameter equivalent to $20D_c$ was used for the freestream domain. Figure 47 highlights important boundary conditions in the simulation. All boundaries not explicitly labeled in Fig. 47 were set as no-slip walls.

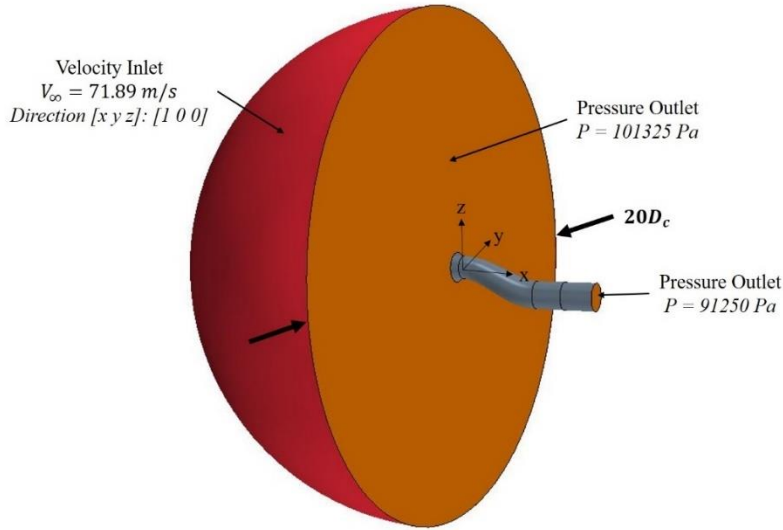


Figure 47 RAE-M2129 simulation domain

Approximately 6 million cells were used in the unstructured mesh. STAR-CCM+'s “Trimmer” meshing model was used throughout the domain. Isotropic refinement regions were applied throughout the inlet with a cell size of 0.002 m. An upstream conical refinement near the lip was used to capture the contraction of the

freestream flow into the inlet. A slow volumetric growth rate was applied to the mesh to gradually increase the cell size in the freestream domain and the downstream parallel extension. A total of 40 prism layers distributed over a total thickness of 0.01 m were used to resolve the boundary layer along the inlet lip, upstream parallel extension, s-duct, and downstream parallel extension (not including the coarse mesh region). The near wall prism layer thickness was iterated until wall y^+ values were mostly below unity to avoid use of wall functions. Figures 48 and 49 show the relevant size parameters of the mesh, and wall y^+ distribution, respectively.

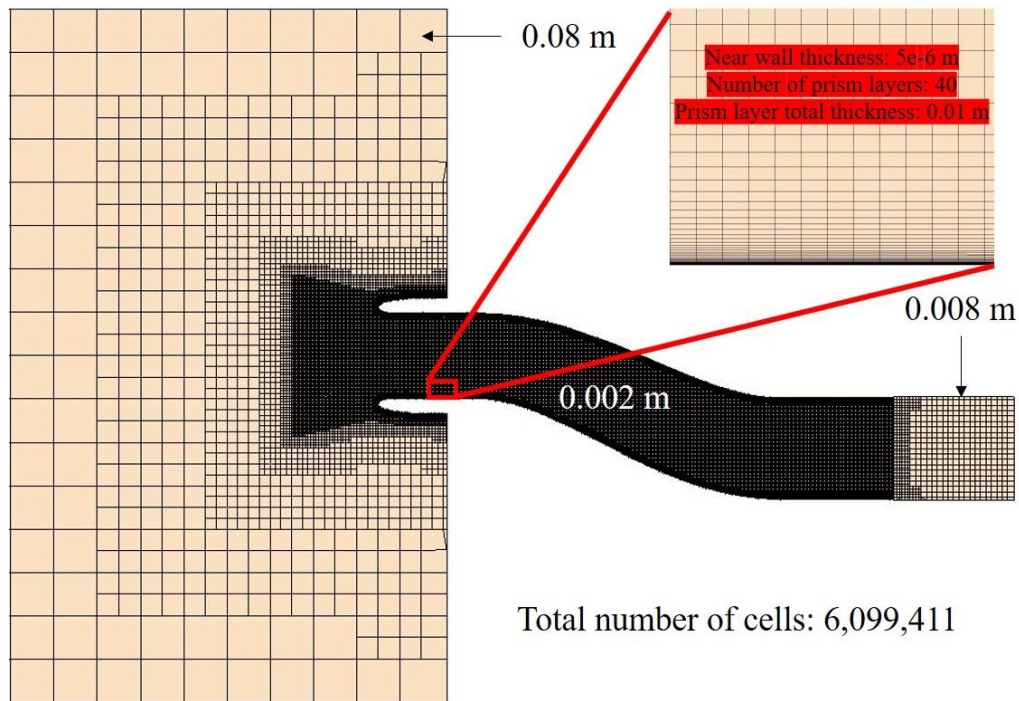


Figure 48 RAE-M2129 unstructured mesh

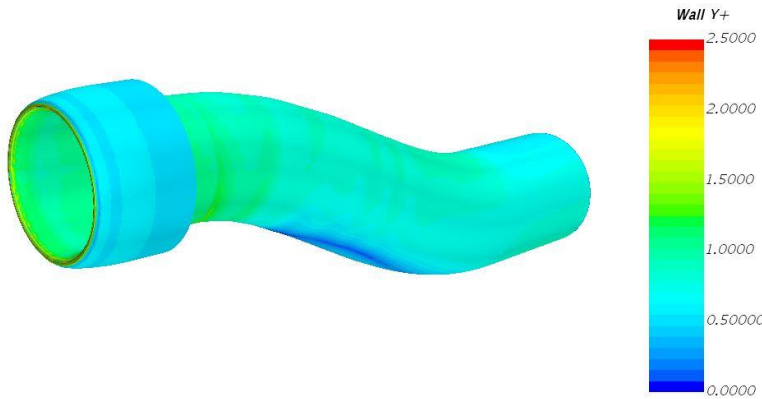


Figure 49 RAE-M2129 wall y^+

4.4 RAE-M2129 Mesh Validation Results

A velocity inlet and two pressure outlet boundary conditions were used to drive the flow in the mesh validation case. The curved surface of the freestream domain was set as the velocity inlet with a constant velocity magnitude of 71.89 m/s at zero incidence angle. The flat surface of the freestream domain was set as a pressure outlet boundary condition with a constant ambient pressure of 101325 Pa. Flow through the inlet was driven by the pressure outlet boundary condition set to the exit surface of the downstream parallel extension.

One of the goals of the mesh validation case was to match QinetiQ's experimental mass flow rate of 2.873 kg/s. A target mass flow condition was set to the pressure outlet at the exit of the downstream parallel extension. STAR-CCM+ uses the difference between the target mass flow condition and the mass flow at the current iteration to

determine an appropriate change in back pressure. Automatic back pressure adjustments were made after every 10 iterations.

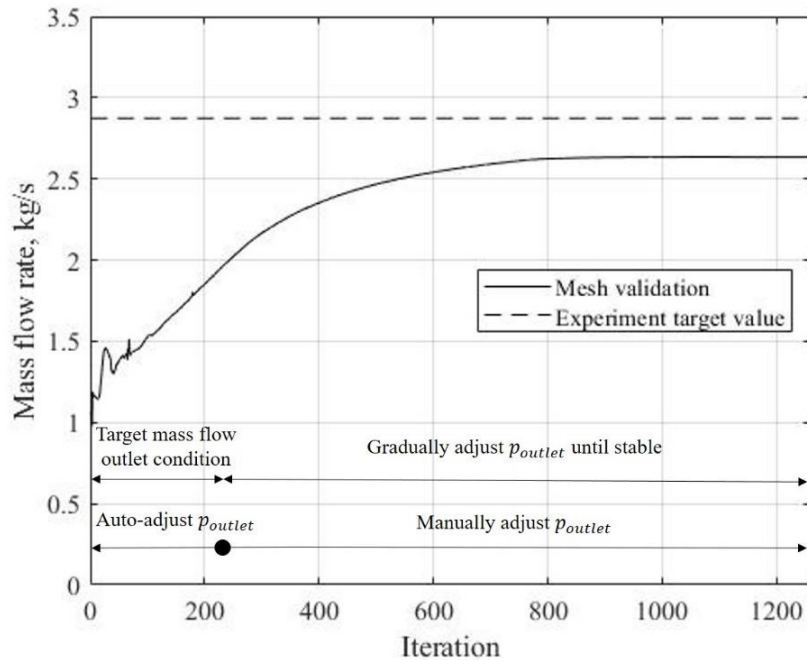


Figure 50 RANS mesh validation solution obtained through outlet pressure adjustments

The simulation process required both automatic and manual adjustments to the back pressure to provide a steady mass flow rate, as shown in Fig. 50. It was found that the change in mass flow rate was much slower than the change in back pressure, possibly due to the small number of iterations between automatic pressure adjustments. The mass flow rate was therefore monitored carefully throughout the solution process. The target mass flow condition at the pressure outlet was disabled when the mass flow rate reached

approximately 2 kg/s, then further adjustments to the back pressure were made manually to allow the solution to reach a stable condition.

Table 7 below summarizes the mesh validation results in comparison to QinetiQ experimental data and Onera CFD results. Considerable effort was made to match the experimental mass flow rate, however problems of high Mach number flow around the first turn of the s-duct prevented any further drop in back pressure. This limitation resulted in a maximum mass flow rate that was approximately 8% lower than the experimental value.

A notable difference between the experimental data and the mesh validation case is a 5% under-prediction of the mass flow ratio (A_0/A_c). Despite this difference, the pressure recovery measured at the AIP matches the experimental data within 0.65%.

Table 7 Summary of RAE-M2129 mesh validation results

	Experiment	RANS [38]	RANS Mesh Validation
Turbulence Model	-	k- ω Kok	k- ω SST
Outlet pressure [Pa]	-	89050	91250
Δ Outlet pressure	-	-	+2.47%
Mass flow [kg/s]	2.873	2.866	2.634
Δ Mass flow/Mass flow	-	-0.22%	-8.32%
A_0/A_c	2.043	2.074	1.942
$\Delta(A_0/A_c) / (A_0/A_c)$	-	+1.53%	-4.94%
Mach at AIP	0.3950	0.4234	0.3972
$\Delta(M_{AIP}) / (M_{AIP})$	-	+7.2%	+0.56%
PRA	0.8701	0.8613	0.8683
$\Delta PRA / PRA$	-	-1.0%	-0.2%
η_{02}	0.9798	0.9806	0.9734
$\Delta\eta_{02}/\eta_{02}$		+0.1%	-0.65%

Figure 51 below compares the Mach number contour for the mesh validation case against previous CFD work by Onera, at a plane located along the centerline of the inlet (normal vector in the y-direction). The mesh validation case demonstrates close agreement in terms of Mach number and streamlines in nearly all areas of the inlet in Fig. 51.

Small deviations occur slightly downstream of the inlet lip, where the mesh validation case shows a slightly larger Mach number. This is an interesting result considering the mass flow rate of the mesh validation case was 8% lower than Onera. It is possible that lip shape estimation error of the mesh validation case contributed to these deviations.

In general, the streamlines in both simulations appear to show the same flow physics. The stagnation point on the lip is nearly identical. The flow contracts from the freestream and accelerates into the upstream parallel extension. The flow reaches a maximum velocity magnitude slightly upstream of the inside corner of the first turn, which follows theoretical and experimental expectations. The separation bubble is predicted within the separated flow downstream of the first turn. There is a locus of points in both simulations near the outside corner of the second turn that result in dramatically different streamline directions due to the separation bubble. A second separation region can be seen on the inside corner of the second turn, however it has a small effect on the flow at the AIP in comparison to the first turn flow separation. The streamlines near the inside corner of the second turn appear to deflect to match the angle of the second turn separation region. This downward deflection of streamlines is opposed

near the centerline of the inlet at AIP, where the separation region propagated from the first turn turns nearby streamlines nearly horizontal.

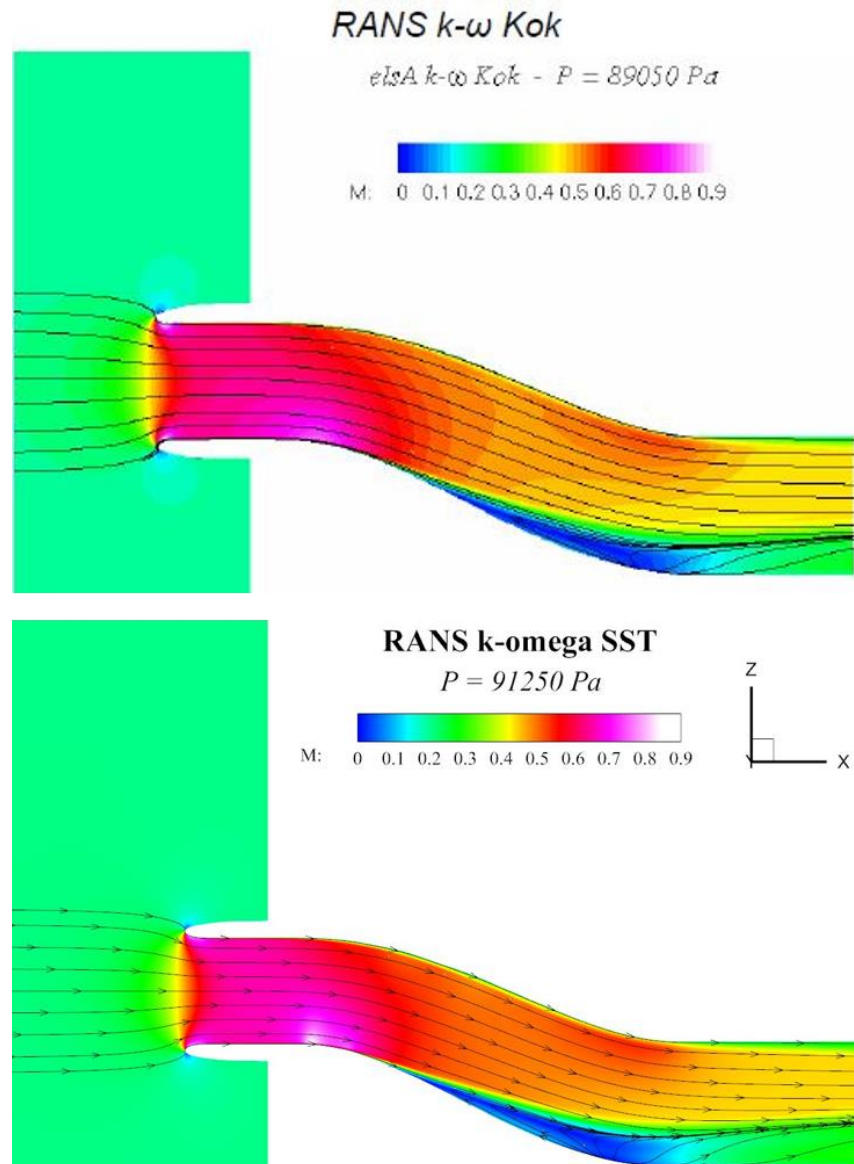


Figure 51 Mach contour comparison between Onera RANS results (top) and mesh validation RANS results (bottom)

Static pressure was measured along the starboard (lower) and port (upper) surfaces and compared against GARTEUR CFD results in Fig. 52. A difference of approximately 11% can be seen at the maximum pressure drop corresponding to the flow acceleration around internal side of inlet lip. The bifurcation of the static pressure between the starboard and port surfaces corresponds to the increased acceleration of the flow along the starboard surface as it approaches the first turn. In GARTEUR CFD results, this bifurcation occurs at approximately $x = -0.1\text{ m}$, while the mesh validation case shows this behavior slightly more downstream at approximately $x = -0.07\text{ m}$.

Figure 52 shows that interesting results occur within the s-duct section of the inlet for the mesh validation case, compared with GARTEUR CFD. Overall, the static pressure trends agree closely in magnitude, however the mesh validation case demonstrates unexpected oscillations along both surfaces. The oscillations were concluded as errors in the mesh validation results because of the steady-state nature of the simulations and further comparisons to experimental data for similar s-duct geometry. Given that the simulated pressure information was obtained from cells near the inlet walls, additional simulations were run with varying near-wall cell thicknesses to attempt to smooth the curves in Fig. 52. No change was observed in these additional simulations. Computational constraints prevented further investigation into the source of these errors. It is possible that the error associated with the lofting methodology described earlier contributed to the oscillations in the starboard and port pressure distributions.

An additional result of Fig. 52 is that the mesh validation case shows an approximately equal static pressure value between the high-speed flow near the lip and

the inside corner of the first turn. GARTEUR results show a relative pressure difference of approximately 20% between these same inlet positions.

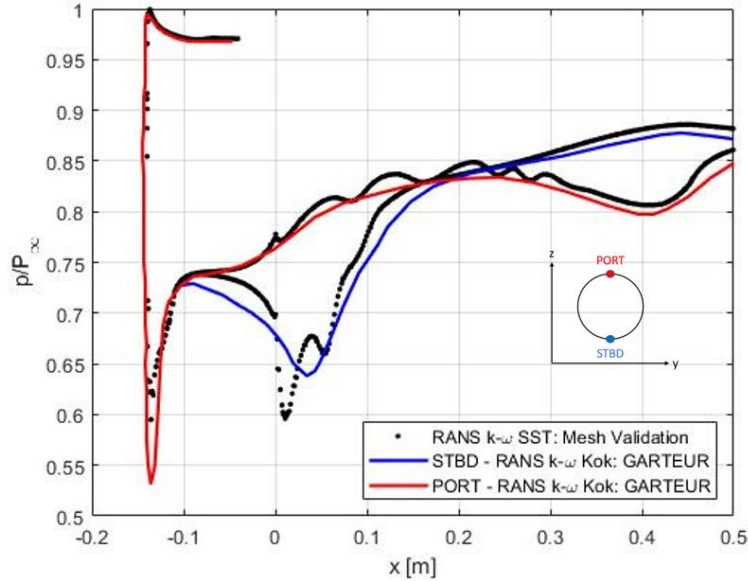


Figure 52 Static pressure along duct walls - starboard and port

The pressure recovery performance parameter was deemed as the most important result in the mesh validation case due to interest in the flow behavior at the AIP. Figure 53 emphasizes the close agreement (-0.65% compared with experimental data) in η_{02} described in Table 7. The CFD results in the mesh validation case and GARTEUR both overpredict the pressure loss at the AIP near the center of the separation region propagated from the inside corner of the first turn. This overprediction of pressure loss is offset by the tight localization of the separation region in the lower section of the AIP in

comparison to the distribution of the separation region in experimental data. Figure 53 also confirms that the separated flow from the inside corner of the second turn has very little effect on the AIP total pressure distribution.

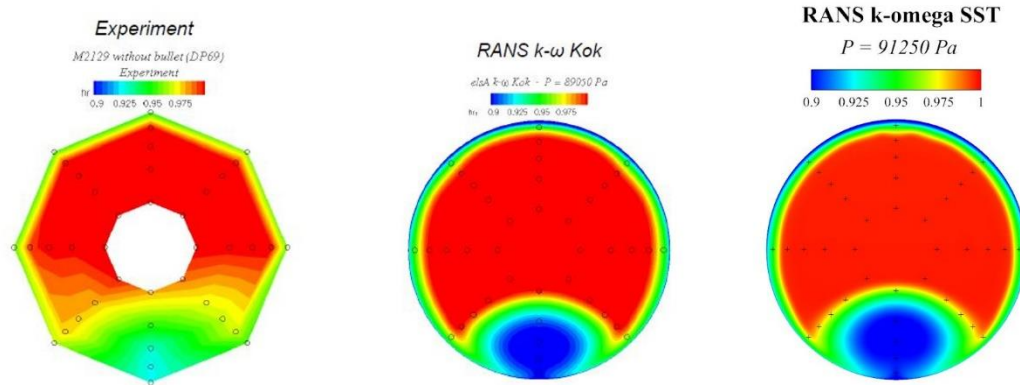


Figure 53 AIP pressure recovery

A result that does not have a GARTEUR comparison but may be useful for future steady-state RANS analyses of similar s-duct geometry, is the progression of pressure recovery downstream of the first turn separation region. Figure 54 shows that the width of the separation region remains relatively constant throughout the second half of the inlet. The separation bubble shows dominant effects in planes 1 and 2. Total pressure recovers near the outside corner of the second turn. Pressure recovery also increases slightly in the interior flow between plane 3 and the AIP.

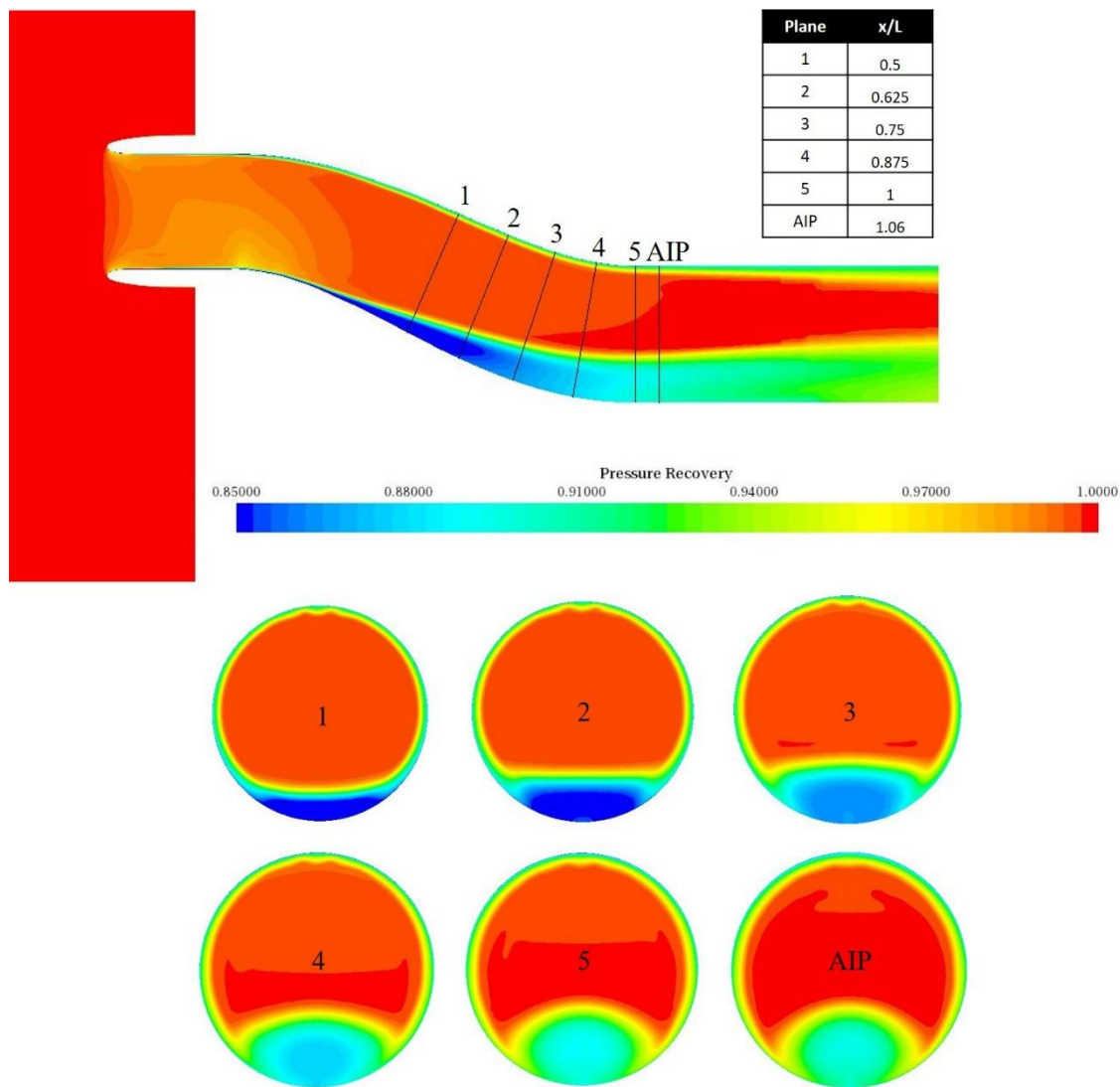


Figure 54 Pressure recovery through downstream half of RAE-M2129 s-duct

In summary, the mesh validation case demonstrated adequate mesh practices for RANS simulation of an s-duct diffuser geometry. The main flow behavior was found to match closely with both QinetiQ experimental data and Onera CFD results. A separation bubble downstream of the first turn was predicted in both the mesh validation case and

CFD results by Onera. Slight differences in mass flow rate and wall static pressure were outweighed mainly by close agreement in the prediction of pressure recovery at the AIP.

4.4 XQ-1A-2 Inlet Design

The focus of this section is a discussion of the XQ-1A-2 inlet design, which is an improvement upon the preliminary XQ-1A-1 inlet. For simplicity, the XQ-1A-2 inlet is referred to as the XQ-1A inlet in the remainder of this discussion. Important aspects of the original design, such as inlet offset and length, were maintained in the updated iteration based on the previously established position of the engine and inlet entrance face. There are two main goals in this section: (1) reduce the number of parameters that fully define the inlet geometry and (2) use CFD to analyze the performance of the updated iteration. It was important to reduce the number of geometric parameters in the design because it provides an efficient foundation for future inlet design trade studies. It was also important to analyze the performance of the updated design iteration through a comparison with the RAE-M2129 mesh validation results. The comparison against the RAE-M2129 inlet required geometric scaling of the XQ-1A inlet. The performance of the XQ-1A inlet was also analyzed at an angle of attack condition of 21° , corresponding to the predicted maximum rate of climb.

As previously discussed, the XQ-1A-1 design relied on vertical offset from a linear reference line between the center of the entrance face of the inlet and the center of the exit face of the inlet. The main problem with this method of definition of the

centerline curvature was that it did not provide a smooth surface transition between the exit of the s-duct and the entrance of the downstream parallel extension.

The XQ-1A inlet design attempts to solve this problem through a centerline curvature definition that relies on the intersection between two circular arcs, as shown by Fig. 55.

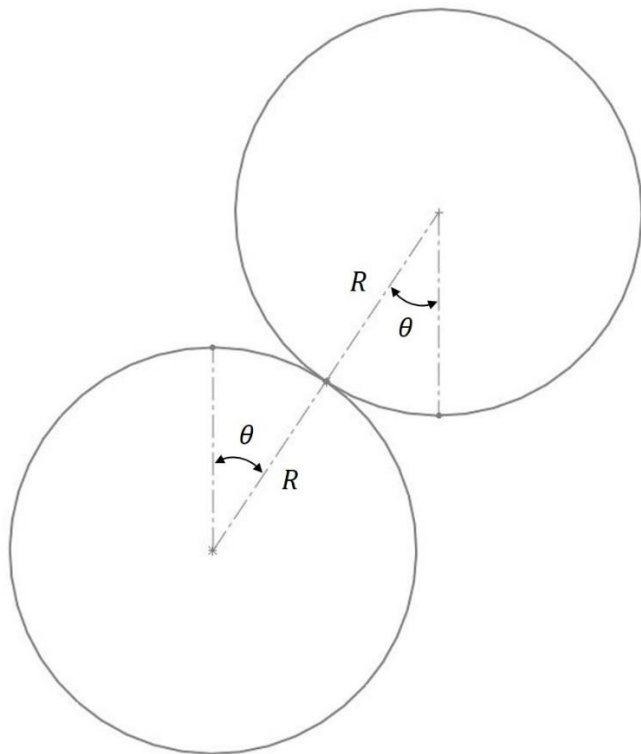


Figure 55 Updated design iteration defined by the intersection of two circular arcs

In this configuration, the circles are of identical size therefore the radius of curvature is constant through the s-duct. The location of the centerline center of curvature changes at the intersection point of the circular arcs. The benefit of this geometric parameterization is that the desired inlet length and offset can be easily converted to an s-duct centerline by Eqn. 35 and Eqn. 36. These centerline relationships are further illustrated in Fig. 56.

$$L = 2R\sin\theta \quad (35)$$

$$H = 2R[1 - \cos\theta] \quad (36)$$

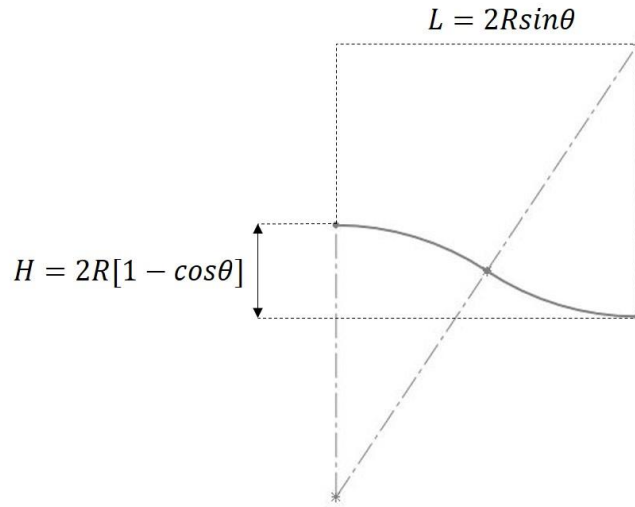


Figure 56 Definition of s-duct centerline curvature

There are a range of combinations of circle radius and arc angle that satisfy each individual constraint of inlet length and offset, however only one combination of R and θ exists such that both constraints are met.

Lofting planes were defined following a similar discretization process performed for the RAE-M2129 geometry. As shown below in Fig. 57, a total of 17 lofting planes were used, which were equally spaced by eight divisions of the arc angle. The updated design maintained elliptical-to-circular cross-sections from the entrance face of the inlet to the exit.

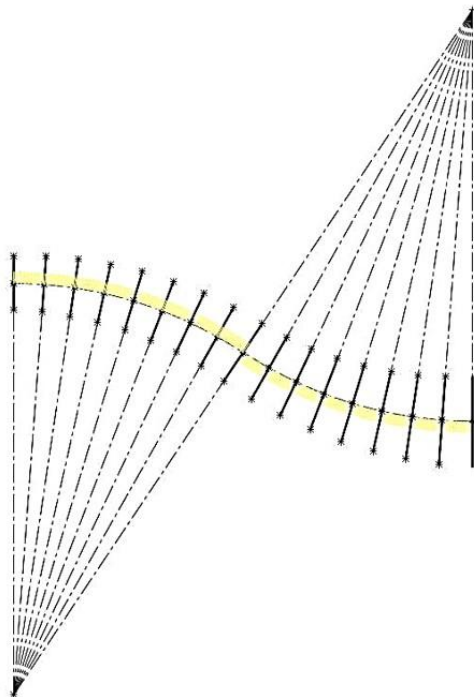


Figure 57 Side view of discretized centerline with constant radius of curvature (highlighted in yellow)

4.4.1 Geometry Scaling

Geometry scaling of the updated design iteration was required to compare performance against the RAE-M2129 inlet. This section highlights the similarities and differences between the scaled XQ-1A inlet design and RAE-M2129 to better understand the performance comparison. The scaled XQ-1A inlet geometry is illustrated below in Fig. 58.

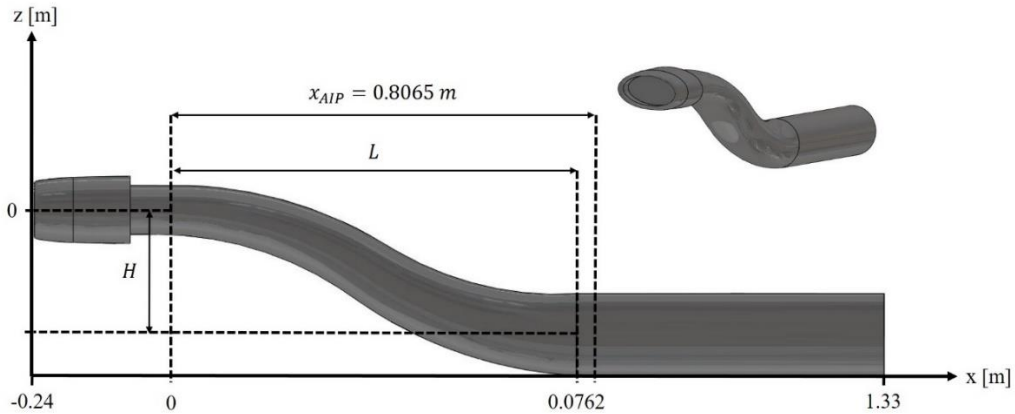


Figure 58 XQ-1A inlet design

The XQ-1A inlet design was scaled-up in size to match the RAE-M2129 cross-sectional area at the AIP ($D_{AIP} = 0.1524 \text{ m}$) and entrance face of the inlet ($A_{inlet} = 0.013 \text{ m}^2$). The AIP and entrance areas were chosen to better understand the flow differences between the two geometries within the s-duct section. These differences

inherent to the XQ-1A design included the elliptical-to-circular cross-section profile, constant radius of curvature, linear change in cross-sectional area, and larger inlet length and offset. The XQ-1A inlet design lofts to a circular cross-section at the AIP, therefore a direct comparison can be made of the pressure recovery profile. Freestream conditions were matched, and the target mass flow rate was set to match the mesh validation case of 2.634 kg/s.

The scaled XQ-1A inlet design uses a centerline with a constant radius of curvature, $R = 0.6868\text{ m}$, and a flow turning angle, $\theta = 33.69^\circ$, to maintain the relative dimensions of the inlet length ($L = 5D_{AIP}$) and offset ($H = 1.514D_{AIP}$). Table 8 below compares the inlet length, offset, and area ratio between the two inlet geometries. Scaling also introduced differences in the centerline profile, as shown below by Fig. 59, that are important to better understand the performance comparison with the RAE-M2129 inlet.

Table 8 Inlet geometry comparison

	RAE-M2129	XQ-1A
L/D_{AIP}	3	5
H/L	0.30	0.30
A_{AIP}/A_{throat}	1.40	1.40

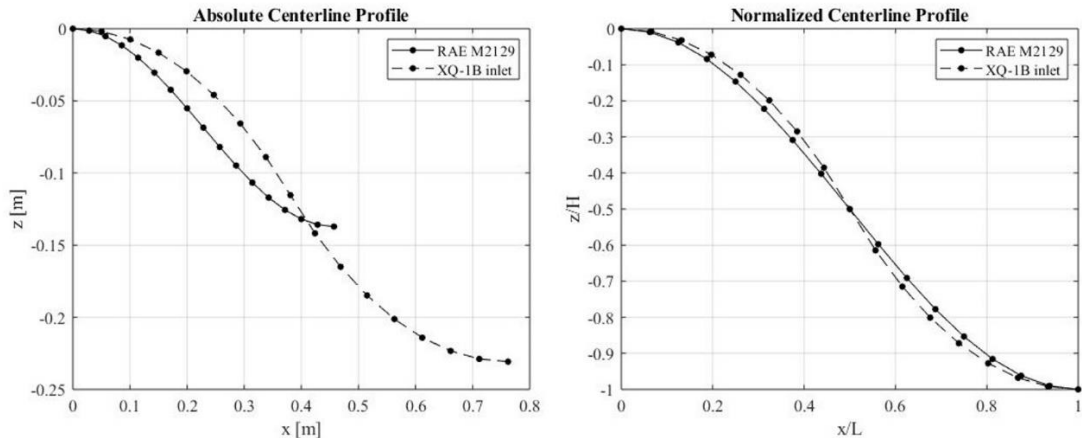


Figure 59 Comparison of absolute and normalized centerline profiles of XQ-1A inlet and RAE-M2129

The scaled XQ-1A inlet has an absolute length that is 66% longer, and an offset that is 68% taller, than the RAE-M2129. The normalized centerline profiles demonstrate a very similar shape despite the differences in radius of curvature. The RAE-M2129 inlet has relatively large curvature radii near the entrance face and exit, which gradually reduces to zero centerline curvature near the center of the inlet. The XQ-1A inlet maintains a constant radius of curvature throughout.

Figure 60 compares the cross-sectional area distribution between each inlet geometry. The XQ-1A design uses a linear increase in cross-sectional area between the inlet entrance face to the AIP. The RAE-M2129 inlet increases area mainly between the first and second turn of the inlet where the radius of curvature of the inlet centerline is relatively small. There is an asymmetry in the area distribution about the midpoint of the

RAE-M2129 inlet such that a gradual increase in cross-sectional area is used upstream of the first turn and downstream of the second turn to the AIP.

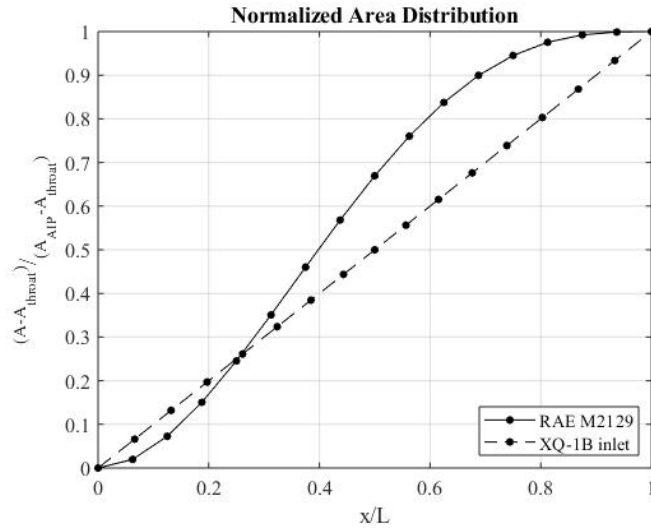


Figure 60 Comparison of normalized area distribution between XQ-1A inlet and RAE-M2129

The XQ-1A inlet design linearly decreases the ratio between the semi-major and semi-minor axes of the elliptical cross-sections to form a circular cross-section at the AIP. The semi-major axis is chosen as twice the length of the semi-minor axis at the entrance face of the inlet. The variation of the elliptical cross-section dimensions is illustrated below in Fig. 61.

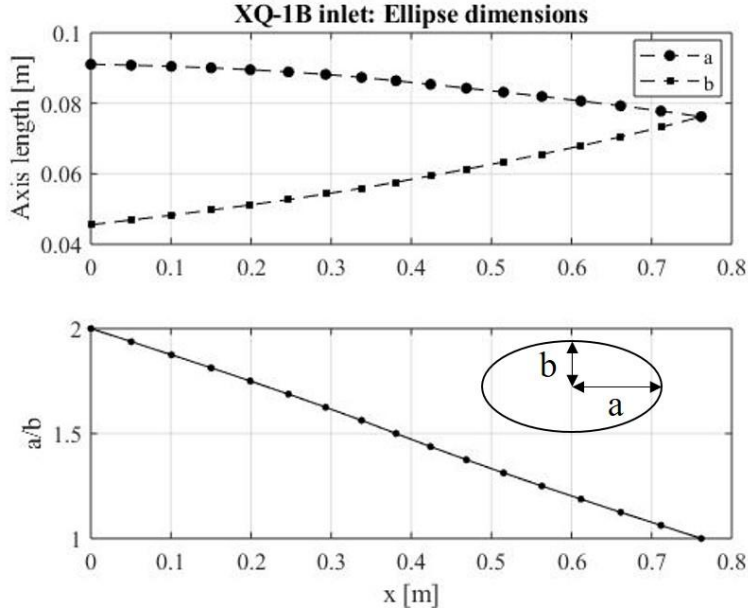


Figure 61 Cross-sectional ellipse dimensions of XQ-1A inlet

4.4.2 CFD Results and Discussion

Boundary conditions used in the mesh validation case were identically applied to the XQ-1A geometry. Two cases are considered in this section that attempt to characterize the XQ-1A inlet performance at a level flight condition ($0^\circ AOA$) and a pitch-up maneuver corresponding to the predicted maximum rate of climb ($21^\circ AOA$). Table 9 below compares the CFD results between the mesh validation case, and the XQ-1A inlet at each flight condition. The target mass flow rate was set to match the mesh validation case of 2.634 kg/s . Based on the increased length and offset of the XQ-1A geometry, a lower outlet pressure was required to meet the target mass flow. The maximum rate of climb case was not able to reach the target mass flow condition due to

numerical convergence issues associated with high Mach number flow around the separation region at the inlet lip. A 28% increase in captured freestream streamtube area was observed for the XQ-1A. The XQ-1A inlet CFD results show a 1.12% lower pressure recovery at the AIP compared with the RAE-M2129 inlet.

Table 9 CFD results for XQ-1A inlet design compared against RAE-M2129 mesh validation case

	RANS Mesh Validation	RANS XQ-1A (0° AOA)	RANS XQ-1A (21° AOA)
Turbulence Model	k- ω SST	k- ω SST	k- ω SST
Outlet pressure [Pa]	91250	89225	86325
Δ Outlet pressure	-	-2.22%	-5.40%
Mass flow [kg/s]	2.634	2.634	2.520
Δ Mass flow/Mass flow	-	0%	-4.33%
A_0/A_c	1.942	2.487	-
$\Delta(A_0/A_c) / (A_0/A_c)$	-	+28.06%	-
Mach at AIP	0.3972	0.4021	0.3977
$\Delta(M_{AIP}) / (M_{AIP})$	-	+1.23%	-0.13%
PRA	0.8683	0.8572	0.8424
$\Delta PRA / PRA$	-	-1.28%	-2.98%
η_{02}	0.9734	0.9625	0.9446
$\Delta\eta_{02}/\eta_{02}$	-	-1.12%	-2.96%

Figure 62 below shows the Mach number contour for the XQ-1A geometry at the steady-level flight condition and the maximum rate of climb condition. The Mach number contour illustrates very similar flow behavior as the RAE-M2129. The flow accelerates through the upstream parallel extension and reaches a maximum speed near

the first turn, however the Mach number contour is more evenly distributed at the first turn compared to the RAE-M2129.

The flow begins to separate downstream of the inside corner of the first turn. Unlike the RAE-M2129 inlet, a separation bubble was not observed for the XQ-1A geometry. As a result, the percentage area of stagnant flow in this separated flow region is lower relative to the RAE-M2129. A larger region of separated flow is observed for the XQ-1A from the inside corner of the second turn.

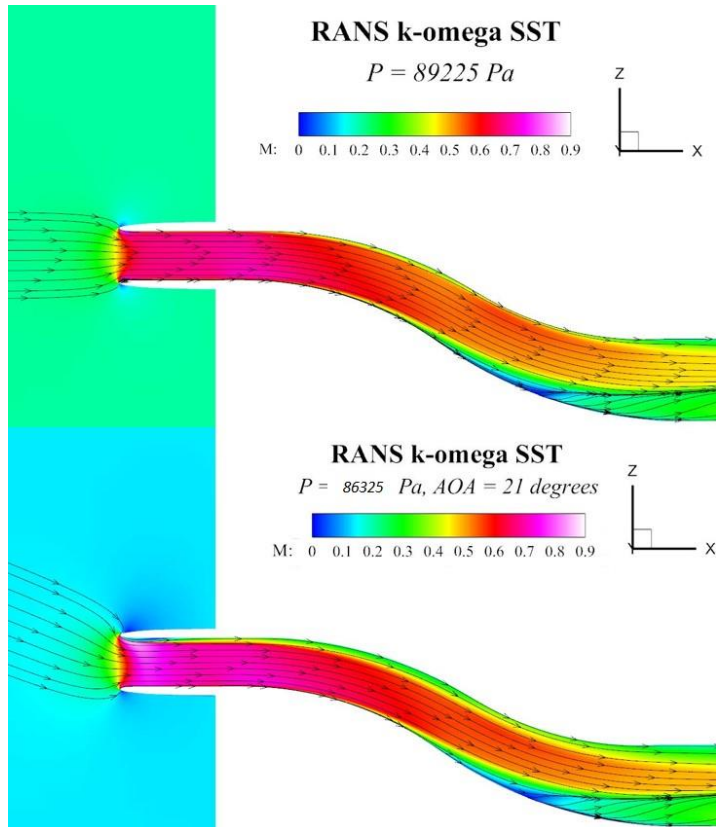


Figure 62 XQ-1A Mach number contour with streamlines for 0° AOA (top) and 21° AOA (bottom)

Figure 63 below shows that the XQ-1A and RAE-M2129 geometry each result in a similar concentrated low-pressure region at the lower half of the AIP. The low-pressure region for the XQ-1A geometry at $0^\circ AOA$ is nearly the same size as that of the RAE-M2129 geometry, just shifted slightly away from the lower wall boundary. There is also a noticeably larger low-pressure region near the upper half of the AIP for the XQ-1A inlet due to flow separation near the inside corner of the second turn. This result suggests that the lower surface-averaged AIP pressure recovery result (-1.12%) for the XQ-1A geometry may be primarily due to larger curvature of the XQ-1A inlet near the second turn. The angle of attack case for the XQ-1A inlet demonstrates the relative size increase of the low-pressure regions, particularly within the upper half of the AIP. The larger region of low pressure in the upper half of the AIP is due to the downstream propagation of flow separation that occurs at the inlet lip (shown in Appendix).

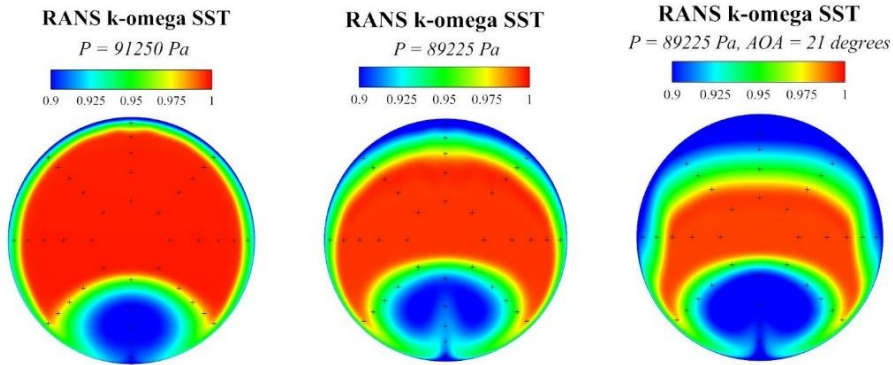


Figure 63 AIP pressure recovery comparison between RAE-M2129 (left) and XQ-1A inlet at $AOA = 0^\circ$ (middle) and XQ-1A inlet at $AOA = 21^\circ$ (right).

The shape of the low-pressure region at the lower half of the AIP suggests the presence of Dean vortices in the steady-state simulations, which is confirmed by a rear-visualization of streamlines through each inlet in Fig. 64. A total of sixteen streamlines were tracked from the freestream conditions to the exit of each inlet. The overall size of the vortex-pair is relatively similar between all three inlet geometries, however the vortices associated with the XQ-1A inlet appear to cause a greater contraction of the lower-half streamlines prior to the vortex-pair formation near the AIP. Possible reasons for the difference in streamline shape include differences of centerline curvature, cross-sectional shape, inlet length, and inlet offset.

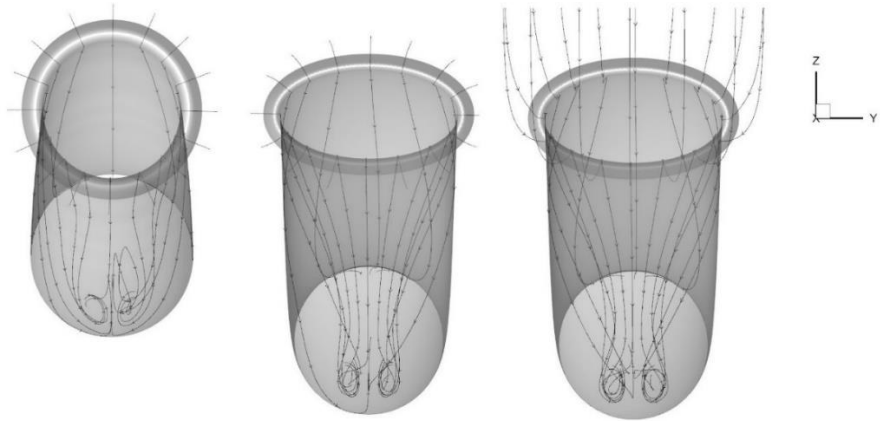


Figure 64 Rear-visualization of dean vortices located near the outside corner of the second turn, left to right: RAE-M2129, XQ-1A ($0^\circ AOA$), XQ-1A ($21^\circ AOA$)

The observed Dean vortices originate from flow separation near the inside corner of the first turn for all three inlet geometries. Figures 65 and 66 below demonstrate the

progression of the Dean vortex-pair formation downstream of the first turn. Compared against the RAE-M2129 results in Fig. 54, vortex formation appears to begin earlier for the XQ-1A geometry, as shown by the pressure recovery profile at the second cross-sectional plane location of $x/L = 0.625$. The overall size of the low-pressure region increases throughout the downstream cross-sections to the AIP, which is a similar trend observed for the RAE-M2129 results. The magnitude of the maximum total pressure loss begins to decrease downstream of the third-plane location of $x/L = 0.75$ for the XQ-1A inlet. For comparison, CFD results for the RAE-M2129 inlet show this decrease in maximum total pressure loss near the second-plane location of $x/L = 0.625$.

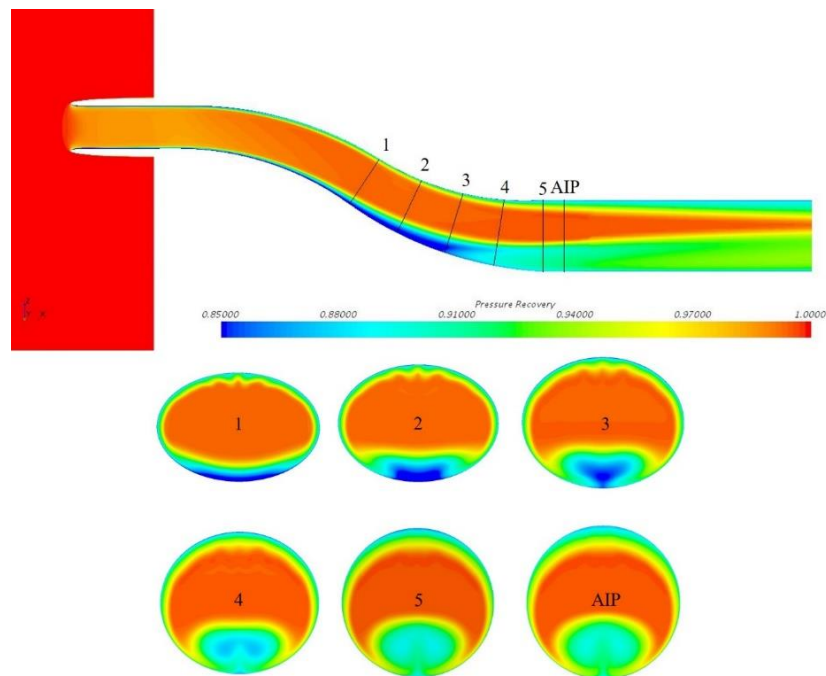


Figure 65 Pressure recovery through downstream half of XQ-1A inlet ($0^\circ AOA$)

Figure 66 shows the propagation of total pressure loss from flow separation near the lip of the XQ-1A inlet due to the 21° angle of attack condition. The overall width of the loss region increases downstream to the AIP. An interesting result is that the width of the maximum pressure loss region within the overall lip separation loss region decreases near the inside corner of the second turn. Larger width loss regions can be seen near the outer edges of the cross-sections in Fig. 66 due to the freestream incidence angle.

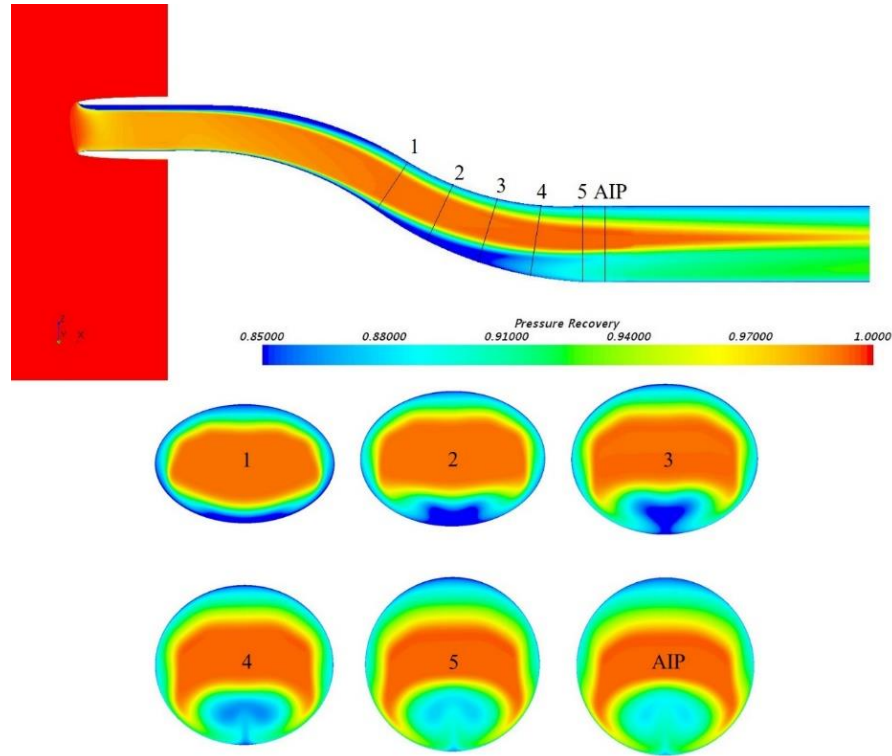


Figure 66 Plane progression of pressure recovery within XQ-1A inlet (21° AOA)

Total pressure distortion at the AIP was quantified for each inlet geometry in terms of circumferential and radial distortion. Circumferential distortion was determined based on circumferential distortion intensity, extent, and multiple-per-revolution elements. Radial distortion was determined based on a radial distortion intensity element.

Table 10 below summarizes circumferential and radial total pressure distortion elements for each ring of pressure probes in each inlet geometry. The pressure probe locations at the AIP are identical for each geometry.

The circumferential distortion intensity trend for the RAE-M2129 geometry is that the greatest intensity occurs within rings 2-4. The XQ-1A demonstrates larger intensity elements in rings 1-3. The intensities for rings 2 and 3 are similar in each geometry. The XQ-1A inlet at 0° AOA and 21° AOA demonstrates a circumferential distortion intensity improvement at ring 4 of 38% and 49%, respectively, compared with the RAE-M2129 inlet. Another difference in circumferential distortion intensity between the RAE-M2129 inlet and the XQ-1A inlet occurs at ring 1. In ring 1 at 0° AOA, the XQ-1A inlet resulted in a 129% greater circumferential distortion intensity than in ring 1 of the RAE-M2129 inlet. This result is explained qualitatively by the increase in overall size of the low-pressure region in the lower half of the AIP in Fig. 63, which is shown to cover pressure probes within ring 1.

Slight improvements in circumferential distortion intensity for the XQ-1A inlet are counteracted by large circumferential distortion extent angles. The extent of circumferential distortion ranges from a minimum of 56° at ring 5 to a maximum of 101° at ring 4 of the RAE-M2129 AIP. The extent angles for the XQ-1A inlet at 0° AOA vary

between 88° to 143° , with extent angles greater than 131° for four of the five rings.

Extent angles for the XQ-1A inlet at 21° AOA vary between 113° at ring 3 to 185° at ring

5. The maximum angle of 185° at ring 5 is associated with the large low-pressure region in the upper half of the AIP due to the propagation of flow separation at the inlet lip.

The MPR distortion element is an important parameter that provides information on the equivalent number of relative low-pressure regions at the AIP. The quantitative results of MPR for the RAE-M2129 inlet confirm that the propagation of flow separation from the inside corner of the first turn is the main contributor to distortion at the AIP for rings 1-4. An equivalent MPR of 1.40 was calculated at ring 5 due to the second turn flow separation effect at the AIP. In general, the XQ-1A inlet resulted in higher MPR distortion elements at more internal AIP rings due to the larger effect of flow separation from the inside corner of the second turn. This effect is also confirmed by the results of radial distortion, which suggest that the primary loss regions occur at outer rings of the AIP.

Table 10 Summary of AIP circumferential and radial total pressure distortion

	Ring	Circumferential Distortion			Radial Distortion Intensity
		Intensity	Extent	MPR	
RAE-M2129	1	0.014	78°	1	-0.018
	2	0.041	94°	1	-0.004
	3	0.040	98°	1	-0.004
	4	0.037	101°	1	-0.004
	5	0.024	56°	1.40	+0.030
XQ-1A (0° <i>AOA</i>)	1	0.032	131°	1	-0.013
	2	0.039	143°	1	-0.006
	3	0.034	139°	1	-0.007
	4	0.023	88°	1.58	+0.002
	5	0.026	139°	1.22	+0.025
XQ-1A (21° <i>AOA</i>)	1	0.037	130°	1	-0.030
	2	0.040	134°	1	-0.014
	3	0.032	113°	1.33	+0.000
	4	0.019	117°	1.34	+0.015
	5	0.024	185°	1.10	+0.029

The results within Table 10 were extracted from the results below in Fig. 67, which provide the circumferential distortion profiles for each ring at the AIP of each inlet geometry. All plots in Fig. 67 are shown on the same axis scale to compare the distortion profile at each ring. In general, the outer regions of each curve represent the total pressure near the upper half of the AIP and the middle region of each curve represents the total pressure near the lower half of the AIP. The dashed line that spans the full circumference of each plot represents the average ring total pressure. The dashed line that spans the shaded low-pressure regions represents the average total pressure within the shaded region. Plots with multiple shaded regions represent rings with MPR elements greater than unity. In all cases where multiple low-pressure regions were observed, the

surrounding high-pressure extent values were greater than the set threshold value of 25° used to calculate the appropriate intensity, extent, and MPR distortion elements.

Relatively very little pressure loss is observed in ring 1 at the AIP of the RAE-M2129 inlet. Ring 1 profiles for the XQ-1A inlet demonstrate the similar circumferential distortion intensity and extent elements shown in Table 10, however the overall profile for the 21° AOA case is shifted lower due to the lower freestream total pressure condition. As expected, this downward shift of the circumferential distortion profile is observed for all AIP rings. The propagation of the separation region from the inside corner of the second turn does not appear within ring 1 for any of the cases tested.

At ring 2, circumferential distortion intensity is similar in magnitude between all three cases. The extent elements for both XQ-1A cases are approximately 50% greater than the RAE-M2129 case at ring 2. Distortion effects can be seen for circumferential locations between 270° to 90° within ring 2 of the XQ-1A inlet at 21° AOA. The drop in pressure within this region demonstrates the large width of the loss region at the AIP associated with the upstream lip separation.

The distortion profiles at outer rings demonstrate the increasing effect of the loss region near the upper half of AIP that results in MPR distortion elements greater than unity, particularly for both XQ-1A cases. An additional general result is that the local high-pressure peaks relative to the associated ring average pressure are larger for the XQ-1A cases, demonstrating the larger circumferential variation in total pressure.

The low-pressure region within the lower half of the AIP is dominant for all rings within the RAE-M2129 case. In the XQ-1A cases at 0° AOA and 21° AOA,

circumferential pressure distortion is dominated by the low-pressure region within the lower half of the AIP for rings 1-4 and rings 1-3, respectively. The remaining rings are dominated by the low-pressure region within the upper half of the AIP for the XQ-1A inlet. A comparison of these results and the normalized inlet centerlines depicted in Fig. 59 suggests that the smaller radius of curvature near the second turn of the XQ-1A inlet may be the cause of the larger region of separated flow at the upper half of the AIP.

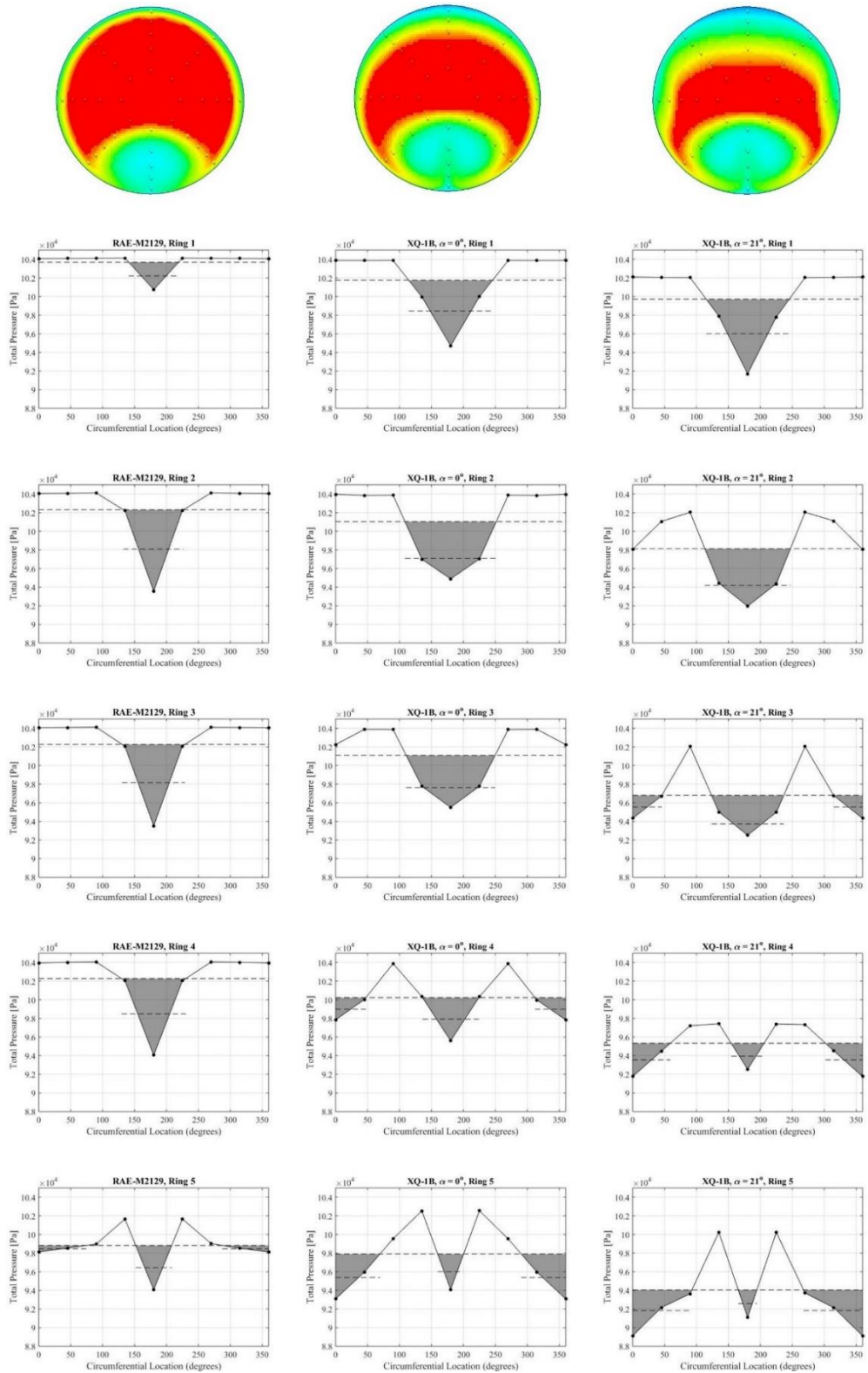


Figure 67 AIP circumferential total pressure distortion

CHAPTER 5. CONCLUSIONS AND FUTURE WORK

5.1 Conclusions

An s-duct inlet design was presented to fit a small-scale UAV developed in-house by The Flight Vehicle Design and Testing Group at The Ohio State University. Subsonic wind tunnel testing was performed for a 1/5th-scale model to obtain aerodynamic characteristics of the aircraft and determine an appropriate small-scale jet engine for the 1/3rd-scale flight-test demonstrator. Inlet length and offset dimensions were determined relative to the engine diameter of the JetCat P-20SX ($L/D_{AIP} = 5.0$ and $H/L = 0.3$) such that the inlet fit the existing fuselage of 1/3rd-scale model. The inlet geometry was parameterized using the intersection of two circular arcs of equal radii, which created an inlet centerline with a constant radius of curvature and a flow turning angle of approximately 33°.

A steady-state RANS CFD validation study was performed for the RAE-M2129 inlet to verify the mesh application to the XQ-1A inlet design. The mesh validation case successfully agreed with much of the experimental data and previous CFD results for the RAE-M2129 inlet, however at an 8% lower mass flow rate and 5% lower mass flow ratio. Difficulty in matching mass flow rate was observed due to the observance of high Mach number flow near the inside corner of the first turn. Details of the RAE-M2129 geometry replication process were discussed to possibly highlight areas of improvement. Agreement between CFD results and experimental data in terms of pressure recovery was

observed within 0.7%, which served as sufficient evidence to proceed due the importance of pressure recovery as an inlet performance parameter.

The design was then scaled up to match both the AIP diameter and inlet entrance diameter of the RAE-M2129 inlet to provide a comparison to evaluate the simulated performance of the XQ-1A inlet. The scaled XQ-1A inlet geometry was also similar to the RAE-M2129 inlet in terms of relative offset ($H/L = 0.3$), however the absolute length and offset of the XQ-1A inlet were larger than the RAE-M2129 inlet. The XQ-1A inlet also used elliptical-to-circular cross-sections while the RAE-M2129 inlet used circular cross-sections throughout. A detailed description of the similarities and differences between the inlet geometries was provided to better understand the performance comparison. The differences in geometry caused a 1.12% decrease in pressure recovery for the XQ-1A inlet according to steady-state RANS CFD results.

Circumferential and radial pressure distortion at the AIP was analyzed in detail for both inlet geometries due to the impact of pressure distortion on compressor surge margin. The results showed that the intensity element of circumferential distortion and radial distortion were similar in magnitude between the inlet geometries, however the XQ-1A inlet demonstrated larger circumferential extent elements that suggested decreased performance. The main contributor to decreased performance of the XQ-1A inlet appeared to be a larger region of separated flow at the upper half of the AIP, propagated downstream from the inside corner of the second turn. A comparison between the inlet centerlines suggest that the larger region of separated flow near the inside corner

of the second turn may be due to the smaller radius of curvature for the XQ-1A inlet at that location.

5.2 Future Work

Future work is required to interrogate and build upon the computational results presented in this thesis. The computational models used, although useful to gain a general understanding of the flow field for various geometries in a time-efficient manner, are a simplified representation of the actual flow physics. The scope of this work was also limited to the simulated performance of the XQ-1A inlet at two flight conditions – (1) steady-level flight and (2) a pitch-up condition at 21° angle of attack.

Possibly the most natural extension of this work is an updated XQ-1A inlet design iteration to reduce the effect of flow separation from the inside corner of the second turn. This may be achieved by lengthening the inlet to increase the radius of curvature of the inlet centerline in this area. It appears that this would be a suitable solution due to the observed dominant effect of flow separation shown by CFD results, despite the inherent increased frictional losses that would occur with an increased inlet length. An increased inlet length would also locate the inlet entrance face more upstream along the fuselage, which would reduce the required frontal area of the boundary layer diverter.

Future work must dedicate time to the inlet lip design to reduce the possibility of flow separation over the range of flight conditions. The inlet lip design should be designed such that it is scalable to higher flight speeds, which may require additional design integration of inlet slots or bleeds.

The XQ-1A inlet design in this thesis used true elliptical cross-sections to simplify the set of design variables but this may not be a suitable geometry in terms of the aerodynamic compatibility between the fuselage and the inlet. Interesting future work may involve a baseline CFD analysis of fuselage/inlet aerodynamics given the current elliptical shape. A body-fitted inlet (modeled after the F-16) may be necessary to improve compatibility.

A full UAV CFD model would be an excellent extension of this thesis to better understand the interaction between the external flow field from the fuselage forebody and the internal inlet flow field over a range of extreme flight conditions. Fuselage boundary layer ingestion would represent the main parameter of concern for full UAV CFD simulations. Results of the simulations may motivate changes in the inlet length and offset dimensions.

Future controlled experimental testing is suggested to calibrate computational models. Static tests of a JetCat P-20SX engine can be used to formulate a baseline for engine performance. The XQ-1A inlet should be fabricated, installed on the engine, and tested under identical freestream conditions as the static tests to isolate inlet effects and evaluate inlet/engine compatibility. The inlet/engine configuration should then be installed within the 1/3rd-scale demonstrator model to understand the performance of the fully integrated system. In all cases, a total pressure rake similar to the one described in this thesis should be installed at an identical AIP location to evaluate the changes in total pressure recovery and circumferential/radial total pressure distortion. The AIP location may not be ideal using JetCat P-20SX engine due to the flow interference caused by the

electric starter motor. In the absence of the JetCat P-20SX engine, engine flight simulators may serve as an effective replacement to evaluate inlet performance.

Flight-test performance represents the ultimate performance evaluator of the inlet. The platform must be further developed to evaluate inlet/engine compatibility based on flight-test performance over the full range of flight conditions. A full combination of computational models, experimental tests, and flight-tests performed under similar flight conditions represents a complete subsonic analysis of the UAV design. Finally, the subsonic platform can be used as a foundation to further develop the UAV design for high-speed flight.

BIBLIOGRAPHY

- [1] The Fédération Aéronautique Internationale, 2019, “Section 12 – Unmanned Aerial Vehicles. UAV, Class U,”
https://www.fai.org/sites/default/files/documents/sc12_vol_u_uav_19.pdf.
- [2] McCrink, M.H., “Development of Flight-Test Performance Estimation Techniques for Small Unmanned Aerial Systems,” Dissertation, The Ohio State University, 2015.
- [3] McCrink, M., and Gregory, J.W., “Design and Development of a High-Speed UAS for Beyond Line-of-Sight Operation.” *AIAA 2018-0750, 2018 AIAA Information Systems-AIAA Infotech@ Aerospace*, 2018, pp. 0750. doi:10.2514/6.2018-0750.
- [4] Raymer, Daniel P. *Aircraft Design: A Conceptual Approach*. 5th ed., American Institute of Aeronautics and Astronautics, 2012.
- [5] Trussa, Colin W., “Low-Speed Aerodynamic Characteristics of a Delta Wing with Articulated Wing Tips,” MS Thesis, The Ohio State University, 2020.
- [6] Disotell, Kevin. "Low-Frequency Flow Oscillations on Stalled Wings Exhibiting Cellular Separation Topology." Electronic Thesis or Dissertation. Ohio State University, 2015. *OhioLINK Electronic Theses and Dissertations Center*. 22 Mar 2020.
- [7] Barlow, J. B., Rae Jr., W. H., Pope, A., 1999, *Low-Speed Wind Tunnel Testing*, 3rd Edition, John Wiley and Sons.
- [8] Schmidt, Louis V. *Introduction to Aircraft Flight Dynamics*. American Institute of Aeronautics and Astronautics, 1998.
- [9] Rusincovitch, J. G., “On the Development of a Six Component Platform for Testing Aircraft Models.” *Ohio State University*, 2004.
- [10] Whitfield, C. A., “Calibration Report.” Whitfield Aerospace, July 19, 2018.
- [11] Whitfield, C. A., “Drag Build-up and Oswald Efficiency Factor Estimation” slides sent via e-mail, March 2020.
- [12] JetCat website,
https://www.jetcat.de/en/productdetails/produkte/jetcat/produkte/hobby/Engines/p20_sx, Date accessed: 3/24/2020.

- [13] Seddon, J., and Goldsmith, E. L., *Intake Aerodynamics*, AIAA Education Series, AIAA, New York, 1985.
- [14] Wikimedia Commons,
https://upload.wikimedia.org/wikipedia/commons/1/14/USAF_F-16C_Block_40H_%2890-0710%29_air_intake_%26_nose_landing_gear_at_MCAS_Iwakuni_May_5%2C_2016.jpg,
Date accessed: 3/27/2020.
- [15] *United States Air Force Research Accomplishments*, Office of Aerospace Research, United States Air Force, June 1964.
- [16] Hamstra el al., 1998, *Transition Shoulder System and Method for Diverting Boundary Layer Air*, US005749542A, United States Patent No. 5,749,542.
- [17] Wikimedia Commons,
[https://commons.wikimedia.org/wiki/File:Navy_pilot_taxis_in_an_F-35C_Lightning_II_carrier_variant,_on_the_flight_deck_of_the_USS_George_Washington_\(29022078605\).jpg](https://commons.wikimedia.org/wiki/File:Navy_pilot_taxis_in_an_F-35C_Lightning_II_carrier_variant,_on_the_flight_deck_of_the_USS_George_Washington_(29022078605).jpg),
Date accessed: 3/27/2020.
- [18] Gad-el-Hak, M., and Ron F. B., “The Discrete Vortices from a Delta Wing.” *AIAA Journal*, Vol. 23, No. 6, 1985, pp. 961–962. doi: 10.2514/3.9016.
- [19] Lockheed Martin website,
<https://www.lockheedmartin.com/en-us/products/f-16.html>,
Date accessed: 3/24/2020.
- [20] Ibrahim, I.H., 2008, “Fluid Flow Studies of the F-5E and F-16 Inlet Ducts,” Master of Engineering Thesis, Nanyang Technological University, School of Mechanical and Aerospace Engineering.
- [21] Melampy, J., 2007, “The Modern Viper Guide – The F-16 C/D Exposed,” Reid Air Publications.
- [22] C.G. Caro, T.J. Pedley, R.C. Schroter, and W.A. Seed, 2012, *The Mechanics of the Circulation*, 2nd ed., Cambridge University Press, New York.
- [23] W.R. Dean M.A. (1927) XVI. *Note on the motion of fluid in a curved pipe* , The London, Edinburgh, and Dublin Philosophical Magazine and Journal of Science, 4:20, 208-223,
DOI: 10.1080/14786440708564324.

- [24] M.J. Tunstall, and Harvey, J.K., 1968, "On the effect of a sharp bend in a fully developed turbulent pipe-flow," *J. Fluid Mech.*, vol. 34, part 3, pp. 595-608.
- [25] Ligrani, P.M., 1994, "A Study of Dean Vortex Development and Structure in a Curved Rectangular Channel with Aspect Ratio of 40 at Dean Numbers up to 430," NASA Contractor Report 4607, Army Research Laboratory Contractor Report ARL-CR-144.
- [26] S.A. Berger, L. Talbot, L.-S. Yao, 1983, "Flow in Curved Pipes," *Ann. Rev. Fluid Mech.*, 15, pp. 461-512.
- [27] SAE Aerospace Recommended Practice, "Gas Turbine Engine Inlet Flow Distortion Guidelines," SAE ARP1420, Rev. B, 2011.
- [28] Çengel, Y.A., Cimbala, J.M., 2013, *Fluid Mechanics Fundamentals and Applications*, 3rd Edition, McGraw-Hill.
- [29] Towne, C.E. and Schum, E.F., 1985, "Application of computational fluid dynamics to complex inlet ducts," AIAA Conference Paper, 95-0035.
- [30] Fotios Papadopoulos, Ioannis Valakos, Ioannis K. Nikolos, 2012, "Design of an S-duct intake for UAV applications", *Aircraft Engineering and Aerospace Technology*, Vol. 84 Iss: 6 pp. 439 – 456.
- [31] Gopaliya, M. K., Kumar, M., Kumar, S., Gopaliya, S. M.. "Analysis of performance characteristics of S-shaped diffuser with offset." *Aerospace Science and Technology*, Vol. 11, No. 2-3, 2007, pp. 130–135., doi:10.1016/j.ast.2006.11.003.
- [32] Gupta, V., Devpura, R., Singh, S. N., and Seshadri, V., "Effect of aspect ratio and curvature on characteristics of S-shaped diffusers." *Indian Journal of Engineering & Material Sciences*, Vol. 8, June 2001, pp. 141–148.
- [33] Lee, J., and Cho, J., "Effect of aspect ratio of elliptical inlet shape on performance of subsonic diffusing S-duct," *Journal of Mechanical Science and Technology*, Vol. 32, No. 3, 2018, pp. 1153–1160. doi:10.1007/s12206-018-0218-5.
- [34] Menzies R. D. D., "Investigation of S-Shaped Intake Aerodynamics Using Computational Fluid Dynamics," Ph.D. Dissertation, Department of Aerospace Engineering, University of Glasgow, Glasgow, 2002.
- [35] Berrier, B.L., and Allan, B.G., 2004, "Experimental and Computational Evaluation of Flush-Mounted, S-Duct Inlets," NASA Langley Research Center, AIAA 2004-0764.

- [36] Gil-Prieto, D., MacManus, D.G., Zachos, P.K., Tanguy, G., Wilson, F., and Chiereghin, N., “Delayed Detached-Eddy Simulation and Particle Image Velocimetry Investigation of S-Duct Flow Distortion,” AIAA Journal, Vol. 55, No. 6, June 2017. doi: 10.2514/1.J055468.
- [37] Simcenter STAR-CCM+ Theory Guide (v.14.02.010). Siemens PLM Software.
- [38] Berens, T.M., Delot, A., Chevalier, M., et. al., “Application of CFD to High Offset Intake Diffusers,” GARTEUR AD/AG-43, GARTEUR TP-173, October 2012.

APPENDIX

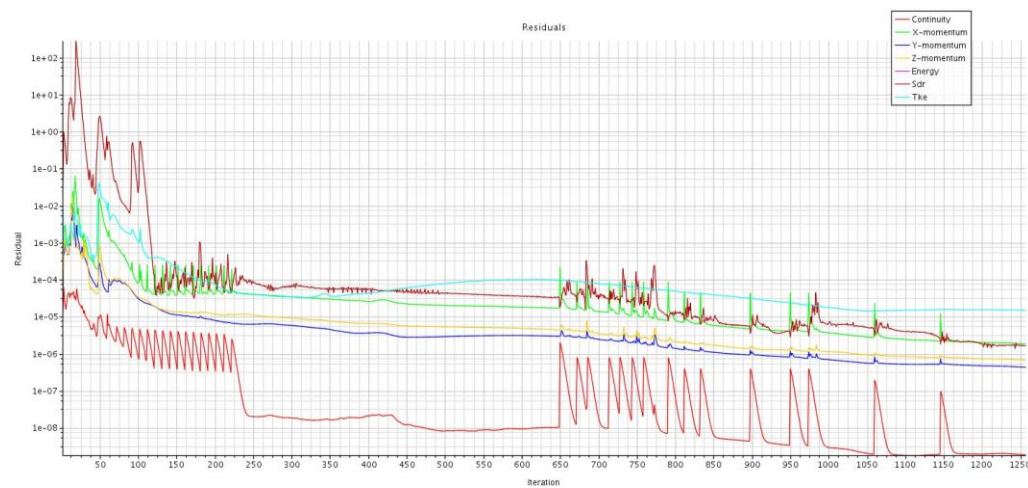


Figure 68 RAE-M2129 mesh validation residuals

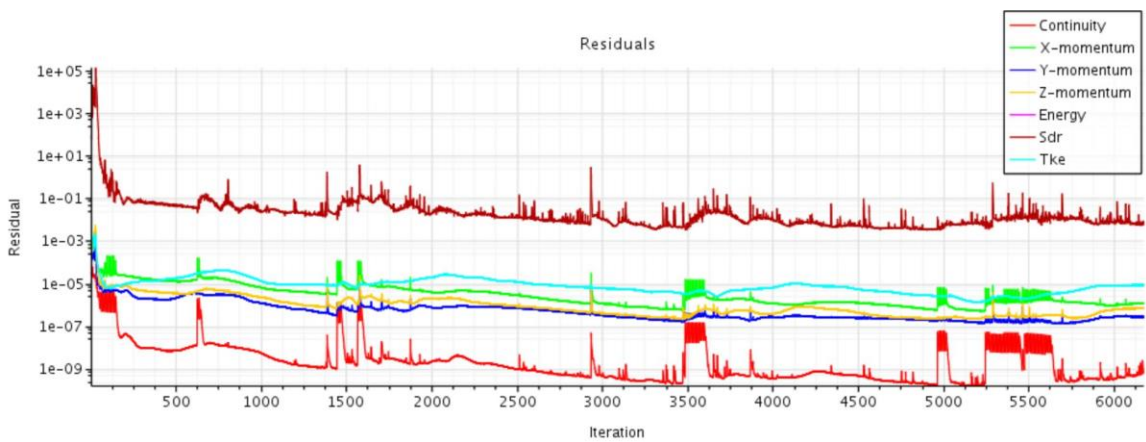


Figure 69 XQ-1A 0° AOA residuals

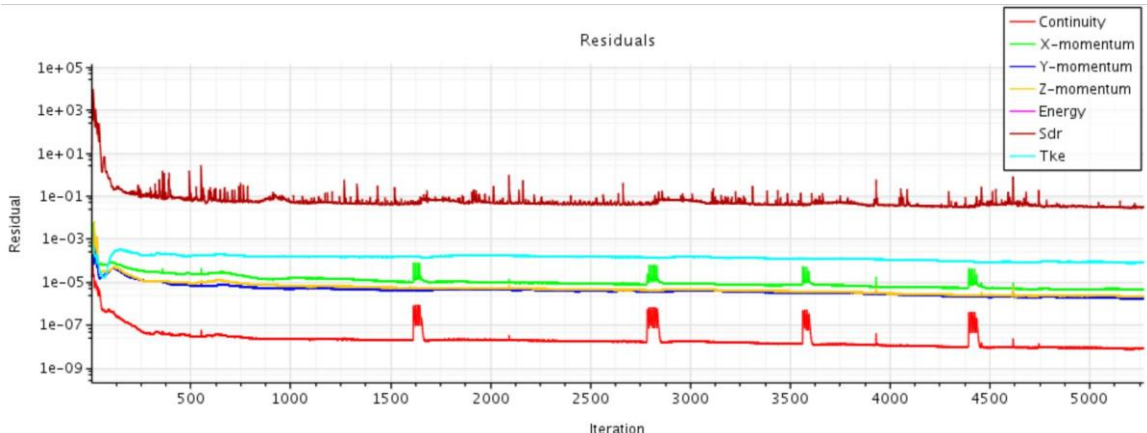


Figure 70 XQ-1A 21° AOA residuals

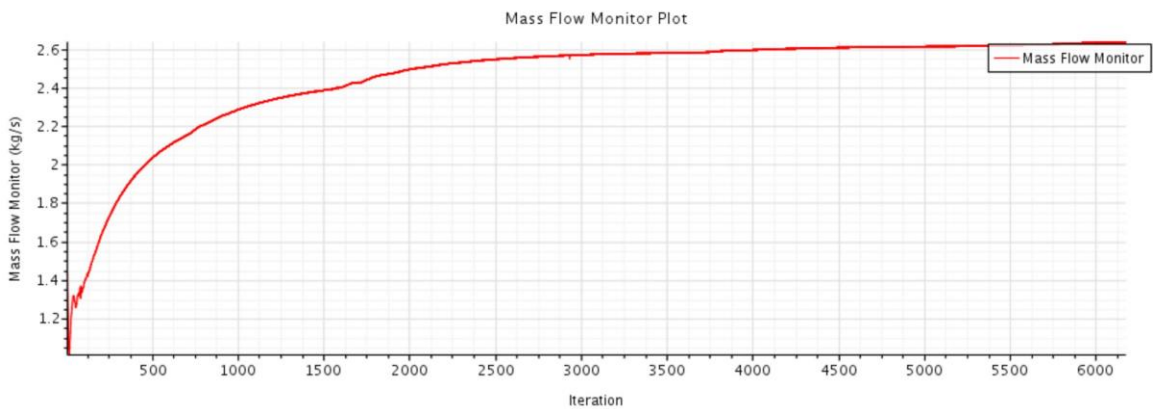


Figure 71 XQ-1A 0° AOA mass flow solution monitor

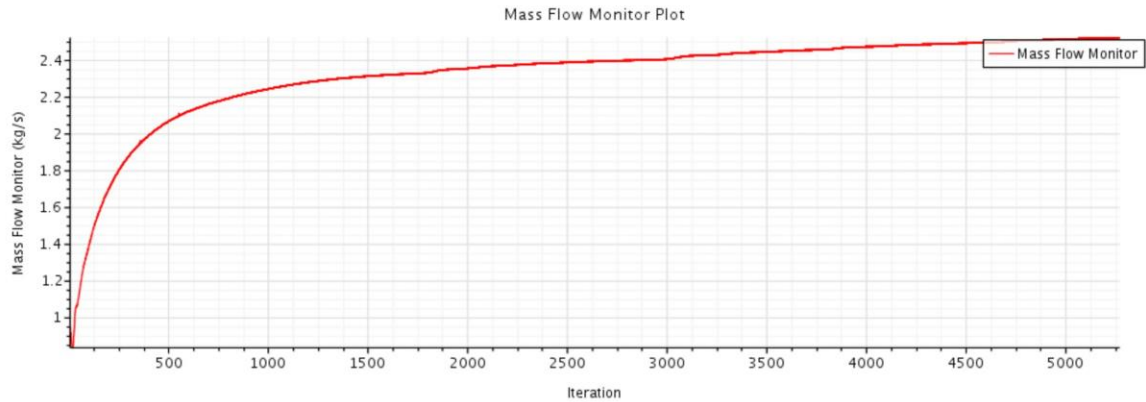


Figure 72 XQ-1A 21° AOA mass flow solution monitor

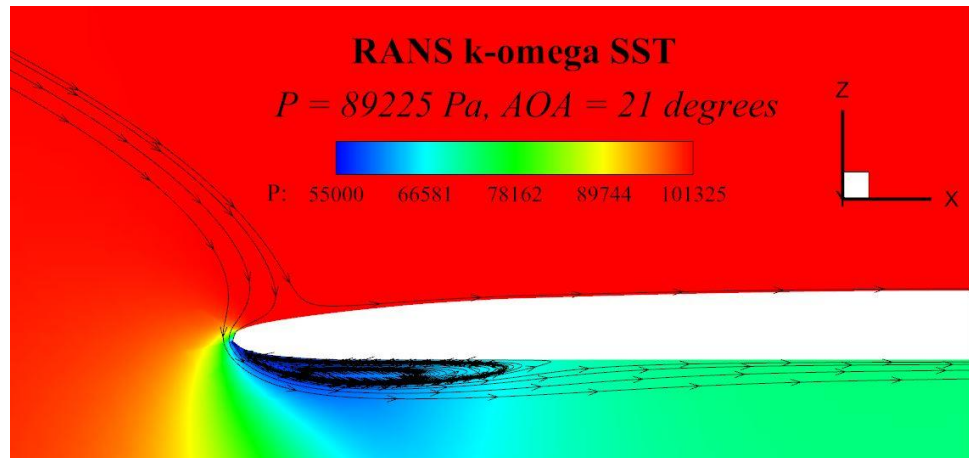


Figure 73 Inlet lip flow separation observed for XQ-1A at 21° AOA